Study of transition metals doped strontium zirconate/manganite for solid oxide fuel cell applications

A

Thesis

Submitted in the partial fulfilment of the requirements for the award of the degree of

DOCTOR OF PHILOSOPHY

By

Paramvir Kaur
Regn. No. 901612009

Under the supervision of

Dr Kulvir Singh
Professor and Head



School of Physics and Materials Science
Thapar Institute of Engineering and Technology
(Deemed-to-be-University)
Patiala-147004, Punjab, India

October-2021

CERTIFICATE

I hereby declare that the work which has been presented in the thesis entitled ***"Study of transition metals doped strontium zirconate/manganite for solid oxide fuel cell applications"*** is an authentic record of my work carried out for the partial fulfilment of the requirements for the award of the degree of Doctor of Philosophy in the School of Physics and Materials Science, Thapar Institute of Engineering and Technology, Patiala (Deemed-to-be-University) under the supervision of ***Dr Kulvir Singh***. The matter submitted in the thesis has not been submitted in part or full to any other university or institute for the award of any degree.

Date: 12-10-2021
Place: Patiala

Paramvir Kaur
Paramvir Kaur
(901612009)

It is certified that the above statement made by the candidate is correct and true to the best of my knowledge and belief.

Dr Kulvir Singh
Professor and Head

School of Physics and Materials Science
Thapar Institute of Engineering and Technology
(Deemed-to-be-University)
Patiala-147004, Punjab, India

Dedicated to

my

beloved grandparents

Acknowledgement

To begin with, I would like to express my gratitude and bow my head to the almighty for instilling in me the strength and willpower to keep pushing myself forward no matter how hard the circumstances. After God is the mentor. I am highly thankful to my supervisor ***Dr Kulvir Singh*** for introducing me to the world of materials science and the scientific community. I am grateful for his motivation, support, and encouragement throughout my PhD. I am highly indebted to ***Dr O.P. Pandey***, Senior Professor, School of Physics and Materials Science, Thapar Institute of Engineering and Technology, Patiala, Punjab, for his encouragement. Dr Pandey's zest for life is an inspiration. I am thankful to my doctoral committee members, ***Dr D.P. Singh***, ***Dr B.C. Mohanty*** and ***Dr Prasenjit Basak*** for their suggestions and comments during the progress report presentations. I am highly grateful to my parents ***Mrs Gurinder Kaur*** and ***S. Pritpal Singh,*** for their constant encouragement and motivation. The journey through my PhD would never have been accomplished without their firm belief and invaluable, everlasting support.

I am thankful to Thapar Institute of Engineering and Technology, Patiala, Punjab, for providing funding as a ***Teaching Associate*** and the Department of Science and Technology (DST), Ministry of Science and Technology, Government of India for the financial assistance through ***Project Associate-I*** under Hydrogen and Fuel Cell (HFC)-2018 project ***DST/TMD/HFC/2k18/123***.

I would like to acknowledge ***SAI Labs, Thapar Institute of Engineering and Technology, Patiala, Punjab***, ***SAIF/CIL Panjab University, Chandigarh,*** and ***IIC IIT-Roorkee*** for providing characterization facilities. I am deeply thankful to ***Dr B.N. Chudasama***, ***Dr Loveleen K. Brar,*** and ***Dr Jayant Kolte*** for their valuable suggestions during various stages of my research work. Special thanks to ***Dr Devender Kumar***, Assistant Professor, Mechanical Engineering Department, Thapar Institute of Engineering and Technology,

Patiala, Punjab, for his encouragement, support, and help even at the eleventh hour. Sincere thanks to ***Ms Neelam Sadana***, ***Mr Lalji Verma***, ***Ms Amandeep Kaur***, ***S. Jant Singh***, ***Mr Purushottam Kumar Singh,*** and ***Mr Vijay K. Verma*** for their help in official and technical matters.

Special thanks to ***Ms Anandita Arora***, ***Mr Jatinder Singh***, ***Mr Piyush Sharma***, ***Dr Rameez Ahmad Mir***, ***Dr Santosh Kumar Mahadevan***, ***Dr Chhavi Pahwa***, ***Mr Anoop Pratap Singh*** for their help and support during my initial years. I would like to acknowledge the help and support received from ***Ms Supreet Kaur, Ms Navneet Kaur, Ms Sandeep Dhillon***, ***Ms Simran Mehta,*** and ***Mr Vikramjit Singh***. Sincere thanks to ***Dr Samita*** for taking out time from her schedule for technical discussions. I am thankful to senior lab members ***Dr Satwinder Singh Danewalia***, ***Dr Pooja Singla***, ***Dr Gaurav Sharma***, ***Dr Neetu Bansal,*** and ***Mr Savidh Khan*** for their help. I sincerely appreciate my lab mates' ***Ms Shivani Punj***, ***Ms Manmeet Kaur***, ***Ms Trisha Walia***, ***Ms Taranvir Kaur***, ***Ms Vimi Dua***, ***Ms Navneet Kaur,*** and ***Mr Santosh Kumar*** constant support, encouragement, and care.

Heartfelt thanks and respect to each staff member of Hostels E, I, and PG, respectively, for their care, help, and much-needed support through the weakest of moments. Words fall short of expressing my gratitude to my friends ***Ms Nitika Sihota, Ms Ekta Jaglan, Ms Aruna Sharma, Ms Deepa Negi,*** and ***Ms Kanwarpreet Kaur*** for being there through thick and thin. Without you all, I wouldn't have had the courage to get over and start fresh each time I fell. In the end, I sincerely thank every person who has come across this journey for their encouragement and support.

Paramvir Kaur

Paramvir Kaur

Index

Contents	Page No.
Certificate	*i*
Acknowledgement	*iii*
List of figures	*viii*
List of tables	*xiii*
List of publications	*xv*
List of conferences attended	*xvi*
List of abbreviations	*xvii*
Abstract	*xix*
Chapter 1: Introduction	1-20
1.1. Fuel cells	1
1.2. Solid oxide fuel cells	4
1.3. Design and components of a SOFC	6
1.3.1. Anode	7
1.3.2. Electrolyte	8
1.3.3. Interconnect	8
1.3.4. Sealant	8
1.3.5. Cathode	9
1.4. Reaction mechanism at the cathode	11
1.5. Role of transition metals doping in perovskite-structured materials	12
References	17
Chapter 2: Literature review	21-39
2.1. Introduction	21
2.2. $SrZrO_3$ materials	23
2.3. $SrMnO_3$ materials	27
2.4. Interaction study of SOFC components	30
2.5. The motivation of the present study	33
2.6. Objectives	34
References	35
Chapter 3: Experimental procedure	40-65
3.1. Raw materials	40
3.2. Sample synthesis procedure	40
3.3. Characterisation techniques	43
3.3.1. X-ray diffraction (XRD)	43
3.3.2. Rietveld refinement	45
3.3.3. Fourier-transform infrared spectroscopy (FTIR)	47
3.3.4. Density and other physical parameters	48

3.3.5. Scanning electron microscopy (SEM) and energy dispersive spectroscopy (EDS) 49
3.3.6. X-ray photoelectron spectroscopy (XPS) 51
3.3.7. Dilatometry 53
3.3.8. Thermogravimetric and differential thermal analysis (TG-DTA) 54
3.3.9. Impedance spectroscopy 55
3.3.10. Ultraviolet-visible (UV) spectroscopy 58
3.3.11. Photoluminescence (PL) spectroscopy 60
3.3.12. Vickers hardness 61
References 64

Chapter 4: Results and discussion-I *66-102*

4.1. Undoped and Cu-doped $SrZr_{1-x}Cu_xO_{3-\delta}$ ($0.00 \leq x \leq 0.20$) 66
4.1.1. XRD analysis 66
4.1.2. FTIR analysis 71
4.1.3. Physical parameters 73
4.1.4. Microstructural analysis 74
4.1.5. TG-DTA analysis 77
4.1.6. Thermal expansion analysis 78
4.1.7. Conductivity analysis 80

4.2. Undoped and Ni-doped $SrZr_{1-x}Ni_xO_{3-\delta}$ ($0.00 \leq x \leq 0.20$) 84
4.2.1. XRD analysis 84
4.2.2. FTIR analysis 86
4.2.3. Microstructural analysis 88
4.2.4. TG-DTA analysis 90
4.2.5. Thermal expansion analysis 92
4.2.6. Band gap analysis 93
4.2.7. Photoluminescence analysis 95
References 99

Chapter 5: Results and discussion-II *103-134*

5.1. Undoped and Cu-doped $SrMn_{1-x}Cu_xO_{3-\delta}$ ($0.00 \leq x \leq 0.20$) 103
5.1.1. XRD analysis 103
5.1.2. FTIR analysis 108
5.1.3. Physical parameters 109
5.1.4. Microstructural analysis 110
5.1.5. TG-DTA analysis 113
5.1.6. Thermal expansion analysis 114
5.1.7. Conductivity analysis 115

5.2. Undoped and Ni-doped $SrMn_{1-x}Ni_xO_{3-\delta}$ ($0.00 \leq x \leq 0.20$) 119
5.2.1. XRD analysis 119
5.2.2. FTIR analysis 122
5.2.3. Physical parameters 123
5.2.4. Microstructural analysis 124

5.2.5. TG-DTA analysis 126
5.2.6. Thermal expansion analysis 127
5.2.7. Conductivity analysis 128
References 132

Chapter 6: Results and discussion-III *135-146*

6.1. An interaction study with sealant and interconnect 135
6.1.1. XRD analysis 135
6.1.2. Microstructural analysis 139
6.1.3. Thermal expansion analysis 143

6.2. An interaction study with interconnect 144
References 146

Chapter 7: Conclusion and future scope *147-148*

7.1. Conclusion 147
7.2. Future scope 148

Appendix *149*

List of figures

Figure no.	Description	Page no.
Fig. 1.1	An illustration of the fuel cell devised by Sir William Grove in 1839 [9]	2
Fig. 1.2	Demonstration of a ~50 kW proof-of-concept SOFC power system by Fuel Cell Energy [13]	3
Fig. 1.3	Classification of different fuel cells based on the type of electrolyte and their operating temperature	3
Fig. 1.4	Schematic representation of a SOFC with a detailed description of the different components [20]	5
Fig. 1.5	Schematic of (a) planar and (b) tubular design SOFC [21]	7
Fig. 1.6	Schematic representation of the planar design SOFC components [30]	9
Fig. 1.7	Diagrammatic illustration of the TPB in the vicinity of which the oxygen reduction reaction (ORR) takes place [20]	10
Fig. 1.8	Essential cathode material properties for SOFC [20]	11
Fig. 1.9	Diagrammatic representation of the ORR in a pure electronic cathode, a composite cathode, and a mixed conducting cathode, respectively [42]	12
Fig. 1.10	A diagrammatic representation of a basic perovskite oxide [46]	13
Fig. 3.1	Schematic of the synthesis procedure of $SrM_{1-x}A_xO_{3-\delta}$ (M=Zr, Mn; A=Cu, Ni; $0.00 \leq x \leq 0.20$)	40
Fig. 3.2	Diffusion couple of SZC-15 and SBBZ. The upper white coloured layer represents the glass SBBZ, and the lower black layer corresponds to SZC-15	43
Fig. 3.3	An illustration of the (a) different components that make up an X-ray diffractometer and (b) the basic principle of X-ray diffraction	44
Fig. 3.4	Representative Rietveld plot of SZC-10. The red dotted line represents the observed data, and the black line represents the calculated data. A complete overlap of the two results in a straight blue line exhibiting complete refinement	46
Fig. 3.5	An illustration of the principle of FTIR	47
Fig. 3.6	Schematic of (a) SEM and (b) typical emissions emitted out from the sample when an incident beam interacts with a specimen [9]	50
Fig. 3.7	(a) Sintered pellets placed on a stub for coating, (b) auto fine coater by JEOL, under which the samples are placed for	51

	coating, and (c) the diffusion couple placed in a mould	
Fig. 3.8	An illustration of the (a) basic principle and (b) instrumentation of XPS	53
Fig. 3.9	Pictorial representation of a push rod type dilatometer	54
Fig. 3.10	Diagrammatic representation of the instrumentation of (a) TGA and (b) DTA/DSC setup	55
Fig. 3.11	An illustration of the relationship between the electrical properties with grain, grain boundary and interface [14]	56
Fig. 3.12	(a) Solartron SI 1260 frequency response analyser, (b) temperature monitor showing the real and programmed temperature, (c) ProboStat containing the sample holder and (d) enlarged view of the sample holder	57
Fig. 3.13	Representative Arrhenius plot of SZC-20. The slopes of the two curves give the E_a of the low and high-temperature regions	58
Fig. 3.14	Diagrammatic representation of a UV-Vis spectrometer setup	60
Fig. 3.15	Diagrammatic representation of the PL setup [20]	61
Fig. 3.16	Pictorial representation of a Mitutoyo MVK-H0 Vickers micro indentation tester	62
Fig. 4.1	(a) XRD patterns of $SrZr_{1-x}Cu_xO_{3-\delta}$ ($0.00 \leq x \leq 0.20$) and (b) refined XRD pattern of SZC-10 confirming orthorhombic structure with *Pbnm* space group	67
Fig. 4.2	Shifting of the highest intense XRD peak (112) with the incorporation of copper in the $SrZrO_3$ system	69
Fig. 4.3	XPS spectra of Cu in (a) SZC-5, (b) SZC-10 and (c) SZC-20	70
Fig. 4.4	FTIR spectra of (a) undoped and (b) Cu-doped $SrZrO_3$	72
Fig. 4.5	SEM micrographs of (a) SZ-0, (b) SZC-5, (c) SZC-10, (d) SZC-15 and (e) SZC-20	75
Fig. 4.6	Variation of density and grain size with an increasing Cu-dopant concentration in $SrZr_{1-x}Cu_xO_{3-\delta}$	76
Fig. 4.7	Representative (a) TG plots (b) DTA curves of SZ-0, SZC-10 and SZC-20	78
Fig. 4.8	Thermal expansion curves of $SrZr_{1-x}Cu_xO_{3-\delta}$ ($0.00 \leq x \leq 0.20$) measured in the temperature range of 200-1000°C	79
Fig. 4.9	Representative Nyquist plot of SZC-10 along with equivalent circuit measured at 350°C	80
Fig. 4.10	Representative Arrhenius plots of (a) SZ-0, (b) SZC-10 and (c) SZC-20	83
Fig. 4.11	(a) XRD patterns of $SrZr_{1-x}Ni_xO_{3-\delta}$ ($0.00 \leq x \leq 0.20$) showing the formation of a single-phase and (b) representative refined pattern of SZN-5	85

Fig. 4.12	Slight shifting of the XRD peaks corresponding to the (002) peak towards higher angles confirming compressive strain in the lattice	86
Fig. 4.13	FTIR spectra of (a) undoped and (b) doped $SrZr_{1-x}Ni_xO_{3-\delta}$ ($0.05 \leq x \leq 0.20$)	88
Fig. 4.14	SEM micrographs of fractured surfaces of (a) SZ-0, (b) SZN-5, (c) SZN-10, (d) SZN-15 and (e) SZN-20	89
Fig. 4.15	(a) TG plots, (b) DTA and DSC curves of $SrZr_{1-x}Ni_xO_{3-\delta}$ ($0.05 \leq x \leq 0.20$)	91
Fig. 4.16	Dilatometry curves of $SrZr_{1-x}Ni_xO_{3-\delta}$ (x=0.00, 0.10, 0.15,0.20)	92
Fig. 4.17	Tauc plot of $SrZr_{1-x}Ni_xO_{3-\delta}$ ($0.05 \leq x \leq 0.20$) with diffuse reflectance spectra in the inset	93
Fig. 4.18	Variation of E_g and E_u with increasing Ni-dopant concentration in $SrZr_{1-x}Ni_xO_{3-\delta}$	95
Fig. 4.19	PL (a) emission and (b) excitation spectra of $SrZr_{1-x}Ni_xO_{3-\delta}$ ($0.00 \leq x \leq 0.20$)	96
Fig. 5.1	XRD patterns of (a) $SrMn_{1-x}Cu_xO_{3-\delta}$ ($0.00 \leq x \leq 0.20$) and (b) $SrMnO_3$ with respect to different temperatures and time durations	104
Fig. 5.2	XPS spectra of (a) Mn^{4+} in SM-0, (b) Mn^{4+} in SMC-10 and (c) Cu^{2+} in SMC-10	105
Fig. 5.3	Variation in the volume fraction of the different crystalline phases with an increasing dopant concentration of Cu in $SrMnO_3$	106
Fig. 5.4	Slight shifting of the highest intense peak of $SrMn_{1-x}Cu_xO_{3-\delta}$ ($0.00 \leq x \leq 0.20$) towards lower diffraction angles signifies the effective doping of higher ionic radii dopant in place of a lower ionic radii host	107
Fig. 5.5	FTIR spectra of (a) $SrMnO_3$ and (b) $SrMn_{1-x}Cu_xO_{3-\delta}$ ($0.05 \leq x \leq 0.20$)	109
Fig. 5.6	SEM micrographs of (a) SM-0, (b) SMC-5, (c) SMC-10, (d) SMC-15 and (e) SMC-20	111
Fig. 5.7	Variation in the density and average grain size of Cu-doped $SrMnO_3$ with increasing dopant concentration	112
Fig. 5.8	Representative (a) TG plots and (b) DTA curves of $SrMn_{1-x}Cu_xO_{3-\delta}$ (x=0.00, 0.10, 0.20)	114
Fig. 5.9	Thermal expansion curves of $SrMn_{1-x}Cu_xO_{3-\delta}$ ($0.00 \leq x \leq 0.20$)	114
Fig. 5.10	(a) Room-temperature Nyquist plots of $SrMn_{1-x}Cu_xO_{3-\delta}$ ($0.00 \leq x \leq 0.20$) with the inset showing the magnified exhibiting the distortion of the semi-circle and (b) fitted SMC-20 with the equivalent circuit	116

Fig. 5.11	Representative Arrhenius plots of (a) SM-0, (b) SMC-10 and (c) SMC-20	118
Fig. 5.12	XRD patterns of $SrMn_{1-x}Ni_xO_{3-\delta}$ ($0.00 \leq x \leq 0.20$) showing the presence of secondary phases	119
Fig. 5.13	XPS spectra of (a) Mn^{4+} in SM-0, (b) Mn^{4+} in SMN-10 and (c) Ni^{2+} in SMN-10	120
Fig. 5.14	Variation in the volume fraction of the different crystalline phases with an increasing dopant concentration of Ni in $SrMnO_3$	121
Fig. 5.15	Shifting of the highest intense peak of $SrMn_{1-x}Ni_xO_{3-\delta}$ ($0.00 \leq x \leq 0.20$)	121
Fig. 5.16	FTIR spectra of (a) $SrMnO_3$ and (b) $SrMn_{1-x}Ni_xO_{3-\delta}$ ($0.05 \leq x \leq 0.20$)	123
Fig. 5.17	SEM micrographs of (a) SM-0, (b) SMN-5, (c) SMN-10, (d) SMN-15 and (e) SMN-20	125
Fig. 5.18	Variation in the density and average grain size of Ni-doped $SrMnO_3$ with increasing dopant concentration	126
Fig. 5.19	Representative (a) TG plots and (b) DTA curves of $SrMn_{1-x}Ni_xO_{3-\delta}$ (x=0.00, 0.10, 0.20)	127
Fig. 5.20	Thermal expansion curves of $SrMn_{1-x}Ni_xO_{3-\delta}$ ($0.00 \leq x \leq 0.20$)	128
Fig. 5.21	Room-temperature Nyquist plots of SMN-15 and SMN-20 exhibiting similar characteristics as that of Cu-doped $SrMnO_3$ and the inset showing the corresponding equivalent circuit for SMN-20	129
Fig. 5.22	Representative Arrhenius plots of SM-0, SMN-10 and SMN-20	130
Fig. 6.1	XRD patterns of (a) SBBZ, SZC-15, IS-1, IS-2, IS-3, and IS-4 representing the presence of $BaSrSi_2O_6$, quartz, and cristobalite phases and (b) magnified view of the secondary phases	136
Fig. 6.2	XRD peak shifting highest intense peak corresponding to (112) plane of IS-1, IS-2, IS-3, and IS-4 with respect to SZC-15	137
Fig. 6.3	SEM micrographs of (a) SZC-15, (b) IS-1, (c) IS-2 and (d) IS-3 showing variation in the microstructure	139
Fig. 6.4	FE-SEM micrographs showing a clear distinction between the cathode (left) and the glass sealant (right) with increasing magnification without the formation of any intermediate undesired phases at the interface	141
Fig. 6.5	Line and dot mapping of IS-4 showing the diffusion of different elements from cathode and glass side over the interface	142

Fig. 6.6	(a) The thermal expansion curves of IS-1, IS-2, IS-3, and IS-4, respectively, and (b) variation in the CTE of the samples with increasing heat durations	143
Fig. 6.7	XRD patterns of ISC-1 and ISC-2 showing no presence of Crofer elements	144
Fig. 6.8	Representative picture of the heat-treated diffusion couple of the cathode-glass sealant. The rectangular bars are the Crofer 22 APU and the brown powdered layer sandwiched between the layers is SZC-15	145

List of tables

Table no.	Description	Page no.
Table 1.1	Goldschmidt's tolerance factor and corresponding associated symmetry along with is the cation size	14
Table 2.1	The coefficient of thermal expansion (CTE), electronic (σ_e) and ionic conductivities (σ_i) of probable SOFC cathode materials	30
Table 3.1	The calcination and sintering temperatures and the respective time durations of the compositions used in this study. Here x=0.05, 0.10, 0.15, 0.20 for all the compositions	41
Table 3.2	Standard capacitance values of different microstructural parts of the sample and electrode	57
Table 4.1	Lattice parameters of $SrZr_{1-x}Cu_xO_{3-\delta}$ ($0.00 \leq x \leq 0.20$) calculated from Rietveld refinement	68
Table 4.2	FWHM and mean crystallite size of $SrZr_{1-x}Cu_xO_{3-\delta}$ ($0.00 \leq x \leq 0.20$) calculated for (112) peak	70
Table 4.3	Relative density, hardness, molar volume, concentration, polaron radius and the distance between Cu^{2+} ions of $SrZr_{1-x}Cu_xO_{3-\delta}$ ($0.00 \leq x \leq 0.20$)	74
Table 4.4	Average grain size and EDS data of $SrZr_{1-x}Cu_xO_{3-\delta}$ ($0.00 \leq x \leq 0.20$)	77
Table 4.5	Total conductivity (σ) of $SrZr_{1-x}Cu_xO_{3-\delta}$ ($0.00 \leq x \leq 0.20$)	81
Table 4.6	Activation energies (E_a) of $SrZr_{1-x}Cu_xO_{3-\delta}$ ($0.00 \leq x \leq 0.20$)	83
Table 4.7	FWHM and mean crystallite size of $SrZr_{1-x}Ni_xO_{3-\delta}$ ($0.00 \leq x \leq 0.20$)	85
Table 4.8	Elemental composition (wt.%) of $SrZr_{1-x}Ni_xO_{3-\delta}$ ($0.00 \leq x \leq 0.20$) obtained from EDS analysis	90
Table 5.1	FWHM and mean crystallite size of $SrMn_{1-x}Cu_xO_{3-\delta}$ ($0.00 \leq x \leq 0.20$)	107
Table 5.2	Density, hardness, molar volume, concentration, polaron radius and the distance between Cu^{2+} ions of $SrMn_{1-x}Cu_xO_{3-\delta}$ ($0.00 \leq x \leq 0.20$)	110
Table 5.3	Weight % of the different elements of the composition	113

	$SrMn_{1-x}Cu_xO_{3-\delta}$ ($0.00 \leq x \leq 0.20$)	
Table 5.4	Total conductivity (σ) of $SrMn_{1-x}Cu_xO_{3-\delta}$ ($0.00 \leq x \leq 0.20$)	117
Table 5.5	Activation energy (E_a) of $SrMn_{1-x}Cu_xO_{3-\delta}$ ($0.00 \leq x \leq 0.20$)	118
Table 5.6	FWHM and mean crystallite size of $SrMn_{1-x}Ni_xO_{3-\delta}$ ($0.00 \leq x \leq 0.20$)	122
Table 5.7	Density, hardness, molar volume, concentration, polaron radius and the distance between Ni^{2+} ions of $SrMn_{1-x}Ni_xO_{3-\delta}$ ($0.00 \leq x \leq 0.20$)	124
Table 5.8	Weight % of the different elements of the composition $SrMn_{1-x}Ni_xO_{3-\delta}$ ($0.00 \leq x \leq 0.20$)	126
Table 5.9	Total conductivity (σ) of $SrMn_{1-x}Ni_xO_{3-\delta}$ ($0.00 \leq x \leq 0.20$)	129
Table 5.10	Activation energy (E_a) of $SrMn_{1-x}Ni_xO_{3-\delta}$ ($0.00 \leq x \leq 0.20$)	131
Table 6.1	Volume fraction (%) of the different crystalline phases	137
Table 6.2	FWHM, crystallite size and density of SZC-15, IS-1, IS-2, IS-3 and IS-4	138
Table 6.3	Weight % of different constituents of the samples obtained from EDS analysis	141

List of publications

SCI

1. **Paramvir Kaur**, K. Singh, Effect of Ni substitution on the structural and optical properties of $SrZr_{1-x}Ni_xO_3$ ($0.05 \leq x \leq 0.20$) perovskites, ***J. Mol. Struct.*** 1180 (2019) 659-664 (**3.196**)

2. **Paramvir Kaur**, K. Singh, Review of perovskite-structure related cathode materials for solid oxide fuel cells, ***Ceram. Int.*** 46 (2020) 5521-5535 (**4.527**)

3. **Paramvir Kaur**, K. Singh, Structural, thermal and electrical study of copper doped strontium zirconate, ***Ionics*** 26 (2020) 6233-6244 (**2.817**)

4. **Paramvir Kaur**, V. Singh, K. Singh, Optical and photoluminescence properties of CaV_2O_6 functionalized by sodium doping, ***Mater. Today Commun.*** 27 (2021) 102354 ***(Not a part of the thesis)*** (**3.383**)

5. **Paramvir Kaur,** T. Walia, K. Singh, An interfacial study between $SrZr_{0.85}Cu_{0.15}O_{3-\delta}$ and barium oxide-containing borosilicate glass sealant for solid oxide fuel cell application, ***Mater. Chem. Phys.*** **(Communicated)**

6. **Paramvir Kaur,** K. Singh, Copper and nickel substituted strontium manganite ceramics and their structural, morphological and conducting properties, ***J. Am. Ceram. Soc.*** **(Communicated)**

Non-SCI

1. **Paramvir Kaur**, K. Singh, Structural and thermal properties of Ni-doped $SrZrO_3$ for solid oxide fuel cells, ***ECS Trans.*** 91(1) (2019) 1543-1550

2. **Paramvir Kaur**, K. Singh, Effect of sintering temperature on the crystal structure of $SrMnO_3$, ***AIP Conf. Proc.*** 2352 (2021) 020039

Book chapter

1. **Paramvir Kaur**, K. Singh, Perovskite-structured cobalt-free cathode materials for solid oxide fuel cells, in: M. Jeguirim (Ed.), Recent advances in Renewable Energy Technologies Vol 2, ***Acad. Press*** (2022) 357-373

List of conferences attended

Poster presentations

1. Effect of Ni doping on the structural and optical properties of $SrZr_{1-x}Ni_xO_{3-\delta}$ ($0.05 \leq x \leq 0.20$) perovskites, ***International Symposium on Functional Materials (ISFM-2018): Energy and Biomedical Applications*** held on April 13-15, 2018 at Shivalik View, Chandigarh

2. Structural and photoluminescence properties of $SrZr_{1-x}Cu_xO_{3-\delta}$ (x=0, 0.1, 0.2) perovskite oxide, ***Recent Advances in Condensed Matter Physics (RACMP)*** held on October 12-13, 2018 at Department of Physics, Kurukshetra University, Kurukshetra

3. Structural and thermal properties of Ni-doped $SrZrO_3$ for solid oxide fuel cells, ***16th International Symposium on Solid Oxide Fuel Cells (SOFC-XVI)*** held on September 8-13, 2019 at Kyoto Teresa, Kyoto, Japan

4. Effect of Cu doping in $SrZrO_3$ for solid oxide fuel cell applications, ***2nd Indian Materials Conclave and 31st AGM*** held on February 11-14, 2020 at CSIR-CGCRI, Kolkata, India

5. Transition metals doped strontium zirconate and strontium manganite perovskite for solid oxide fuel cell applications, ***DST Sponsored Industry-Academia Conclave on Hydrogen and Fuel Cells*** held on February 27-28, 2020 at IISER Thiruvananthapuram, Kerala, India

Oral presentations

1. Effect of sintering temperature on the crystal structure of $SrMnO_3$, ***5th National e-Conference on Advanced Materials and Radiation Physics (AMRP-2020)*** held on November 9-11, 2020 at SLIET, Longowal, Punjab, India

2. Copper and nickel doped strontium zirconate as cathode materials for solid oxide fuel cell, ***Energy Materials Conference 2021*** held on August 11-13, 2021 at Ulrika, Sweden

3. Transition metals doped strontium zirconate and manganite as cathode materials for solid oxide fuel cells, ***Ceramics Materials for Solid Oxide Fuel Cells (SOFCs)*** held on October 21, 2021 at ARCI Hyderabad, India

List of abbreviations

CHP	Combined heat and power
CTE	Coefficient of thermal expansion
DSC	Differential scanning calorimeter
EDS	Energy dispersive spectroscopy
FCC	Face centred cubic
FTIR	Fourier-transform infrared spectroscopy
FWHM	Full width at half maxima
GDC	Gadolinium-doped ceria
ICDD	International centre for diffraction data
IS	Interaction study of the cathode with a glass sealant
ISC	Interaction study of the cathode with Crofer interconnect
LPS	Liquid phase sintering
LSM	Lanthanum strontium manganite
MIEC	Mixed ionic and electronic conductor
ORR	Oxygen reduction reaction
PL	Photoluminescence spectroscopy
SBBZ	Glass sealant ($45SiO_2$+$40BaO$+$10B_2O_3$+$5ZrO_2$)
SEM	Scanning electron microscopy
SM	$SrMnO_3$
SMC	$SrMnCuO_3$
SMN	$SrMnNiO_3$
SOFC	Solid oxide fuel cells
SZ	$SrZrO_3$

SZC	$SrZrCuO_3$
SZN	$SrZrNiO_3$
TG-DTA	Thermogravimetric and differential thermal analyzer
TPB	Triple phase boundary
UV	Ultraviolet-visible spectroscopy
XPS	X-ray photoelectron spectroscopy
XRD	X-ray diffraction
YSZ	Yttria-stabilized zirconia

Abstract

Environment-friendly, better efficiency, and fuel flexibility have made solid oxide fuel cells (SOFCs) a popular alternative to conventional combustion energy generating systems. However, despite having many advantages, the wide-scale commercialisation of SOFCs is still hampered by its cost and incompatibility of the different components. High operating temperature (≥1000°C) leads to a higher start-up time with increased electrode kinetics. Therefore, research nowadays is focused on the development of materials for intermediate-temperature (600-800°C) and low-temperature (<600°C) range SOFCs.

Among all the components of SOFC, the cathode is a vital component. It should have mixed conductivity, i.e. electronic and ionic conductivity. Mixed conducting materials have a pronounced effect on the oxygen reduction reaction since their presence increases the triple-phase boundary, thus, lowering the operating temperature, forming the core of this thesis.

Mainly, perovskite-based materials have been studied for use as SOFC cathode materials for a long time due to their ability to accommodate a range of elements from the periodic table, inherent vacant sites and ability to accommodate multiple cations as dopants. Therefore, in this thesis, the effects of transition metal (Cu^{2+} and Ni^{2+}) doping on the structural, thermal and conducting properties of strontium based perovskite (ABO_3) materials ($SrZrO_3$ and $SrMnO_3$) are studied. The doping has been done at the B-site of the ABO_3 type materials to enhance their conducting properties, match coefficient of thermal expansion (CTE), and increase the sinterability of Sr-based perovskites. Selected samples exhibiting comparable structural and thermal properties with a boro-silicate glass sealant and a standard interconnect material are also analysed for structural and thermal compatibility of developed materials. The thesis is divided into seven chapters with an overview in the beginning and a list of cited references at the end of each chapter.

Chapter 1 describes the background of fuel cells, types and geometry of the SOFCs. The advantages and disadvantages of the different fuel cells, their working principle, and different designs are also discussed. The focus of the thesis is primarily to develop cathode materials for SOFC; therefore, the different processing methods are discussed in detail and their effects on the reaction mechanism. Further, the role of doping transition metals is discussed to understand their effect on the structural, thermal and conducting properties of perovskite-structured materials.

Chapter 2 gives a detailed account of the literature related to $SrZrO_3$, $SrMnO_3$ and other perovskite structured materials, along with interaction/interfacial study of different SOFC components. The literature is based on the role of different dopants, structural, thermal and conducting properties. The motivation of the present research work is also discussed in this chapter. Towards the end of the chapter, the objectives of the thesis are defined based on the motivation and literature survey.

Chapter 3 describes the detailed synthesis procedure of $SrM_{1-x}A_xO_{3-\delta}$ (M: Zr, Mn; A: Cu, Ni; $0.00 \leq x \leq 0.20$) and the interaction study of the selected cathode with a glass-sealant and a interconnect (Crofer 22 APU). The samples are characterised using various techniques to study structural, thermal, and conducting properties of synthesised materials. The principle and technical details of the different characterisation techniques, namely X-ray diffraction (XRD), Rietveld refinement, Fourier-transform infrared spectroscopy (FTIR), scanning electron microscopy (SEM) coupled with energy dispersive spectroscopy (EDS), X-ray photoelectron spectroscopy (XPS), dilatometry, thermogravimetric-differential thermal analysis (TG-DTA), impedance analyser, ultraviolet-visible spectroscopy (UV-Vis), photoluminescence spectroscopy (PL) and Vickers hardness are discussed in this chapter.

Chapter 4 deals with the effect of doping Cu and Ni with different concentrations in place of Zr in $SrZrO_3$. This chapter is further divided into two sub-sections. In the first sub-section,

doping of Cu^{2+} is discussed, whereas, in the second section, Ni^{2+} doping is discussed in detail. Doping of transition metals in $SrZrO_3$ induces oxygen vacancies in the crystal lattice necessary for ionic motion. The effect of doping on the structural, thermal and conducting properties is studied. The results are discussed in light of the disordering created by the dopants and their concentrations. The monophasic nature of the samples enhances the conducting properties of the system. Cu^{2+} enhanced the thermal and conducting properties of $SrZrO_3$; however, due to the brittleness of the Ni-doped samples, the conductivity measurement could not be carried out. Both dopings had thermal expansion in the tolerance limit required for SOFCs.

Chapter 5 discusses the effect of different dopings in $SrMnO_3$. The first part gives a detailed account of the effect of doping Cu^{2+} in $SrMnO_3$, and the second part gives information about the effect of Ni^{2+} doping in $SrMnO_3$. The samples are studied in light of the structural transformations, vacancy generation on doping lower valence cation, the presence of secondary phases and thermal changes due to ordering or disordering of the vacancies. The presence of minor phases is detrimental in determining as well as enhancing the conductivity of the samples. However, the thermal expansion of the doped samples is well within the prescribed limit for SOFCs.

Chapter 6 gives a detailed account of the chemical interaction of selected cathode material, i.e. $SrZr_{0.85}Cu_{0.15}O_{3-\delta}$ with a glass sealant and a standard interconnect material. This chapter is divided into two sections. The first section deals with the changes observed at the cathode-sealant interface, while the second section elaborates on the changes at the cathode-interconnect interface. The structural and thermal changes occurring at the interface are studied based on XRD, SEM, and dilatometry results. The interaction with the sealant was successful; however, due to incompatibility of CTE at high temperatures, chemical bonding between the cathode and interconnect could not form.

Chapter 7 accounts for the conclusions drawn from the obtained results on $SrM_{1-x}A_xO_{3-\delta}$ (M: Zr, Mn; A: Cu, Ni; $0.00 \leq x \leq 0.20$) and the interaction study. In all the series, the $SrZr_{1-x}Cu_xO_{3-\delta}$ ($0.05 \leq x \leq 0.20$) is the best cathode material in terms of monophasic nature, CTE and conductivity. The conductivity values vary from 10^{-7} to 10^{-4} S cm^{-1} with increasing Cu dopant concentration and the composition, $SrZr_{0.85}Cu_{0.15}O_{3-\delta}$, has the highest conductivity at 800°C. Interestingly, the CTE of the diffusion couple after exposure of 500 hrs is within the required limit for SOFCs. Additionally, the future scope and suggestions are also given at the end of this chapter.

Overview

Solid oxide fuel cells (SOFCs) have gained popularity due to their flexibility in the choice of fuels and non-emission of toxic gases. However, high operating temperatures limit their use for commercial purposes and also increase their cost. Materials selection plays a vital role in the efficient working of the cell and lowering its operating temperatures. Therefore, this chapter briefly explains the need for fuel cells and the working of different components of SOFC. Since the focus of the present research work is to understand and develop the cathode materials for SOFCs. Therefore, material requirements, the basic structure of the probable materials, reaction mechanism, along with some of the commonly used materials, are also discussed in this chapter.

1.1. Fuel cells

With the growing population, changes in the climate, mass migrations, and pandemics worldwide, the demand and supply of energy consumption are increasing faster than ever. All over the world, there is rigorous competition on developing devices that are high in production and low in producing different pollutants that are harmful to the environment. Because of this, there is a need for sustainable, renewable, and clean electricity-producing devices with enhanced efficiency and free from fossil fuel consumption. Fuel cells in this regard have garnered much attention owing to their simplistic design, which does not have any moving parts. Also, a particular class of fuel cells comprises primarily solid ceramic materials, making them an excellent choice for stationary power applications [1].

Fuel cells are electrochemical energy conversion devices that produce electricity by converting the chemical energy of the fuel and oxidant into electrical energy, heat, and water [2, 3]. Since fuel cells convert chemical energy directly into electricity, they offer many advantages over traditional power sources, such as improved efficiency, greater fuel diversity, and, most importantly, lower negative impacts on the environment [4, 5]. Nations all around the world are signing climate agreements for the reduction of CO_2 and other greenhouse gas emissions. Fuel cells could be one such alternative electricity-producing device that produces clean energy without any release of toxic gases. They can produce electricity as long as fuel (hydrogen, ethanol, methanol, or gaseous fossils fuels like natural gas) and oxidant (oxygen or air) are fed [6, 7].

Fuel cells were discovered long back when Sir William Grove devised a basic fuel cell that operated at room temperature in 1839. It consisted of a hydrogen anode, oxygen cathode, and an electrolyte of dilute sulphuric acid [8]. Fig. 1.1 illustrates the diagrammatic representation of Grove's fuel cell.

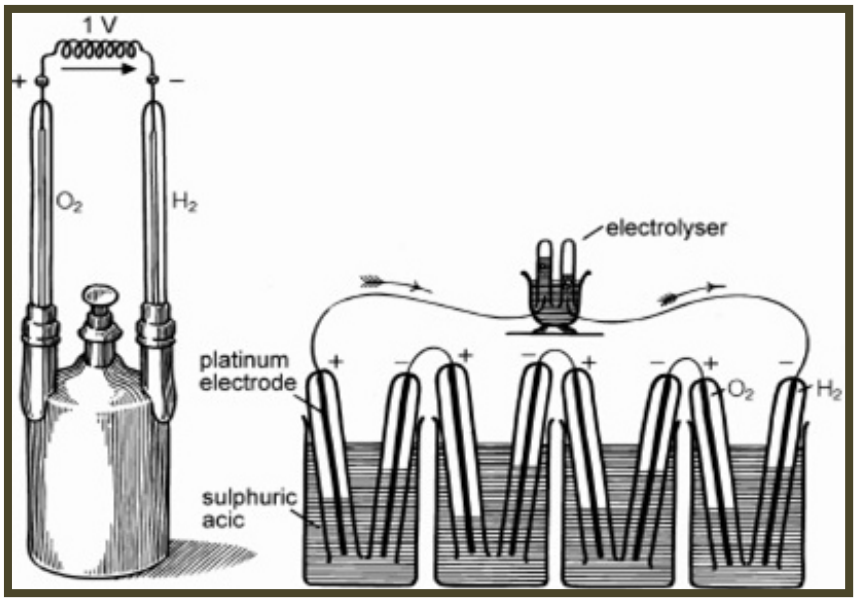


Fig. 1.1 An illustration of the fuel cell devised by Sir William Grove in 1839 [9]

Over time, much development took place, which modified Grove's basic fuel cell. In 1950s, Bacon developed a 5kW stationary fuel cell with the help of nickel gauze electrodes [10]. This work of Bacon led to the development of alkali fuel cells (AFC) in 1958. They are considered the future energy source based on the salient features of the fuel cells. The national aeronautics and space administration (NASA) began developing fuel cell generators for human-crewed space missions in the 1960s. Alkali fuel cell (AFC) was the first fuel cell used in an Apollo spacecraft [11]. The first proton exchange membrane fuel cell (PEMFC) was developed by NASA using platinum as the catalyst. Fuel cells served as the means for electrical power as well as to produce drinking water for astronauts. PEMFC and solid oxide fuel cell (SOFC) technology came into the public eye during the 1990s, majorly for the development of residential micro-combined heat and power (CHP) applications [12, 13]. Since a single fuel cell can produce an output of ~1 Volt only, multiple cells are stacked together to get outputs in W, kW, MW or in terms of power density i.e. ~2 Wcm^{-2} [14]. Fig. 1.2 shows a ~50 kW proof-of-concept SOFC power system fuelled by natural gas.



Fig. 1.2 Demonstration of a ~50 kW proof-of-concept SOFC power system by Fuel Cell Energy [15]

Apart from AFC, PEMFC, and SOFC, there are two other fuel cells: phosphoric acid (PAFC) and molten carbonate fuel cell (MCFC). All these fuel cells are distinguished based on the electrolyte material used and hence named after them. AFC, PAFC, and MCFC have a liquid electrolyte, while PEMFC and SOFC have a solid electrolyte. Since all these fuel cells have different operating temperatures, they are classified as high-temperature fuel cells and low-temperature fuel cells, as shown in Fig. 1.3.

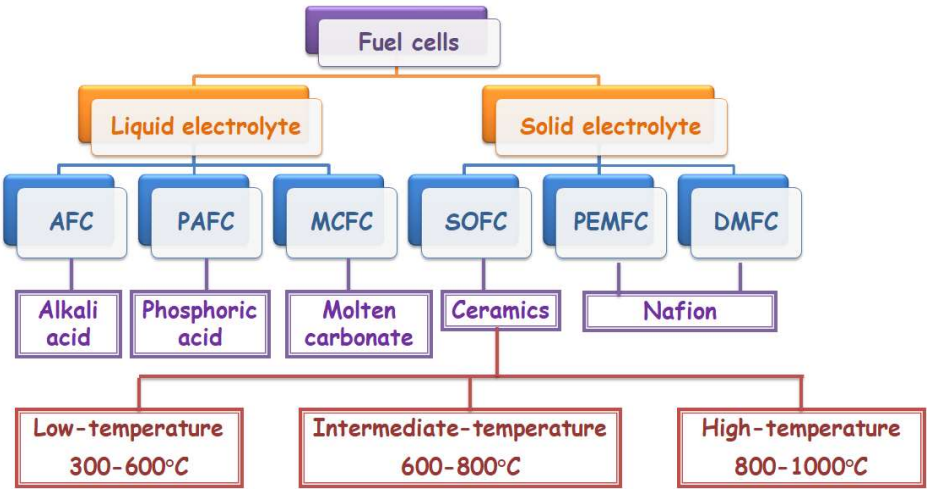


Fig. 1.3 Classification of different fuel cells based on the type of electrolyte and their operating temperature

The AFCs come under low-temperature fuel cells since their operating temperature is between 20°C and 90°C. AFCs make use of potassium hydroxide (KOH) as their electrolyte. Since the electrolyte is liquid, AFCs corrode quickly, which is their significant disadvantage. Another disadvantage is that AFCs must be kept in a CO_2-free environment to minimise electrolyte poisoning [16].

PAFCs make use of phosphoric acid as their electrolyte, as suggested by its name. The charge carriers in this type of fuel cell are the hydrogen ions, H^+ (proton). PAFCs operate in the temperature range of 175-200°C. PAFCs are difficult to manufacture since they require expensive platinum catalyst coating at the electrodes. MCFCs are high-temperature fuel cells with an operating temperature of ~650°C. They use molten carbonate salt mixture as their electrolyte, suspended in a porous, chemically inert ceramic matrix of beta (hexagonal) alumina solid electrolyte (BASE). Management of the electrolyte is a crucial factor for the long-term use of MCFCs. PEMFCs use a thin, permeable polymer sheet as their electrolyte, which acts as an insulator for electrons and a conductor for protons. PEMFCs are low-temperature fuel cells with an operating temperature between 60 and 100°C. The major drawback of PEMFCs is their low efficiency (40-45%) and use of high-cost platinum catalysts [17-19].

1.2. Solid oxide fuel cells

Solid oxide fuel cells (SOFCs) are high-temperature devices with operating temperatures ranging from 600°C to 1000°C. However, high operating temperature causes material degradation. Additionally, the formation of undesired interfacial crystalline phases and change in oxygen partial pressure during operation shortens the lifespan of a SOFC. Varying the electrolyte's thickness and choosing appropriate materials for the different SOFC components can solve the problem. On the other hand, it is advantageous since the catalytic activity of cathode and anode increases with high temperatures. Based on the operating

temperatures (T_o), the SOFCs can be labelled as low-temperature SOFCs (LT-SOFCs), i.e., SOFCs having $T_o < 600℃$, intermediate-temperature SOFCs (IT-SOFCs) i.e. $600℃ \leq T_o \leq 800℃$ and high-temperature SOFCs i.e. $T_o > 800℃$ [20]. SOFCs offer many advantages over other fuel cells such as comparatively high efficiency of ~85%, variety in the type of fuels such as hydrogen, ethanol, methanol, etc., emission of low levels of poisonous fumes such as oxides of nitrogen, sulphur, and carbon, noiseless and free from vibration [21].

A basic SOFC has a dense electrolyte sandwiched between two porous electrodes, namely cathode and anode. Along with these components, there is an interconnect and a glass sealant. The metallic interconnect binds the different cells together and separates the fuel and gases, while the sealant placed between various components acts as a shield to prevent the mixing of the fuel and the oxidant gases. The cathode, also known as the air electrode, is where the gaseous oxygen enters the cell and reacts with the electrons coming from the outer electrical circuit. Here, the oxygen gas gets converted into ions which pass through the electrolyte and move towards the anode or the fuel electrode. At the anode side, the oxygen ions react with hydrogen ions to form H_2O while liberating electrons. These electrons move towards the outer circuit, where they form the source of electricity, as shown in Fig. 1.4.

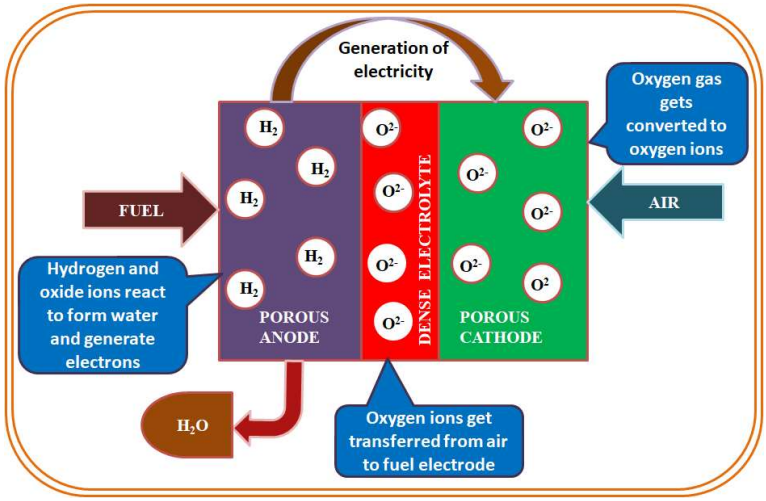


Fig. 1.4 Schematic representation of a SOFC with a detailed description of the different components [22]

Given below are the reactions that take place at both the electrodes:

Cathode: $$^1/_2\, O_2 + 2e^- \rightarrow O^{2-} \quad (1.1)$$

Anode: $$H_2 + O^{2-} \rightarrow H_2O + 2e^- \quad (1.2)$$

Overall reaction: $$H_2 + {}^1/_2\, O_2 \rightarrow H_2O \quad (1.3)$$

These reactions are applicable in the case of oxide-ion conducting SOFCs. There is another type of SOFC in which the primary charge carriers are the H^+ (protons). Therefore, this class of SOFCs is known as the proton-conducting SOFCs. Here, the protons from the anode travel towards the cathode, where they react with oxygen ions to form the same end products as in the case of oxide-ion conducting SOFCs. However, in this case, the reactions take place only in the presence of hydrogen or water vapour atmospheres. The reactions that take place at the cathode and anode in proton-conducting SOFCs are as follows:

Cathode: $$^1/_2\, O_2 + 2H^+ + 2e^- \rightarrow H_2O \quad (1.4)$$

Anode: $$H_2 \rightarrow 2H^+ + 2e^- \quad (1.5)$$

The difference in both cases is in the direction of the reaction procedure and the charge carriers.

1.3. Design and components of a SOFC

Since SOFCs consists of almost all ceramic components, there are multiple ways of constructing them. The most popular ways of designing a SOFC are planar and tubular. Each has its pros and cons in designing and applications point of view. Fig. 1.5 shows the typical planar and tubular SOFC design. The planar SOFC consists of a flat plate anode-electrolyte-cathode layered stack. An additional component, i.e., the sealant, is required to construct the planar design of a SOFC. This type of configuration has a higher power density due to its shorter electrical path and is cost-effective compared to its counterpart. However, the tubular design SOFC is complex, with the electrolyte and electrode layers grown over porous

zirconia or $LaMnO_3$ tube. Fabrication of interconnect is such that it touches the cathode while the cells are connected in series by pushing interconnect over the surface of the anode of the neighbouring cell with the help of nickel felt. Barring one, all the components of the tubular, as well as planar SOFCs, are the same. The following sections give a brief description of the SOFC components.

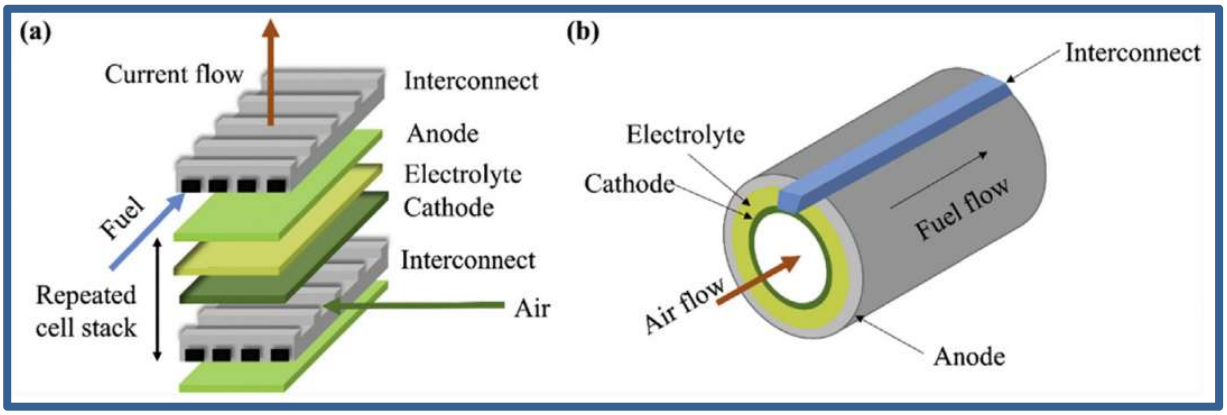


Fig. 1.5 Schematic of (a) planar and (b) tubular design SOFC [23]

1.3.1. Anode

In a SOFC, fuel is supplied to the anode; therefore, it is also known as the fuel electrode. The anode must be able to function in a reducing oxygen/air atmosphere. Depending upon whether the SOFC is anode-supported, the thickness of the anode varies accordingly. The oxidation reaction between the oxygen ions and the hydrogen produces heat as well as water and electricity. If the fuel is a light hydrocarbon, for example, methane, another function of the anode is to act as a catalyst for steam reforming the fuel into hydrogen. It provides another operational benefit to the fuel cell stack since the reaction is endothermic, which cools the stack internally [21]. The reducing conditions combined with electrical conductivity make metals attractive anode candidates. Nickel is the most commonly used anode material for its abundance, affordability, and high catalytic activity. Nickel is often coupled with Y_2O_3-stabilized ZrO_2 (YSZ) and used as an anode [24].

1.3.2. Electrolyte

Once the oxygen gets converted into ions, it migrates through the electrolyte towards the anode. The electrolyte must therefore possess high ionic conductivity with minimum electronic conductivity. It must be fully dense to prevent any short-circuiting of reacting gases through it. It should also be as thin as possible to minimise resistive losses in the cell. Apart from this, the electrolyte must be chemically, thermally, and structurally stable with rising SOFC operating temperature [25-27]. YSZ, doped cerium oxide, doped bismuth oxide, and doped gadolinium oxide are some of the commonly used electrolyte materials. However, YSZ is the most popular electrolyte material due to its high ionic conductivity above 800°C [28].

1.3.3. Interconnect

The purpose of interconnect is to connect individual cells in planar SOFC. The interconnect material should have 100% electronic conductivity with no porosity. Similar to the other SOFC components, it should also have a coefficient of thermal expansion (CTE) close to that of the cathode and anode. Compatibility and inertness towards other fuel cell components since interconnect undergoes simultaneous exposure to the anode's reducing environment and the cathode's oxidising atmosphere. Depending upon the operating temperatures, the choice of interconnect materials varies. At the operating temperatures of ~900-1000°C, interconnects are made up of alloys such as Inconel 600 and Crofer 22 APU. At or below 800°C, ferrite steels can be used as interconnects, while stainless steel is used below 700°C since they are comparatively inexpensive and readily available [29].

1.3.4. Sealant

As discussed in Section 1.2, sealants are an essential component of a planar SOFC since they provide a barrier in preventing the mixing of the fuel with the oxidant (Fig. 1.6).

Sealants should be able to withstand variable atmospheres. They should be chemically and thermally stable while having compatible CTE with other SOFC components. There are two types of sealants, namely compressive and rigid seals. The main distinction between these two is the CTE matching requirement with other components [30]. Since the compressive seals are tightly attached to the other components, they do not require exact CTE matching. However, for the rigid seals, CTE matching is a necessary condition to be satisfied. Silver and mica-based metal gaskets are generally used as compressive seals; however, glasses and glass-ceramics are used as rigid seals [31].

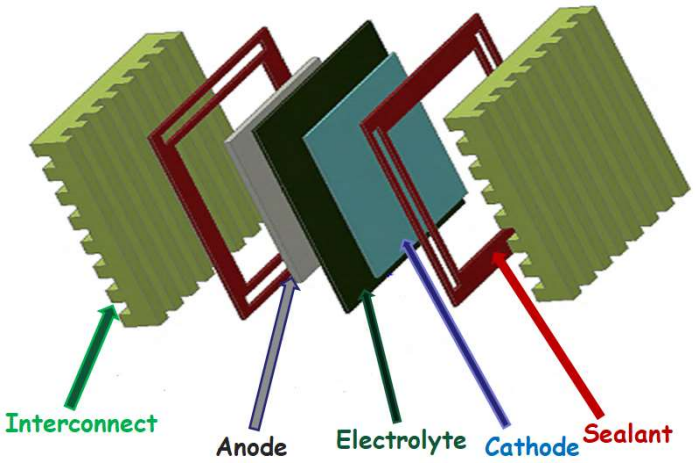


Fig. 1.6 Schematic representation of the planar design SOFC components [32]

1.3.5. Cathode

The cathode (air electrode) is a porous layer over the electrolyte where the reduction of the oxygen gas into ions takes place. As stated above, depending on whether the SOFC is cathode supported or anode supported, the thickness of the electrode varies accordingly [33]. A peculiarity of the cathode materials is that they should be both electronically and ionically conductive since both ions and electrons are present at the cathode [34]. Lanthanum strontium manganite (LSM) is a popular cathode material because of its compatibility with doped zirconia (ZrO_2) electrolytes. LSM has a low level of chemical reactivity with YSZ, which extends its lifetime. Although LSM works well as a cathode at high operating

temperatures, its performance degrades as the operating temperature is lowered below 800°C [35, 36]. Since LSM is a poor ionic conductor, the electrochemically active region is limited to the triple-phase boundary (TPB). TPB is the junction where the oxygen gas, electrons from the cathode, and ions from the electrolyte meet, as shown in Fig. 1.7.

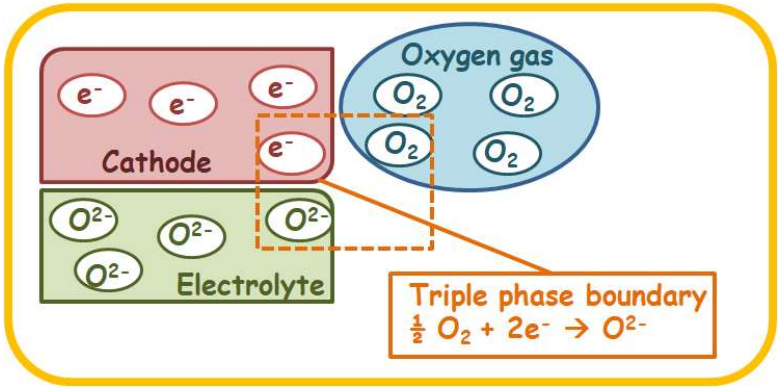


Fig. 1.7 Diagrammatic illustration of the TPB in the vicinity of which the oxygen reduction reaction (ORR) takes place [22]

A potential cathode material must conduct both electrons and oxygen ions to increase the reaction zone beyond the TPB. Therefore, the ionic conductivity should be between 10^{-1} to 10^{-4} Scm^{-1}, while the electronic conductivity should be ≥100 Scm^{-1} [21]. Composite cathode materials such as LSM-YSZ are used to increase this TPB length. However, defects induced perovskite and related structures exhibiting mixed ionic and electronic conduction are popular cathode material choices [34, 37, 38].

Apart from the mixed ionic and electronic conductivity (MIEC), another critical parameter to be satisfied by a cathode material is the thermal expansion. It is a well-known fact that materials either expand or contract on heating. The CTE is a measure of this change in the length of the material. As the SOFC undergoes various thermal cycles during the operation, any mismatch between the CTEs of the different components leads to cracking the components. To avoid this, the CTE of all the SOFC components should be matchable or in tolerance limit. The CTE of the standard electrolyte materials decides the appropriate CTE

range for other SOFC components. Therefore, CTE between 9-13×10^{-6} $°C^{-1}$ is found suitable for SOFC electrode materials [39, 40]. Since the cathode is a mixed conductor; consequently, it should be porous enough for the smooth passage of the electrons and the oxide ions. The materials need to be chemically stable to avoid disturbing stoichiometry. The materials should have catalytic properties to speed up the electrochemical reactions [25, 41]. Fig. 1.8 depicts the schematic of the required SOFC cathode material properties.

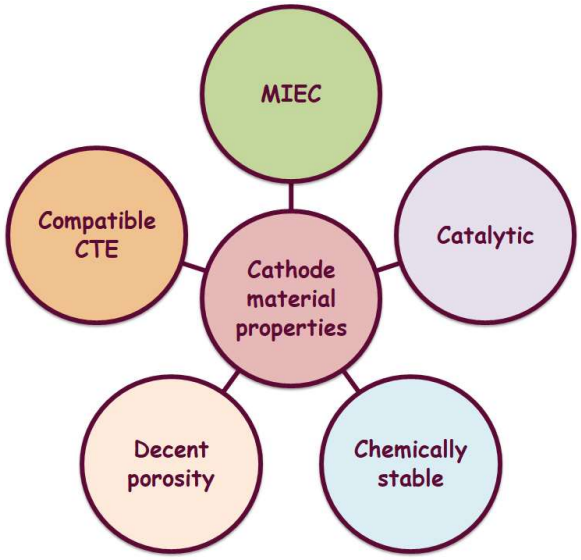


Fig. 1.8 Essential cathode material properties for SOFC [22]

1.4. Reaction mechanism at the cathode

The electrochemical reactions that occur at the cathode have a substantial impact on the overall performance of the SOFC. The first and foremost step for the reactions is converting the oxygen gas (O_2) into the electrochemically active oxygen anions (O^{2-}). This step involves several different processes such as adsorption, dissociation, reduction, and incorporation of the O^{2-} into the lattice of the cathode materials. After this is the transportation of the anionic species towards the electrolyte, this process takes place via cathode, which is why the cathode should have good porosity to allow a substantial amount of diffusion. Once the O^{2-} reaches over to the electrolyte, they jump onto its lattice. The reduction of the O_2 into the O^{2-} is

known as the oxygen reduction reaction (ORR). It is the major contributor to total cell resistance [42].

Broadly, there are three major pathways through which these reactions take place [43]. Fig. 1.9 shows the electrochemical reactions taking place via the electrode surface path (pure electronic cathode), electrolyte surface path (composite cathode), and bulk path (MIEC cathode), respectively. The electrochemical reactions can take place via any of these three pathways. However, for the reactions to occur faster, it is generally preferred to have MIEC cathodes since they help increase the area of reaction beyond the TPB.

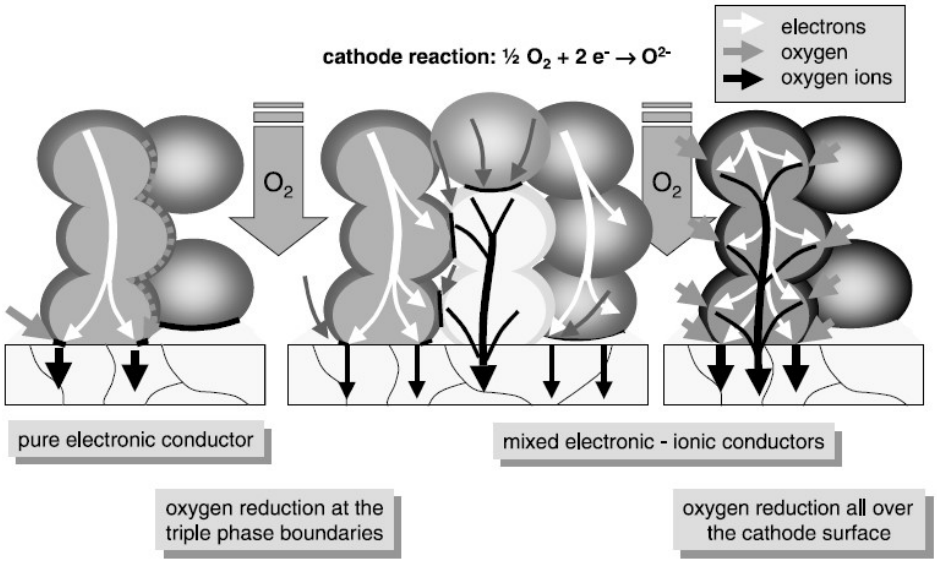


Fig. 1.9 Diagrammatic representation of the ORR in a pure electronic cathode, a composite cathode, and a mixed conducting cathode, respectively [44]

1.5. Role of transition metals doping in perovskite-structured materials

Perovskite and related structured materials have been long-time favourites when choosing materials for SOFC components [39, 45-47]. These materials are a popular choice for SOFC components due to the uniqueness of their structure and ability to accommodate most of the periodic table elements. As shown in Fig. 1.10**,** an elementary perovskite structure consists of an anion (generally O^{2-}) and two different ionic radii cations (A and B).

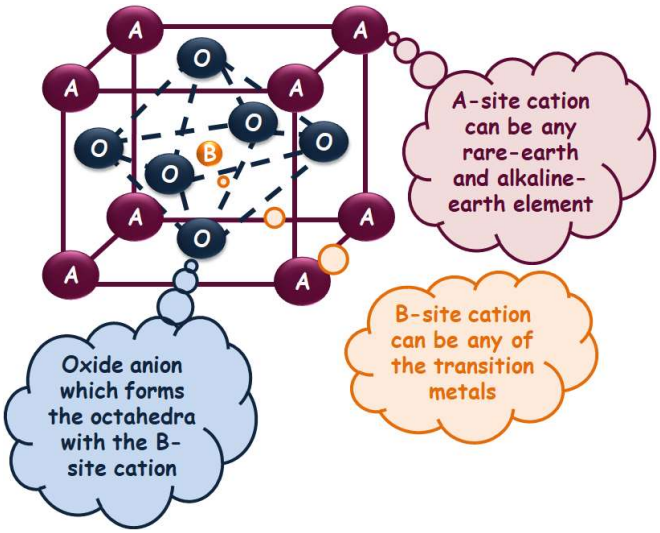


Fig. 1.10 A diagrammatic representation of a basic perovskite oxide [48]

The chemical formula describing a perovskite structure is ABO_3. The larger A-site cations are placed at the cube's corners, while the smaller B-site cation is at the body centre. The O^{2-} ions at each face of the cube. The perovskite-structured oxides are generally distorted since most of the periodic table elements do not satisfy the requirements for forming an ideal arrangement. Therefore, the following Goldschmidt's tolerance factor gives the degree of distortion from the cubic symmetry:

$$t = \frac{r_A + r_B}{\sqrt{2}\,(r_B + r_O)} \tag{1.6}$$

where r_A, r_B and r_O are the ionic radii of the A-site, B-site cations, and oxygen anion, respectively [49]. Furthermore, in the case where two elements are present, either A or B-site, instead of using r_B in equation (1.6), $\frac{r_B + r_{B'}}{2}$ can be used. The deviation from the cubic symmetry results in the tilting of the BO_6 octahedral. Therefore, the bond angle between the B-site cation and the oxygen anion decreases, leading to the formation of other structures. The values of t given in Table 1.1 determine the symmetry of the system.

Table 1.1 Goldschmidt's tolerance factor and corresponding associated symmetry along with is the cation size

Goldschmidt's tolerance factor (*t*)	Symmetry	Cation size
0.75-0.9	Orthorhombic/Rhombohedral	A is small
0.9-1.0	Cubic	A and B fit perfectly
>1.0	Hexagonal/Tetragonal	A is massive

The A-site cations are generally the rare-earth and alkaline-earth elements (La, Ca, Ba, Sr, etc.), while the B-site cations are the transition metals (Mn, Fe, Co, Ti, etc.) [50]. The different SOFC properties can be altered by doping various elements at the cationic sites or combined at A and B-sites. Doping creates charge imbalance in the system, which is compensated either by the increase in the valence state of the B-site cation causing electronic contribution or by the formation of oxygen vacancies responsible for the ionic (protonic) conduction [50, 51]. The oxide ion conductors turn protonic in hydrogen-containing atmospheres. Water from the gas phase dissociates into a hydroxide ion and a proton. The hydroxide ion fills the oxide ion vacancy while the proton forms a covalent bond with the lattice oxygen [52, 53].

Apart from oxygen vacancies, the ionic conductivity is highly dependent on the geometric factors since the ionic conductivity decreases on moving from most symmetric structures to less symmetric crystal structures [54]. Doping could either be intrinsic or extrinsic. Point defects, vacancies, Schottky and Frenkel defects are the intrinsic vacancies essential for the ionic conduction [55]. The extrinsic defects are the ones created by the introduction of impurities. The doping of a smaller or larger ionic radii dopant in place of a larger or smaller ionic radii host with different valence states results in oxide ion vacancies or oxide ion excess, respectively. Generally, Kroger-Vink notations represent these additions. For

example, doping of Cu^{2+} in place of Zr^{4+} generates defects in the systems represented by the following equation [55]:

$$CuO \rightarrow Cu''_{Zr} + O_o^X + V_o^{\cdot\cdot} \quad (1.7)$$

The following equation represents the defect equilibrium:

$$\frac{1}{2} O_2\,(g) + V_o^{\cdot\cdot} \leftrightarrow O_o^X + 2h^{\cdot} \quad (1.8)$$

In these equations, Cu''_{Zr} denotes Cu at the Zr site, O_o^X represents the oxygen ion at the lattice and $V_o^{\cdot\cdot}$ represents the vacant oxygen site (as discussed above). As the partial pressure of oxygen increases, pure ionic conduction plays a vital role in the total conductivity of the system. The change in the valence state of the transition metals acts as a hopping site for the electrons and holes, which account for n-type and p-type conductivity, respectively. The hopping mechanism occurs through the transition metal to oxygen to transition metal chain commonly known as the B-O-B chain in the ABO_3 structure [56]. Both ionic and electronic conduction in these materials makes them suitable for use as electrodes in SOFC.

Numerous perovskite-based materials have been used as cathode materials for SOFCs. Perovskite materials are distinguished based on A-site, B-site as well as the type of dopants. Different materials serve different purposes based on the properties they satisfy. For example, compositions containing cobalt such as $PrBa_{1-x}Sr_xCo_2O_{5+\delta}$ and $NdBa_{0.5}Sr_{0.5}Co_{2-x}Mn_xO_{5+\delta}$ have very high conductivity ~3000 Scm^{-1} [57, 58]. However, these materials also exhibit high CTE values $>22\times10^{-6}$ $°C^{-1}$ which causes cracking of the electrolyte and delamination at the cathode/electrolyte interface [44]. Gradually, Fe-based materials got popularity since their CTE was comparatively lower than the Co-based materials due to their stable $3d^5$ configurations and a lower chance of conversion from Fe^{3+} to Fe^{4+} [59]. Observing the merits of these materials, co-doping of Co and Fe-based materials yielded extraordinary results. The combination turned out to be advantageous for mixed ionic and electronic conduction since

cobalt enhanced the electronic conduction while iron promoted the ionic conduction in $Ba_{0.5}Sr_{0.5}Co_{0.8}Fe_{0.2}O_{3-\delta}$ [60, 61]. Similarly, to date, many materials are used as cathodes for SOFC [62, 63]. So, the latest development in various cathode materials particularly, Sr-based materials, are given and discussed in the next chapter.

References

[1] M. Farooque, H.C. Maru, Proc. IEEE 89 (2001) 1819-1829.

[2] J. Larminie, A. Dicks, Second ed., John Wiley & Sons, West Sussex (UK), 2003.

[3] S.C. Singhal, Electrochem. Soc. Interface. (2007) 41-44.

[4] S.C. Singhal, Solid State Ion. 135 (2000) 305-313.

[5] S.C. Singhal, K. Kendall, First ed., Elsevier, Oxford (UK), 2003.

[6] S.M. Haile, Acta Mater. 51 (2003) 5981-6000.

[7] B.C.H. Steele, Nature 400 (1999) 619-621.

[8] A.J. Appleby, J. Power Sources 29 (1990) 3-11.

[9] P.G. Grimes, IEEE AES Systems Magazine 15 (2000) 7-10.

[10] J.M. Andujar, F. Segura, Ren. Sustain. Energy Rev. 13 (2009) 2309-2322.

[11] A.B. Stambouli, E. Traversa, Renew. Sustain. Energy Rev. 6 (2002) 433-455.

[12] S.C. Singhal, Solid State Ion. 152-153 (2002) 405-410.

[13] E. Fontell, T. Kivisaari, N. Christiansen, J.B. Hansen, J. Palsson, J. Power Sources 131 (2004) 49-56.

[14] N.Q. Minh. Second ed., Acad. Press, Cambridge (USA), 2016.

[15] S.D. Vora, G. Jesionowski, M.C. Williams, ECS Trans. 91 (2019) 27-39.

[16] K. Kordesch, V. Hacker, J. Gsellmann, M. Cifrain, G. Faleschini, P. Enzinger, R. Fankhauser, M. Ortner, M. Muhr, R.R. Aronson, J. Power Sources 86 (2000) 162-165.

[17] N. Sammes, R. Bove, K. Stahl, Curr. Opin. Solid State Mater. Sci. 8 (2004) 372-378

[18] W. Sangarunlert, S. Suhchai, A. Nathakaranakule, Int. J. Renew. Energy 3 (2008) 39-47.

[19] S.J. Peighambardoust, S. Rowshanzamir, M. Amjadi, Int. J. Hydrog. Energy 35 (2010) 9349-9384.

[20] J. Richter, P. Holtappels, T. Graule, T. Nakamura, L.J. Gauckler, Monatsh. Chem. 140 (2009) 985-999.

[21] P.S. Devi, A.D. Sharma, H.S. Maiti, Trans. Indian Ceram. Soc. 63 (2004) 75-98.

[22] P. Kaur, K. Singh, Ceram. Int. 46 (2020) 5521-5535.

[23] K.H. Ng, H.A. Rahman, M.R. Somalu, Int. J. Hydrog. Energy 44 (2019) 30692-30704.

[24] J.W. Fergus, Solid State Ion. 177 (2006) 1529-1541.

[25] N. Mahato, A. Banerjee, A. Gupta, S. Omar, K. Balani, Prog. Mater. Sci. 72 (2015) 141-337.

[26] C. Xia, in: J.W. Fergus, R. Hui, X. Li, D.P. Wilkinson, J. Zhang (eds.), Taylor & Francis Group, Boca Raton (USA), 2009.

[27] R.N. Basu, Anamaya Publishers, New Delhi (India), 2007.

[28] V.V. Kharton, F.M.B. Marques, A. Atkinson, Solid State Ion. 174 (2004) 135-149.

[29] J.W. Fergus, Solid State Ion. 171 (2004) 1-15.

[30] K. Singh, T. Walia, Int. J. Energy Res. (2021) 1-24.

[31] J.W. Fergus, J. Power Sources 147 (2005) 46-57.

[32] M.K. Mahapatra, K. Lu, J. Power Sources 195 (2010) 7129-7139.

[33] C. Zuo, M. Liu, M. Liu, in; M. Aparicio et al. (eds.), Springer Science+Business Media, New York (USA), 2012.

[34] SK. Burnwal, S. Bharadwaj, P. Kistaiah, J. Mol. Engg. Mater. 4 (2016) 1630001(1)-(7).

[35] S.P. Jiang, J. Mater. Sci. 43 (2008) 6799-6833.

[36] Z. Shao, W. Zhu, Z. Zhu, Prog. Mater. Sci. 57 (2012) 804-874.

[37] R. O'Hayre, D.M. Barnett, F.B. Prinz, J. Electrochem. Soc. 152 (2005) A439-A444.

[38] R. O'Hayre, S.W. Cha, W. Colella, F.B. Prinz, John Wiley & Sons, New Jersey (USA), 2016.

[39] C. Sun, R. Hui, J. Roller, J. Solid State Electrochem. 14 (2010) 1125-1144.

[40] F. Tietz, Ionics 5 (1999) 129-139.

[41] WNAW Yusoff, N.W. Norman, A.A. Samat, M.R. Somalu, A. Muchtar, N.A. Baharuddin, J. Adv. Res. Fluid Mech. Therm. Sci. 50 (2018) 153-160.

[42] S.B. Adler, Chem. Rev. 104 (2004) 4791-4843.

[43] J. Fleig, Annu. Rev. Mater. Res. 33 (2003) 361-382.

[44] A. Weber, E.I. Tiffee, J. Power Sources 127 (2004) 273-283.

[45] S.J. Skinner, Int. J. Inorg. Mater. 3 (2001) 113-121.

[46] A.J. Jacobson, Chem. Mater. 22 (2010) 660-674.

[47] A. Jun, J. Kim, J. Shin, G. Kim, ChemElectroChem 3 (2016) 511-530.

[48] P. Kaur, K. Singh, in: M. Jeguirim (ed.), Elsevier, Amsterdam (Netherlands), 2021.

[49] V.M. Goldschmidt, Die Naturwissenschaften 14 (1926) 477-485.

[50] S.J. Skinner, J.A. Kilner, Mater. Today 6(3) (2003) 30-37.

[51] V. Thangadurai, W. Weppner, Ionics 12 (2006) 81-92.

[52] T. Yajima, H. Suzuki, T. Yogo, H. Iwahara, Solid State Ion. 51 (1992) 101-107.

[53] R.A. Davies, M.S. Islam, J.D. Gale, Solid State Ion. 126 (1999) 323-335.

[54] J. Ranlov, PhD thesis, Technical University of Denmark, Kongens Lyngby (Denmark), 1995.

[55] P.J. Gellings, H.J.M. Bouwmeester, CRC Press, Boca Raton (USA), 1997.

[56] N. Orlovskaya, N. Brouwning, Springer Science+Business Media, New York (USA), 2012.

[57] J.H. Kim, J.T.S. Irvine, Int. J. Hydrog. Energy 37 (2012) 5920-5929.

[58] J. Kim, S. Choi, S. Park, C. Kim, J. Shin, G. Kim, Electrochim. Acta 112 (2013) 712-718.

[59] S.P. Simner, J.F. Bonnett, N.L. Canfield, K.D. Meinhardt, J.P. Shelton, V.L. Sprenkle, J.W. Stevenson, J. Power Sources 113 (2003) 1-10.

[60] Y. Guo, Y. Zhou, D. Chen, H. Shi, R.R.Z. Shao, J. Power Sources 196 (2011) 5511-5519.

[61] J.P. Martınez, D.M. Lopez, J.C.R. Morales, P. Nunez, C.S. Bautista, A.J.S. Garcia, J.C. Vazquez, Int. J. Hydrog. Energy 34 (2009) 9486-9495.

[62] A. Aguadero, L. Fawcett, S. Taub, R. Woolley, K. Wu, N. Xu, J.A. Kilner, S.J. Skinner, J. Mater. Sci. 47 (2012) 3925-3948.

[63] J. Kim, S. Choi, A. Jun, H.Y. Jeong, J. Shin, G. Kim, ChemSusChem 7(6) (2014) 1669-1675.

Overview

Material development is a critical factor in the fabrication of the SOFC. This chapter aims to understand the type of materials used as SOFC cathodes. Generally, perovskite-structured materials (ABO_3) are used as SOFC cathodes; however, there are different categories based on A and B-site and the chemical nature of dopants. In this chapter, various perovskite-structured materials are reviewed for their structural, thermal, and conducting properties. In the last, the motivation and objectives of the present study are also given.

2.1. Introduction

Mostly the research is carried out on developing materials for different SOFC components, particularly in the intermediate-temperature range, i.e. 600-800°C. In this section, a review of the perovskite-structure related materials, particularly Sr-based materials, is discussed. Sr-doped $La_{1-x}Sr_xMnO_3$ (LSM) is an extensively used cathode material since the doping effectively increases the electron-hole concentration and thus improves the electronic conductivity [1]. However, the conductivity of LSM increases only till 30 mol% of Sr, after which is a formation of a detrimental $La_2Zr_2O_7$ pyrochlore phase at the interface of LSM and YSZ electrolyte [2]. Various researchers carried out the doping of La, Pr, Nd, Sm, Gd, Yb and Y in $Ln_{0.6}Sr_{0.4}MnO_3$ to avoid forming such insulating phases [3]. The results revealed that $PrMnO_3$ exhibited a CTE of ~12×10^{-6} K^{-1} comparable with YSZ electrolyte. Also, Sr-doping in $Pr_{1-x}Sr_xMnO_3$, $Nd_{1-x}Sr_xMnO_3$ and $Sm_{1-x}Sr_xMnO_3$ inhibited the growth of undesired pyrochlore phases at the cathode-electrolyte interface [4].

Cobalt-containing compositions usually have high ionic and electronic properties than other cathode materials. $La_{1-x}Sr_xCoO_{3-\delta}$ exhibits marked electrode activity due to high oxygen diffusivity and high diffusivity of oxygen molecules. However, it also has a large CTE and high reactivity with YSZ [5]. Substitution of La with Gd or Pr results in the decreased CTE and area-specific resistance (ASR) of the system. A decrease in the CTE of $Ln_{0.6}Sr_{0.4}CoO_{3-\delta}$ where Ln=La, Pr, Nd, Sm and Gd was observed moving from La to Gd. Similar results were observed for $Ln_{1-x}Sr_xMnO_3$ and $Ln_{0.8}Sr_{0.2}Fe_{0.8}Co_{0.2}O_3$ [6, 7]. The conductivity and catalytic activity of (La, Sr) (Co, Cu)$O_{3-\delta}$ was enhanced by doping Cu in place of Co-site. The electrode interfacial conductivity of (La, Sr) (Co, Cu)$O_{3-\delta}$ was 15.32 Scm^{-1} at 800°C in air. Also, Cu addition eliminated the phase transformations with no reduction of the CTE [8].

Compositions having structures related to perovskites have also been studied extensively. Zhou et al. investigated $LaSrMnCoO_{5+\delta}$ and found it to have electrical conductivity between

111-140 Scm^{-1} at 600-850℃ and a CTE of ~15.8×10^{-6} K^{-1} between 30-1000℃. Although the conductivity is comparable; however, the CTE is on the higher side than standard electrolyte materials [9-11]. Generally, it is observed that the lanthanum-series elements are present at the A-site. Doping of lanthanum-based materials with decreasing ionic radii decreases oxygen content, CTE, and electrical conductivity. Reduction in CTE values is due to the decreasing iconicity of the Ln-O bond on the cost of the covalent bond, whereas the decrease in the electrical conductivity is due to the bending of the O-Co-O bonds. In other words, the bond angle changes between Co and oxygen coordinated octahedrally [12].

Higher amount of cobalt results in the delamination at the cathode/electrolyte interface and the cracking of the electrolyte due to increased CTE. Lanthanum ferrites are more stable than cobaltite perovskites since Fe^{3+} ions have a stable electronic configuration. Ralph et al. [13] studied the area-specific resistance and CTE of $La_{0.8}Sr_{0.2}FeO_3$ and observed that the ASR decreased to 0.1 Ω cm^2. The CTE of this composition matched that of CGO and YSZ. Even after 500 hours (hrs) of operation, this material did not degrade. Cu-doped lanthanum strontium ferrites show superior performance for the electrochemical reduction of oxygen. The current densities of the cells with $La_{0.7}Sr_{0.3}Cu_{0.2}Fe_{0.8}O_3$ as a cathode are approximately two to three times higher than $La_{0.7}Sr_{0.3}FeO_3$ [14]. The electrochemical investigations of $La_{0.8}Sr_{0.2}Zn_xFe_{1-x}O_{3-\delta}$ (x=0.1-0.3) showed remarkable electrochemical activity with electrical conductivity of 13.63 Scm^{-1} at 550℃. The fuel cell demonstrated good stability by continuously running for 10 hrs on commercially available natural gas [15].

Most of the work carried out on the lanthanum manganite materials is through doping at the A-site. However, doping at the B-site introduces non-stoichiometric defects in the perovskite lattice, which help increase the ionic conduction. Ti-doped $SrFe_{1-x}Ti_xO_{3-\delta}$ (x=0.00-0.15) exhibit decreasing conductivity of 64, 72, 52 and 41 Scm^{-1} with the increasing dopant concentration i.e. x=0, 0.05, 0.10 and 0.15, respectively [16]. The conductivity of the samples

shows a shift from semiconducting to metallic behaviour. Also, the CTE of the samples decreases from 26.5×10^{-6} K^{-1} to 22.9×10^{-6} K^{-1} with the increase in the Ti content. However, it is still comparable with other Ti and Fe based compositions such as $La_{1-x}Sr_xFe_{1-y}Ti_yO_{3-\delta}$, $Sr_{0.97}Ti_{1-x}Fe_xO_{3-\delta}$ and $La_{0.6}Sr_{0.4}Ti_xFe_{1-x}O_{3-\delta}$ [17-19]. The decrement in the CTE indicates that the Ti-O bond is stronger than the Fe-O bond. Apart from Ti, Cu doping enhances the conductivity of $SrFeO_3$ effectively [20]. The conductivity of $SrFe_{0.7}Cu_{0.3}O_{3-\delta}$ increases from 25 to 54 Scm^{-1} between 500-800°C. Also, the CTE of the system exhibits an average value of 13.8×10^{-6} $K^{-1,}$ which is compatible with $Ce_{0.9}Gd_{0.1}O_{1.95}$ (GDC) electrolyte. Thus, comparing Cu with Ti, it is concluded that doping of Cu instead of Ti decreases the CTE of the system drastically while the conductivity of the system is not much affected.

Ding et al. [21] studied the crystal structure, chemical compatibility, CTE and electrochemical properties of $Sr_{0.7}Y_{0.3}CuO_{2+\delta}$. The samples exhibit a CTE of 11.1×10^{-6} K^{-1} between 25-800°C, which is compatible with SDC electrolyte having CTE ~12.1×10^{-6} K^{-1}. Kharton et al. [18] evaluated the thermal and transport properties of $SrTi_{1-x}Fe_xO_{3-\delta}$. The samples have CTE between 11-13×10^{-6} K^{-1} in the temperature range of 300-700°C. An increase in the Fe concentration at the B-site of $SrTiO_3$ leads to increased ionic and electronic conductivity. It is due to the decrease in the cubic unit cell volume and ion transference number being <0.1 of such materials. Overall, the CTE of these systems is much lower than cobalt-based materials such as $Ln_{0.6}Sr_{0.4}CoO_{3-\delta}$ and $LnBaCo_2O_{5+\delta}$ [12, 22]. Apart from these materials, $SrZrO_3$ and $SrMnO_3$ promise SOFC cathode materials. Therefore, the following sections give the literature survey related to strontium zirconate and strontium manganite.

2.2. $SrZrO_3$ materials

The crystal structure and phase transitions of $SrZrO_3$ have been studied using different experimental techniques. The crystal structure is determined using X-ray diffraction (XRD) and neutron powder diffraction method, while the phase transitions are evaluated using

differential scanning calorimetry (DSC), variable temperature-dependent XRD and dilatometry. Initially, it was observed that $SrZrO_3$ has an orthorhombic structure, but with further progress in the research, it was observed that the crystal structure changes from orthorhombic to tetragonal at high temperature. In general, $SrZrO_3$ undergoes three reversible phase transformations, namely, orthorhombic with space group (*Pnma*) to tetragonal (*I4/mcm*) to ideal cubic structure (*Pm3m*) at 700℃, 1000℃ and 1150℃, respectively. However, an intermediate orthorhombic phase (*Cmcm*) was also observed [23, 24]. Ligny et al. [25] studied the thermal expansion and heat capacity over a wide range of temperatures and found a sharp anomaly near the phase transition temperature. Kennedy et al. [26] studied the evolution of the crystal structure of $SrZrO_3$ at high temperatures (>1087℃) using powder neutron diffraction and the Rietveld refinement method. The analysis confirmed that a first-order intermediate orthorhombic phase with the space group *Cmcm* exists at 727℃ and after which there is a continuous transition from tetragonal (*I4/mcm*) to cubic (*Pm3m*) phase. Fujimori et al. [27] explained the various high-temperature phase transitions using Raman spectroscopy.

Hasegawa et al. [28] studied the structural phase transitions of $SrZrO_3$ were observed at 769℃, 846℃ and 1102℃ using differential scanning calorimetry (DSC) high-temperature XRD and dilatometry. The DSC results observed between room temperature to 1200℃ resulted in a second order, first order and again a second-order phase 769℃, 846℃ and 1102℃ respectively. The linear and volume CTEs were also calculated using dilatometry. It was seen that the volume CTEs were about three times greater than the linear CTEs. These results were in sync with the XRD results, which demonstrate that with the increase in the temperature, structural phase transitions occur, which vary from primitive orthorhombic (*Pm3m*) to body-centred orthorhombic (*Ibmm*) to tetragonal (*I4/mcm*) and finally to the cubic (*Pm3m*) phase.

Zhao et al. [29] studied the thermal expansion of $SrZrO_3$ using high-temperature XRD up to 1200°C. It was observed that the tilting of BO_6 octahedra induced volume change which is denoted by excess volume, while the corresponding thermal expansion denotes excess thermal expansion for a lower symmetry phase to the cubic phase. It was observed that the contribution to the thermal expansion of the A-site cation of the cubic phase is negligible in comparison to that of the B-site cation. Misra et al. [30] studied the electrical conductivity and oxygen sensing behaviour of $SrZr_{1-x}Fe_xO_{3-\delta}$ (x=0-0.2) ceramics. The electrical conductivity of the pellets was investigated under three different oxygen partial pressures, namely, 100% oxygen, 21% O_2 in air and argon containing 10(±2) ppm of O_2. The composition depicted a semiconducting behaviour with the increase in temperature. The electrical conductivity of the samples was calculated to be ~10^{-9} to 10^{-8} Scm^{-1} in the temperature range 200-527°C. Compositions with x=0.1 and x=0.2 exhibited a maximum change in conductivity around 400°C. Fe has ionic radii (0.645Å) comparable to Zr (0.72Å), which is why Fe is substituted in place of Zr in this system. With the increase in the concentration of iron, a linear reduction in the lattice parameters was observed, whereas there was an increase in the conductivity values. Structural, dielectric and magnetic properties of $SrZrO_3$ and $SrZr_{0.9375}Fe_{0.0625}O_3$ were investigated by Tang et al. [31]. The microstructural analysis revealed that with the introduction of iron, the grain size decreased. It implies that higher content of iron inhibits grain growth or increases the crystallisation temperature of $SrZrO_3$. As for the dielectric constant and loss, there was an increase in both values with the introduction of Fe.

Borkar et al. [32] studied the conductivity phenomenon of $SrZrO_3$. The impedance spectroscopy measurements revealed that at elevated temperatures, the conductivity of $SrZrO_3$ was due to the presence of grain and grain boundaries. For temperatures >327°C, the grain and grain boundaries become conducting. The activation energy of $SrZrO_3$ was between

0.7-1.2eV, suggesting ionic and protonic conduction. The physical and electrical properties studied by Muhamad et al. [33] revealed high dielectric constant and conductivity of $SrZrO_3$. The dc conductivity of $SrZrO_3$ varied between 5.3×10^{-9} and 5.2×10^{-6} Scm^{-1}. Since the conduction phenomenon was dominant between 10 Hz to 10 kHz, it was concluded that the major contribution to the conduction phenomenon is by the grain boundaries. Muller et al. [34] verified the existing defect structure of yttrium-doped $SrZrO_3$. The study aimed to identify the majority charge carriers in different atmospheres such as hydrogen and oxygen and different temperature conditions. The results revealed the presence of proton, hole and oxygen vacancy in the conduction phenomenon. Osaka et al. [35] did the thermal and structural study of Yb-doped $SrZrO_3$. The DTA results revealed a broad endothermic peak at 812°C, accompanied by a small weight loss due to the oxygen mass loss. Substitution of Yb^{3+} in place of Zr^{4+} yielded oxide ion vacancies. The XRD patterns revealed single-phase formation and decreased difference of the subcell volume on doping due to the mass loss of oxygen at high temperature, justifying the DTA results.

Shi et al. [36] utilised density functional theory (DFT) to understand doping effects on the proton incorporation and protonic conductivity of Al, Sc, Ga, Y, Rh, In, and Yb-doped $SrZrO_3$. It was observed that doping leads to a large local distortion around hydrogen and dopant ions, thus affecting the protonic conduction. The results show that the DFT geometries optimisations can reproduce the local lattice distortion induced by doping trivalent ions and hydrogen into $SrZrO_3$. Overall the dopants, Yb and Y were effective dopant ions which improved the protonic conduction in $SrZrO_3$.

Juaristi et al. [37] studied the effect of sintering temperature on the crystal structure, microstructure and electrical properties of 4 mol.% ZnO doped $SrZr_{0.9}Y_{0.1}O_{3-\delta}$. ZnO doping effectively increased the densification of $SrZrO_3$ to ~97% at 1300°C. Zn is located on the lattice sites and acts as an acceptor dopant that considerably improves the bulk conductivity

in the dry atmosphere due to greater oxygen-vacancy concentration and wet atmospheres by filling the vacancies through protonic defects. The grain boundary conductivity improvement is due to the enhanced concentration of effective charge carriers in the space-charge layers and associated lower potential barrier height.

As an alternative to yttria-stabilised zirconia (YSZ), mechanical and thermal properties of $SrZrO_3$ as a thermal coating material were reported by Ma et al. [38]. The Young's modulus, hardness and fracture toughness of $SrZrO_3$ was calculated to be 170±4 GPa, 9.2±0.1 GPa and 1.5±0.1 MPa$\sqrt{m}$, respectively. The formation of $La_2Zr_2O_7$ or $SrZrO_3$ was also studied by Yang et al. [39], which negatively impacts cell performance. The layer was formed between the interface of YSZ thin film and $La_{0.8}Sr_{0.2}MnO_3$ and $La_{0.65}Sr_{0.35}MnO_3$ substrate, respectively. These observations were made using XRD, transmission electron microscopy (TEM) and selected area electron diffraction (SAED). The formation of such a layer leads to higher cell resistance and considerable cell voltage loss, because of which the cell degrades faster [40].

Hassan et al. [41] prepared and investigated compounds of a high-temperature SOFC to check their mechanical and thermal properties. Ba and Ca niobate were used as electrolyte materials, whereas $SrCeO_3$ and $SrZrO_3$ stabilised with 5% Yb were used as cathode materials. Cermet of 50:50 wt% Ba, Ca niobate, and Ni was used as an anode material. Vickers hardness and fracture toughness of the cathode materials ($SrZrO_3$ stabilised with 5% Yb) was found to be 4.6 GPa and 1.54 MPa$\sqrt{m}$, respectively. Also, the CTE of $SrZrO_3$ stabilised with 5% Yb was reported to be 10.4×10^{-6} K^{-1}. All the examined samples were potential candidates for use as cathode materials in SOFCs.

2.3. $SrMnO_3$ materials

Negas and Roth initially studied the system $SrMnO_3$ by geometric and quenching experiments, while the structures were determined by Kuroda et al. [42, 43]. It was observed

that the system undergoes about three-phase transitions, namely hexagonal $SrMnO_{3-y}$ (<1035°C), orthorhombic $SrMnO_{2.56}$ (1035-1400°C) and cubic $SrMnO_{2.74-2.62}$ (1400-1740°C). Using dilatometry measurements, Kriegel et al. [44] studied the phase transition temperatures and oxidation temperatures of $SrMnO_{3-y}$ and Sr_2MnO_{4-y}. It was seen that the $SrMnO_3$ structure was built by the most dense-packed anions and Sr^{2+} ions.

Aliovalent dopings in ceramics are done due to their ability to create defects that affect their electrochemical properties. Substitution of $SrMnO_3$ with different elements such as La^{3+}, Pr^{3+}, Mo^{5+} has been well reported in the literature [45]. However, cerium doping is done extensively since partial substitution of Ce^{3+} in place of Sr^{2+} stabilises the perovskite-type structure. It yields a change in the valence state of Mn from +4 to +3, which increases the concentration of charge carriers, thereby increasing the conductivity of $SrMnO_3$.

The structural, thermal and electrical properties of $Sr_{1-x}Ce_xMnO_3$ ($0 \leq x \leq 0.5$) were studied by Hashimoto et al. using XRD, DTA and dc four-probe method, respectively [45]. The composition with the highest cerium content stabilised its crystal structure (tetragonal) even after heat treatment of 100 hrs. The phase showed a high conductivity value of 290 Scm^{-1} at 1000°C, which was due to the compound's highly symmetric structure and the high concentration of charge carriers. The same group also studied the structure, thermal expansion, conductivity and compatibility with the electrolyte of $Sr_{1-x}Ce_xMnO_{3-\alpha}$ (x=0.1, 0.3) [46, 47]. It was observed that at 55°C, there exists a first-order transition from tetragonal to cubic structure, and at the same point, a drastic change in the conductivity was also observed. The conductivity reached a maximum of 450 Scm^{-1} at 150°C and decreased to 270 Scm^{-1} at 800°C. The polarization resistance of $Sr_{1-x}Ce_xMnO_3$ (x=0.1, 0.2, 0.3) was studied by Ryu et al. [48]. The increasing concentration of Ce leads to an increase in the Mn^{3+}. It further leads to the lattice volume expansion due to the larger ionic radii of the Mn^{3+} ion. It was also observed that a decrease in the oxygen vacancy concentration leads to an increase in the

polarisation resistance with the increasing Ce content. The synthesis method and the conductivity were in accordance with the results given by Jeong et al., who had studied the same composition with x=0.4. In this case, x=0.4 showed a single-phase and the secondary phase of CeO_2 [49].

Impedance spectroscopy studies of $SrMnO_3$, $BaMnO_3$ and $Ba_{0.5}Sr_{0.5}MnO_3$ were conducted by Markiewicz et al. [50]. Impedance spectroscopy results gave information about the grain inhomogeneity and also distinguished between long-range and localised conduction mechanisms. The contribution of the grain boundaries is prominent in $BaMnO_3$, whereas it is least in $SrMnO_3$. The conductivity values of $Ba_{0.5}Sr_{0.5}MnO_3$ were found to lie between $BaMnO_3$ and $SrMnO_3$. Burmistrov et al. [51] investigated $Sr_{0.75}Y_{0.25}Co_{0.5}Mn_{0.5}O_{3-y}$ oxides for their electrical conductivity, CTE and reactivity with gadolinia-doped ceria (GDC) electrolyte. The composition had conductivity 59-110 Scm^{-1} between 600°C and 900°C. However, the degradation of the electrochemical characteristics of the cell by 7.5% after 200 hrs at 900°C was observed.

The reason for such degradation was cited to be the mechanical degradation of the cathode-electrolyte interface, which was caused by the local chemical expansion. However, it was concluded that the $Sr_{0.75}Y_{0.25}Co_{0.5}Mn_{0.5}O_{3-y}$ oxides work best as cathodes at 700°C. Sr based double perovskite materials have also been of great interest lately. Double perovskite $LaSrMnCoO_{5+\delta}$ was studied by Zhou et al. as a promising cathode material [52]. The chemical compatibility of the sample was tested with $Sm_{0.2}Ce_{0.8}O_{1.9}$ (SDC) electrolyte. The electrical conductivity of the samples was calculated. It was in the range of 111-140 Scm^{-1} between the temperature range 600-850°C, whereas the average CTE of the sample was 15.8×10^{-6} K^{-1} measured in the temperature range 30-1000°C. Saad et al. [53] studied the structural, electronic and magnetic properties of $SrMnO_3$ and $SrCoO_3$. The XRD and density functional theory (DFT) results showed that $SrMnO_3$ crystallised with a single phase. With

the increase in the occupation number of Mn^{4+} and Co^{4+}, a decrease in the unit cell volume was observed, along with an increase in the tolerance factor of $SrMnO_3$. Abbas et al. [54] studied the thermally activated variations in conductivity and activation energy of $SrMnO_3$. Electrical and impedance spectroscopy techniques were used to calculate the variation in losses, ac conductivity, and activation energy. The temperature dependence of these properties showed that $SrMnO_3$ is thermally activated. The values of dc conductivity and relaxation behaviour were calculated to be 0.036 and 0.034 eV, respectively. A summary of the CTE and conductivity of Sr-based materials is given in Table 2.1.

Table 2.1 The coefficient of thermal expansion (CTE), electronic (σ_e) and ionic conductivities (σ_i) of probable SOFC cathode materials

Composition	Dopant	CTE ($\times 10^{-6}$ K^{-1})	σ_e (Scm^{-1})	σ_i (Scm^{-1})	References
$SrFe_{1-x}Ti_xO_3$	Ti^{4+}	22-26	41-72	-	[16]
$SrTi_{1-x}Fe_xO_{3-\delta}$	Fe^{4+}	11-13	-	-	[18]
$SrFe_{0.7}Cu_{0.3}O_{3-\delta}$	Cu^{2+}	13.8	25-54	-	[20]
$SrFe_{1-x}Nb_xO_3$	Nb^{3+}	21	34-70	-	[23]
$SrZr_{1-x}Fe_xO_3$	Fe^{4+}	-	-	10^{-9} to 10^{-8}	[30]
$SrZrO_3$	Yb^{2+}	10.4	-	-	[41]
$Sr_{1-x}Ce_xMnO_3$	Ce^{3+}	-	270-450	-	[46, 47]
$La_{1-x}Sr_xMnO_3$	Sr^{2+}	11-13	130-300	5.93×10^{-7}	[55]
$La_{1-x}Sr_xCoO_3$	Sr^{2+}	19-20	1200-1600	0.22	[56, 57]
$La_{1-x}Sr_xFeO_3$	Sr^{2+}	12-16	129-369	$0.2\text{-}5.6\times10^{-3}$	[58, 59]
$Sr_{0.8}Ce_{0.2}Mn_{1-x}Co_xO_3$	Co^{2+}	-	102	-	[61]

2.4. Interaction study of SOFC components

During the operation of a SOFC, due to the high temperature and long hours of high-temperature operation of SOFC, there is a risk of the formation of detrimental phases among the different SOFC components. An interfacial study among the different components has been carried out to understand the formation of such phases and predict various materials' lifetime and suitability for SOFC applications. The interaction study between the cathode and the glass sealant and interconnect is not reported much in the literature. However, glass

sealant and interconnect are essential planar SOFC components. Therefore, the formation of any unwanted interfacial layers or chemical deposition and formation of different crystalline phases could hamper the SOFC performance.

Simner et al. [62] observed that an interaction between the Sr-doped $LaFeO_3$ (LSF) cathode and yttria-stabilised zirconia (YSZ) electrolyte exhibited the need for an Sm-doped CeO_2 layer between them. The XRD does not reveal any detrimental phases; however, the diffusion of zirconia decreased the conductivity. Therefore, incorporating an Sm-doped CeO_2 layer between the cathode and YSZ electrolyte is required for enhanced conductivity at the cathode-electrolyte interface. Naoumidis et al. [63] investigated the chemical interaction at the cathode/electrolyte and anode/electrolyte interface of SOFC. Strong diffusion of Mn and Co into the electrolyte took place between the cathode $La_{0.75}Sr_{0.2}Mn_{0.8}Co_{0.2}O_3$ and the $La_{0.9}Sr_{0.1}Ga_{0.8}Mg_{0.2}O_3$ (LSGM) electrolyte. After heat-treatment of 100 hrs at 1300°C, Co diffused deep into the electrolyte, and its concentration increased with the increase in the Co concentration. At the CeO_2 anode and LSGM electrolyte interface, the formation of $LaSrGa_3O_7$ was observed due to La migration into ceria. Compared to the benefit of Co doping on the electrochemical properties, La migration has a negative impact due to its low conductivity. Duong et al. [64] studied the compatibility of an electronic conductor, $Sm_{0.5}Sr_{0.5}CoO_{3-\delta}$ (SSC) and an ionic conductor, LSGM, as constituents of composite SOFC cathodes. Above 800°C, a secondary phase of $LaSrGa_3O_7$ was formed at the interface, which increased with increasing sintering temperature. The extent of inter-diffusion varied depending on the size of the neighbouring grain. SSC and LSGM were incompatible compositing couples at the SOFC intended environments.

Lahl et al. [65] investigated the chemical interactions between alumina-silicate glass sealants and anode side components of the SOFCs. Cordierite forms many reaction mixtures of sealants with ZrO_2 stabilised with YSZ (electrolyte) or nickel (anode). The formation of

detrimental phases such as cordierite and cristobalite were observed in different powder mixtures and diffusion couples. The inter-diffusion investigations revealed maximum diffusion of chromium across the interfaces of the sealant and interconnect. Chromium is estimated to have diffused up to 0.9 mm in 50,000 hrs on operating the SOFC at 1000°C. Kaur et al. [66] investigated the crystallisation mechanism of barium-lanthanum-borosilicate glass ($30BaO\text{-}40SiO_2\text{-}20B_2O_3\text{-}10La_2O_3$) with YSZ and titania-doped bismuth vanadate $Bi_2V_{0.80}Ti_{0.20}O_{5.5\text{-}\delta}$ electrolytes for different heat duration for 5, 100 and 750 hrs. The XRD and microstructural analysis revealed the presence of the $BaSiO_3$ phase. However, no other detrimental phases such as zirconate were formed.

Kumar et al. [67] studied the chemical interaction between $SiO_2\text{-}B_2O_3\text{-}SrO\text{-}A_2O_3$ (A=Y, La, Al) based glasses and $Bi_4V_{1.8}Al_{0.2}O_{11}$ electrolyte at 800°C for different heat treatment durations. $SrVSi_2O_7$, AVO_4 and A_2SiO_5 (A=Y, La, Al) phases were formed during the heat treatment. Strong diffusion of V^{5+} and Bi^{3+} into glasses was observed without any formation of detrimental cristobalite phase. The glass composition, $SiO_2\text{-}B_2O_3\text{-}SrO\text{-}Al_2O_3$, was found compatible with doped bismuth vanadate at SOFC operating temperature. Another glass composition, $AO\text{-}SiO_2\text{-}B_2O_3\text{-}Y_2O_3$ (A=Ba, Sr), was studied for interaction with 8 mol% yttria-stabilised zirconia (YSZ) electrolyte and Crofer 22 APU interconnect by Kumar et al. [68]. The interaction study was performed at 850°C for 100, 200 and 500 hrs. The microstructure of the diffusion couple with the electrolyte did not reveal any porosity, while that of interconnect exhibited the formation of a chromate layer at the interface. The glass samples show good adhesion with the electrolyte as well as the sealant. Crystallisation kinetics is faster for the SrY/YSZ couple due to the low-activation energy of SrY glass and its high number of nucleation sites compared with BaY glass [38].

Perez et al. [69] studied the degradation between three interconnects: Crofer 22 APU, SS430 and Conicro 4023 W 188 and $La_{0.6}Sr_{0.4}FeO_3$ (LSF40) cathode. Chromium deposition was

observed along with the formation of $SrCrO_4$, $LaCrO_3$ and La_2O_3, which block the LSF40 electrode surface, thereby degrading the YSZ/SDC/LSF40/Interconnect stack performance. LSF40 assembled with SS430 exhibited substantial Cr deposition. The deposition of the Cr species and the reaction with the LSF40 cathode is related to the composition of the oxide formed at each metallic interconnect and the composition of the alloys. The best results obtained were for the half-cell (YSZ/SDC/LSF40) in contact with Conicro 4023 W 188 and Crofer 22 APU after heat treatment in air at 800°C for 100 hrs.

2.5. The motivation of the present study

As observed from the literature survey, the B-site elements and doping of the ABO_3 perovskites play an essential role in enhancing these systems' catalytic and conducting properties. As an example, cobalt doping at the B-site increases the electronic conductivity; however, it also greatly influences the CTE of the composition. The increase in the CTE could be avoided by doping with cations having multiple valence states such as nickel, copper etc., which would also improve the overall conductivity of the system. As observed from the literature, $SrZrO_3$ and $SrMnO_3$ have been doped with different dopants to satisfy the structural, thermal and conducting properties according to SOFC requirements.

The proposed systems $SrZrO_3$ and $SrMnO_3$ have been studied extensively with iron and cerium dopants, respectively. However, the extended use of copper and nickel as dopants has not been studied systematically so far. The doping of copper and nickel at the B-site is expected to give interesting results due to their different oxidation states, particularly copper. Moreover, these systems' mechanical properties have not been reported yet, whereas mechanical properties are essential in making cathode supported planar solid oxide fuel cells. Also, the interaction study of the cathode with glass sealant is rarely reported. However, the interaction between the different components of SOFC is of utmost importance to identify the

undesired phase formations at the interfaces, which are detrimental for the working of the SOFC.

2.6. Objectives

The following are the objectives of the present thesis:

1. Synthesis of $SrZr_{1-x}A_xO_3$ and $SrMn_{1-x}A_xO_3$ (A=Ni, Cu) with x=0, 0.05, 0.10, 0.15, 0.20 using solid state reaction method
2. Characterisation of the above mentioned samples using different techniques such as X-ray diffraction (XRD), scanning electron microscope (SEM) with attached energy dispersive spectroscopy (EDS), impedance analyser, dilatometer, Vickers hardness etc. to check their suitability as cathode materials in SOFCs
3. Selected samples will be studied for interaction study with glass sealants and interconnect materials

References

[1] U. Stimming, S.C. Singhal, H. Tagawa, W. Lehnert, Electrochem. Soc. Proc. Ser. 97-40 Pennington, New Jersey, USA (1997) 37-50.

[2] H. Yokokawa, N. Sakai, T. Kawada, M. Dokiya, Solid State Ion. 40 (1990) 398-401.

[3] T. Ishihara, T. Kudo, H. Matsuda, Y. Takita, J. Am. Ceram. Soc. 77 (1994) 1682-1684.

[4] Y. Sakaki, Y. Takeda, A. Kato, N. Imanishi, O. Yamamoto, M. Hattori, M. Iio, Y. Esaki, Solid State Ion. 118 (1999) 187-194.

[5] L.W. Tai, M.M. Nasrallah, H.U. Anderson, D.M. Sparlin, S.R. Sehlin, Solid State Ion. 76 (1995) 259-271.

[6] A. Weber, E. Tiffee, J. Power Sources 127 (2004) 273-283.

[7] F. Riza, Ch. Ftikos, F. Tietz, W.J. Fischer, J. Eur. Ceram. Soc. 21 (2001) 1769-1773.

[8] K. Yasumoto, Y. Inagaki, M. Shiono, M. Dokiya, Solid State Ion. 148 (2002) 545-549.

[9] O. Yamamoto, Electrochim. Acta 45 (2000) 2423-2435.

[10] M. Mogensen, T. Lindegaard, U.R. Hansen, J. Electrochem. Soc. 141(8) (1994) 2122-2128.

[11] T. Ishihara, H. Matsuda, Y. Takita, J. Am. Chem. Soc. 116 (1994) 3801-3803.

[12] J.H. Kim, A. Manthiram, J. Electrochem. Soc. 155(4) (2008) B385-B390.

[13] J.M. Ralph, C. Rossignol, R. Kumar, J. Electrochem. Soc. 150(11) (2003) A1518-A1522.

[14] G. Coffey, J. Hardy, O. Marina, L. Pederson, P. Rieke, E. Thomsen, Solid State Ion. 175 (2004) 73-78.

[15] M.S. Javed, N. Shaheen, A. Idrees, C. Hu, R. Raza, Int. J. Hydrog. Energy 42 (2017) 10416-10422.

[16] X. Yu, W. Long, F. Jin, T. He, Electrochim. Acta 123 (2014) 426-434.

[17] E.V. Tsipis, M.V. Patrakeev, V.V. Kharton, A.A. Yaremchenko, G.C. Mather, A.L. Shaula, I.A. Leonidov, V.L. Kozhevnikov, J.R. Frade, Solid State Sci. 7 (2005) 355-365.

[18] V.V. Kharton, A.V. Kovalevsky, A.P. Viskup, J.R. Jurado, F.M. Figueiredo, E.N. Naumovich, J.R. Frade, J. Solid State Chem. 156 (2001) 437-444.

[19] J.H. Park, K.Y. Kim, S.D. Park, Desalination 245 (2009) 559-569.

[20] Q. Li, T. Xia, L. Sun, H. Zhao, L. Huo, Electrochim. Acta 150 (2014) 151-156.

[21] X. Ding, X. Gao, J. Shen, J. Wang, W. Zhu, X. Wang, J. Jiang, Int. J. Hydrog. Energy 39 (2014) 1030-1038.

[22] K.T. Lee, A. Manthiram, J. Electrochem. Soc. 153(4) (2006) A794-A798.

[23] A. Ahtee, M. Ahtee, A.M. Glazer, A.W. Hewat, Acta Crystallog. B 32 (1976) 3243-3246.

[24] L. Carlsson, Acta Crystallog. 23 (1976) 901-905.

[25] D. Ligny, P. Richet, Phys. Rev. B 53(6) (1996) 3013-3022.

[26] B.J. Kennedy, C.J. Howard, B.C. Chakoumakos, Phys. Rev. B 59 (1999) 4023-4027.

[27] H. Fujimori, M. Kakihana, K. Ioku, S. Goto, M. Yoshimura, J. Ceram. Soc. Japan 112(4) (2004) 189-192.

[28] S. Hasegawa, T. Sugimoto, T. Hashimoto, Solid State Ion. 181 (2010) 1091-1097.

[29] Y. Zhao, D.J. Weidner, Phys. Chem. Miner. 18 (1991) 294-301.

[30] S. Misra, Mater. Chem. Phys. 190 (2017) 1-7.

[31] C. Tang, Q. Wu, Y. Cui, Ceram-Silikaty 60(1) (2016) 68-71.

[32] H. Borkar, A. Barvat, P. Pal, A.K. Shukla, J.J. Pulikkotil, A. Kumar, J. Appl. Phys. 119 (2016) 214101(1)-(6).

[33] N.F. Muhamad, R.A.M. Osman, M.S. Idris, M.N.M. Yasin, EPJ Web Conf. 162 (2017) 01052(1)-(4).

[34] J. Muller, K.D. Kreuer, J. Maier, S. Matsuo, M. Ishigame, Solid State Ion. 97 (1997) 421-427.

[35] T. Osaka, C. Numako, K. Koto, Mater. Res. Bull. 34(1) (1999) 11-24.

[36] C. Shi, M. Morinaga, J. Comput. Chem. 27 (2006) 711-718.

[37] G. Juaristi, D. Coll, G.C. Mather, J. Power Sources 331 (2016) 435-444.

[38] W. Ma, D.E. Mack, R. Vaben, D. Stover, J. Am. Ceram. Soc. 98(8) (2008) 2630-2635.

[39] K. Yang, J.H. Shen, K.Y. Yang, I.M. Hung, K.Z. Fung, M.C. Wang, J. Power Sources 159 (2006) 63-67.

[40] S. Kanae, Y. Toyofuku, T. Kawabata, Y. Inoue, T. Daio, J. Matsuda, J.T. Chou, Y. Shiratori, S. Taniguchi, K. Sasaki, ECS Trans. 68(1) (2015) 2463-2470.

[41] D. Hassan, S. Janes, R. Clasen, J. Eur. Ceram. Soc. 23 (2003) 221-228.

[42] T. Negas, R.S. Roth, J. Solid State Chem. 1 (1970) 409-418.

[43] K. Kuroda, N. Ishizawa, N. Mizutani, M. Kato, J. Solid State Chem. 38 (1981) 297-299.

[44] R. Kriegel, N. PreuB, Thermochem. Acta 285 (1996) 91-98.

[45] A. Maignan, S. Hebert, L. Pi, D. Pelloquin, C. Martin, C. Michel, M. Hervieu, B. Raveau, Cryst. Engg. 5 (2002) 365-382.

[46] S. Hashimoto, H. Iwahara, J. Electroceram. 4(1) (2000) 225-231.

[47] S. Hashimoto, H. Iwahara, Mater. Res. Bull. 35 (2000) 2253-2262.

[48] J. Ryu, R. O' Hayre, H. Lee, Solid State Ion. 260 (2014) 60-64.

[49] C. Jeong, J. Ryu, T. Noh, Y.N. Kim, H. Lee, Adv. Appl. Ceram. 112(8) (2013) 494-498.

[50] E. Markiewicz, R.B. Koronska, A. Budziak, A. Kalvane, D.M. Nalecz, Phase Transit. 87 (2014) 1060-1072.

[51] I. Burmistrov, O.A. Drozhzhin, S.Y. Istomin, V.V. Sinitsyn, E.V. Antipov, S.I. Bredikhin, J. Electrochem. Soc. 156(10) (2009) B1212-B1217.

[52] Q. Zhou, W.C.J. Wei, Y. Guo, D. J. Electrochem. Commun. 19 (2012) 36-38.

[53] M.M. Saad H.E., A. El-Taher, Dig. J. Nanomater. Bios. 11(4) (2016) 1383-1396.

[54] S.K. Abbas, S. Atiq, S. Riaz, S. Naseem, J. Mater. Sci. Mater. Electron. 28 (2017) 7171-7176.

[55] S.P. Jiang, Solid State Ion. 146 (2002) 1-22.

[56] F. Tietz, I.A. Raj, M. Zahid, D. Stover, Solid State Ion. 177 (2006) 1753-1756.

[57] F. Tietz, I.A. Raj, M. Zahid, A. Mai, D. Stover, Prog. Solid State Chem. 35 (2007) 539-543.

[58] E.V. Bongio, H. Black, F.C. Raszewski, D. Edwards, C.J. McConville, V.R.W. Amarakoon, J. Electroceram. 14 (2005) 193-198.

[59] M.V. Patrakeev, J.A. Bahteeva, E.B. Mitberg, I.A. Leonidov, V.L. Kozhevnikov, K.R. Poeppelmeier, J. Solid State Chem. 172 (2003) 219-231.

[60] H. Ullmann, N. Trofimenko, F. Tietz, D. Stover, A.A. Khanlou, Solid State Ion. 138 (2000) 79-90.

[61] H. Gu, H. Chen, L. Gao, Y. Zheng, X. Zhu, L. Guo, Int. J. Hydrog. Energy 33 (2008) 4681-4688.

[62] S.P. Simner, J.P. Shelton, M.D. Anderson, J.W. Stevenson, Solid State Ion. 161 (2003) 11-18.

[63] A. Naoumidis, A.A. Khanlou, Z. Samardzija, D. Kolar, Fresenius J. Anal. Chem. 365 (1999) 277-281.

[64] A.T. Duong, D.R. Mumm, J. Power Sources 241 (2013) 281-287.

[65] N. Lahl, D. Bahadur, K. Singh, L. Singheiser, K. Hilpertz, J. Electrochem. Soc. 149(5) (2002) A607-A614.

[66] G. Kaur, O.P. Pandey, K. Singh, Int. J. Appl. Ceram. Tech. 11(1) (2014) 136-145.

[67] V. Kumar, S. Sharma, O.P. Pandey, K. Singh, Solid State Ion. 181 (2010) 79-85.

[68] V. Kumar, O.P. Pandey, K. Singh, K. Lu, Fuel Cells 14(4) (2014) 635-644.

[69] V.M. Perez, A.M. Amesti, M.I. Arriortua, J. Power Sources 280 (2015) 505-515.

Overview

This chapter gives comprehensive information about the synthesis procedure and the technical details of the different characterisation techniques. All the samples have been synthesised using the solid-state reaction method. In some cases, two stages of heat-treatment are given to achieve the desired phases with good density. The heat-treated samples have been studied for their structural, thermal, and electrical properties. Characterisation techniques such as X-ray diffraction (XRD), Rietveld refinement, Fourier-transform infrared spectroscopy (FTIR), scanning electron microscopy (SEM) coupled with energy dispersive spectroscopy (EDS), X-ray photoelectron spectroscopy (XPS), dilatometry, thermogravimetric-differential thermal analysis (TG-DTA), impedance analyser, ultraviolet-visible spectroscopy (UV-Vis), photoluminescence spectroscopy (PL) and Vickers hardness are used to study these properties.

3.1. Raw materials

Stoichiometric ratios of $SrCO_3$ (98%, Loba Chemie), ZrO_2 (99%, Loba Chemie), MnO_2 (80% LR, SD Fine), CuO (99%, Loba Chemie), and NiO (99%, Loba Chemie) were used for the synthesis of the compositions $SrM_{1-x}A_xO_{3-\delta}$ (M=Zr, Mn; A=Cu, Ni; $0.00 \leq x \leq 0.20$), respectively. The chemicals were used as such without any further purification. Fig. 3.1 gives the step-by-step representation of the synthesis procedure. The details of these steps are discussed in the following section.

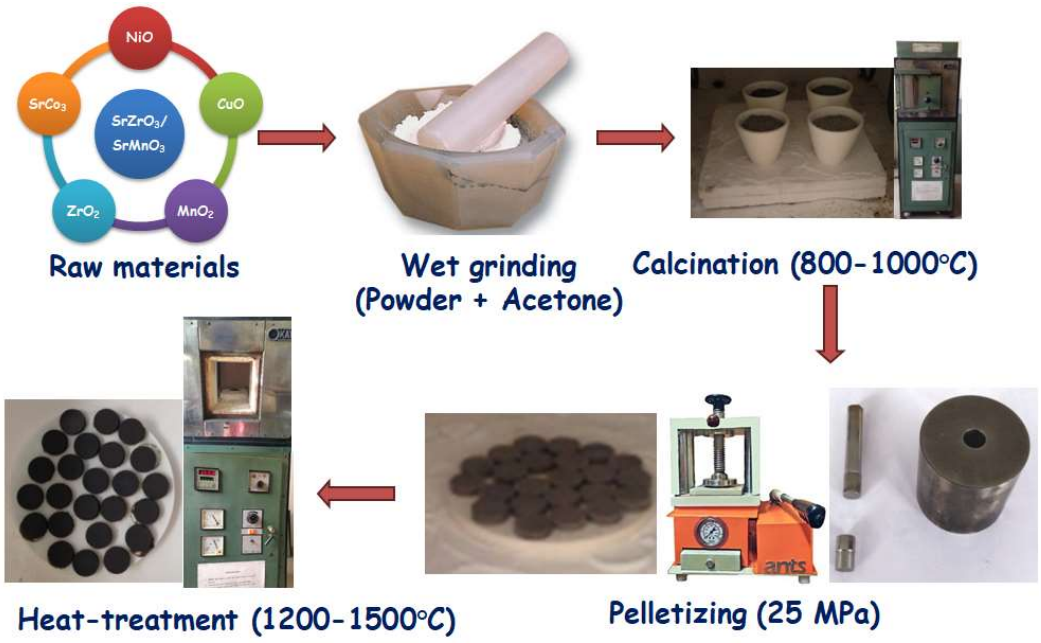


Fig. 3.1 Schematic of the synthesis procedure of $SrM_{1-x}A_xO_{3-\delta}$ (M=Zr, Mn; A=Cu, Ni; $0.00 \leq x \leq 0.20$)

3.2. Sample synthesis procedure

According to the chemical formula, the powders of all the materials mentioned in section 3.1 were taken in stoichiometric ratios. These chemical powders were mixed manually using an agate mortar and pestle for 2 hours (hrs) in acetone media. After mixing, they were subjected to calcination to convert the carbonates into oxides. Polyvinyl alcohol (PVA) was also mixed in the calcined powders for better binding of the powders. The binder mixed powders were

pelletised in a steel die set with a tungsten carbide inner lining using a manually operated hydraulic press. Pellets of a thickness of ~1-2 mm and ~10 mm diameter were made by applying a load of 25MPa. The pellets were placed on alumina disks and sintered at a heating rate of 5°C min^{-1} in a high resistance OKAY furnace by Bysakh and Co. Kolkata, India. Owing to the different melting points of the dopants (NiO and CuO), the heat-treatment temperatures vary for each composition, as listed in Table 3.1. Moreover, the calcination temperature and sintering temperature were decided based on the thermal studies of some of the samples after taking stoichiometric ratios and grinding.

Table 3.1 The calcination and sintering temperatures and the respective time durations of the compositions used in this study. Here x=0.05, 0.10, 0.15, 0.20 for all the compositions

Composition	Sample label	Calcination temperature (Time)	Sintering temperature (Time)
$SrZrO_3$	SZ-0	800°C (10 hrs)	1500°C (5 hrs)
$SrZr_{1-x}Ni_xO_{3-\delta}$	SZN-5, SZN-10, SZN-15, SZN-20	800°C (10 hrs)	1300°C (15 hrs) 1000°C (24 hrs)
$SrZr_{1-x}Cu_xO_{3-\delta}$	SZC-5, SZC-10, SZC-15, SZC-20	800°C (10 hrs)	1200°C (5 hrs)
$SrMnO_3$	SM-0	1000°C (5 hrs)	1300°C (4 hrs)
$SrMn_{1-x}Ni_xO_{3-\delta}$	SMN-5, SMN-10, SMN-15, SMN-20	1000°C (5 hrs)	1300°C (4 hrs)
$SrMn_{1-x}Cu_xO_{3-\delta}$	SMC-5, SMC-10, SMC-15, SMC-20	1000°C (5 hrs)	1250°C (4 hrs)

Based on the characterisation results of $SrM_{1-x}A_xO_{3-\delta}$ (M=Zr, Mn; A=Cu, Ni; $0.00 \leq x \leq 0.20$), the sample (SZC-15) was selected for interaction with glass sealant (an essential component of the planar design of the SOFC as discussed in the introduction section) having composition $45SiO_2+40BaO+10B_2O_3+5ZrO_2$. The glass sealant, $45SiO_2+40BaO+10B_2O_3+5ZrO_2$, referred

to as SBBZ, was synthesised using the melt quench technique. The oxides, $BaCO_3$ (99%, Loba Chemie), B_2O_3 (99%, Ubichem), SiO_2 (~60% granularity, Loba Chemie), ZrO_2 (99%, Loba Chemie) were taken in respective weight% and mixed manually for 2 hrs in an agate pestle and mortar. The mixed powders were placed in a recrystallised alumina crucible and melted at 1500℃. The melt was poured onto the copper plate and quenched by another copper plate. The samples for the interaction study were taken in weight % with 70% SZC-15 and 30% SBBZ. The powders of both the components were mixed, pelletised, and heat-treated at 800℃ in the air for 1, 10, 100, and 500 hrs, respectively. The samples are therefore labelled as IS-1, IS-2, IS-3, and IS-4, respectively. For heat-treatment at 500 hrs, instead of mixing the powders, a diffusion couple was made by layering 70 wt.% SZC-15 over 30 wt.% SBBZ with the help of hydraulic press at a load of 25 MPa as shown in Fig. 3.2.

The sample SZC-15 was studied for interaction with a standard interconnect material, Crofer 22 APU. Crofer 22 APU by ThyssenKruppVDM GmbH is a commonly used ferritic steel interconnect material. In the present study, commercially available Crofer consisting of 20-24% Cr, 0.3-0.8% Mn, 0.5% Si, 0.5% Cu, 0.5% Al, 0.03-0.20% Ti, 0.04-0.20% La, 0.05% P, 0.03% C, 0.02% S, and balance% of Fe (all in wt.%) was used [1]. It was cut into rectangular pieces of ~14 mm×2.5 mm×4 mm dimensions. Further, the pieces were polished using silicon carbide (SiC) emery papers of grit sizes 400 and 1000 to get a mirror-like surface. During polishing, the pieces were wet using diluted micro polish alumina (~6μm size). The pieces were ultrasonically cleaned in acetone after polishing. The diffusion couple, i.e. Crofer 22 APU/SZC-15/Crofer 22 APU, was made using the slurry technique. The diffusion couples were heat-treated at 1000℃ for 1 and 10 hrs and are labelled as ISC-1 and ISC-2, respectively.

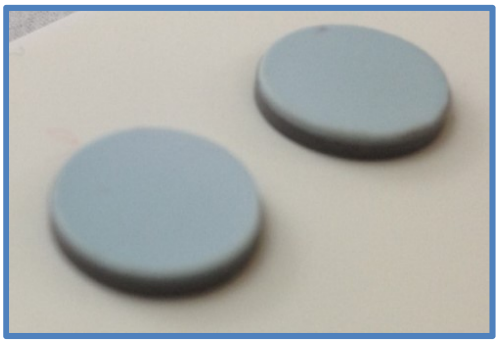


Fig. 3.2 Diffusion couple of SZC-15 and SBBZ. The upper white coloured layer represents the glass SBBZ, and the lower black layer corresponds to SZC-15

3.3. Characterisation techniques

The heat-treated samples were characterised for their structural, thermal, and electrical properties to check their suitability as cathode materials for SOFC. The following sections give a brief description of the technical details of the characterisation techniques such as X-ray diffraction (XRD), Rietveld refinement, Fourier-transform infrared spectroscopy (FTIR), physical parameters, scanning electron microscopy (SEM) with attached energy dispersive spectroscopy (EDS), X-ray photoelectron spectroscopy (XPS), dilatometry, thermogravimetric and differential thermal analysis (TG-DTA), impedance spectroscopy, ultraviolet-visible (UV) spectroscopy, photoluminescence (PL) spectroscopy, and Vickers hardness.

3.3.1. X-ray diffraction (XRD)

Powder XRD is a commonly used non-destructive, qualitative and quantitative analytical technique to detect crystalline phases and their volume fractions. In this technique, X-rays are diffracted from the testing powder samples. The X-rays produced by the cathode ray tube are filtered to produce monochromatic X-ray radiation, directed towards the sample in the form of a collimated beam, as shown in Fig. 3.3 (a). On interacting with the sample, the X-rays produce constructive interference (and a diffracted ray) on satisfying the following equation, i.e., Braggs law:

$$n\lambda = 2\,d\sin\theta \tag{3.1}$$

where λ is the wavelength of the X-ray (generally used is Cu K_α = 1.5406 Å), θ is the scattering angle, and n is an integer representing the order of the diffraction peak [2].

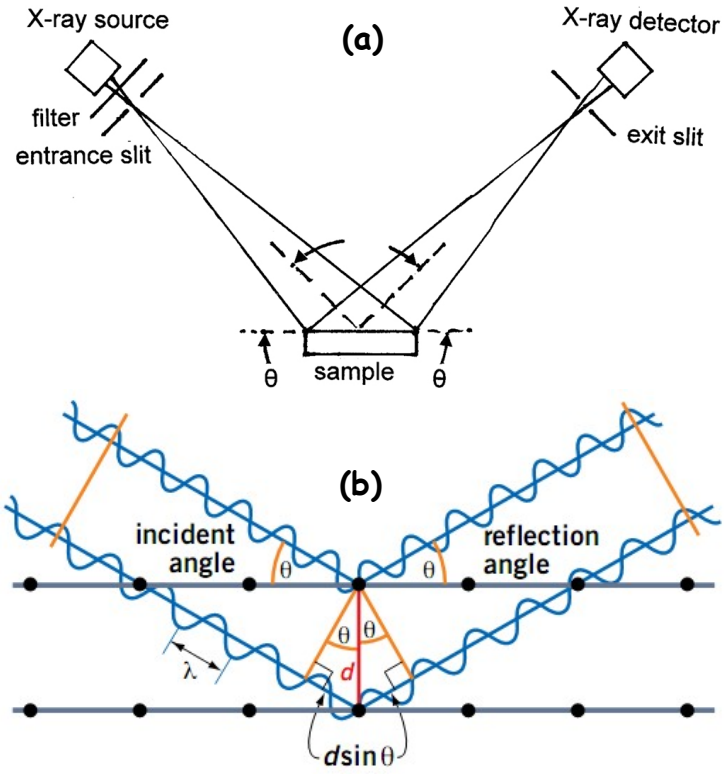


Fig. 3.3 An illustration of the (a) different components that make up an X-ray diffractometer and (b) the basic principle of X-ray diffraction

The samples are scanned over a range of 2θ angles giving diffractions from all the possible lattice directions due to the random orientation of the powder samples. Each diffracted beam corresponds to a unique d-space value used to compare with standard reference data for identifying the crystalline phases (Fig. 3.3 (b)). The international centre for diffraction data (ICDD) database provides the standard reference patterns. PANalytical X'Pert Pro X-ray diffractometer was used to obtain the XRD patterns in the present study. The system is equipped with a Ni filter to filter out wavelengths other than Cu-K_α radiations. The patterns were recorded between the angular range of 10-80° with a step size of 0.017°. During the measurement, the scan speed was 4° min^{-1}. X'Pert HighScorePlus software was used for peak

analysis. Various other parameters such as the average crystallite size, lattice parameters, volume fraction of the different phases, etc., are calculated using the XRD patterns. The Scherrer equation given below correlates the peak broadening (B) given by the full width at half maxima (FWHM) in radians with the average crystallite size (D):

$$D = \frac{k\lambda}{B(2\theta)cos\theta} \tag{3.2}$$

Here λ is the incident wavelength (Cu K_α) and k is the shape factor constant varying between 0.8-1.2 (generally taken as 0.9) [2]. The volume fraction of the different crystalline phases present in the heat-treated samples is calculated using the direct comparison method as given by Cullity [2].

3.3.2. Rietveld refinement

The X-ray diffraction of the powder samples results in a pattern characterised by reflections, i.e., peaks in intensity at certain positions. The peak height, width, and position help determine various aspects of the crystal structure. The Rietveld refinement method uses the least-squares approach to refine a theoretical line profile to match the measured profile. A well-fitted profile is achieved by optimising lattice parameters, background functions, atomic positions, atomic site occupancies, preferred orientation, overall scale factor, asymmetry values, etc. The FWHM has a vital role in the refinement of the XRD patterns. Since the FWHM is a function of 2θ, therefore, the variation of FWHM with the θ is given by the following equation [3]:

$$(B(2\theta))^2 = U\ tan^2\theta + V\ tan\theta + W \tag{3.3}$$

where U, V and W are the peak shape parameters that are varied during the refinement. A few statistical parameters known as the reliability factors or R-indices define the accuracy of the fitting. The following equations express the R-indices such as profile factor (R_p), weighted profile factor (R_{wp}) and expected weighted profile factor (R_{exp}) [4]:

$$R_p = \sum |y_{i(obs)} - y_{i(cal)}| / \sum y_{i(obs)} \quad (3.4)$$

$$R_{wp} = [\sum w_i \left(y_{i(obs)} - y_{i(cal)}\right)^2 / \sum w_i \, y_{i(obs)}^2]^{1/2} \quad (3.5)$$

$$R_{exp} = [(N - P) / \sum w_i y_{i(obs)}^2]^{1/2} \quad (3.6)$$

where N is the total number of observed data points, P is the number of refined parameters and $(N - P)$ is the number of degrees of freedom. Apart from the R-indices, the goodness of fit (χ^2) is the ratio of R_{wp} and R_{exp}. As R_{wp} approaches to R_{exp}, χ^2 tends to 1, thus implying a well-refined XRD pattern. Fig. 3.4 shows the difference in the plot of the calculated and observed diffraction patterns. It is another method of checking the accuracy of the refinement. In the present study, FullProf software was used to refine the cell parameters at room temperature. The XRD patterns were fitted using the pseudo-Voigt peak shape function, a convolution of Gaussian and Lorentzian functions. A representative Rietveld plot of SZC-10 is given in Fig. 3.4.

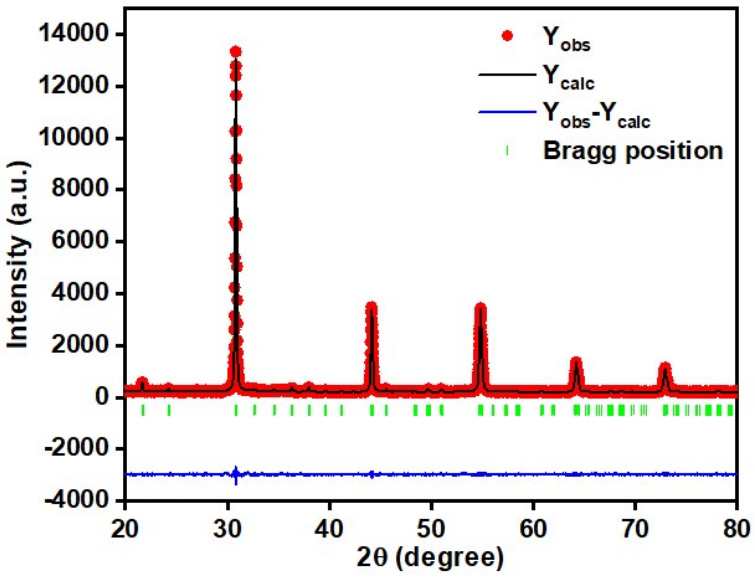


Fig. 3.4 Representative Rietveld plot of SZC-10. The red dotted line represents the observed data, and the black line represents the calculated data. A complete overlap of the two results in a straight blue line exhibiting complete refinement

3.3.3. Fourier-transform infrared spectroscopy (FTIR)

FTIR is used to obtain the infrared spectrum of absorption and emission of solids, liquids, and gases. FTIR makes use of a mathematical process (Fourier transform) to convert the raw data (interferogram) into the actual spectrum (Fig. 3.5). When the infrared radiation passes through the given sample, some of it is absorbed by the sample while some passes through it, i.e., transmitted. The resulting signal obtained at the detector is the spectrum representing a molecular fingerprint of the sample. FTIR is used to collect high spectral resolution data over a wide range of wavelengths between 10,000 and 400 cm^{-1} [5]. FTIR spectroscopy is helpful since each chemical element produces unique spectral fingerprints.

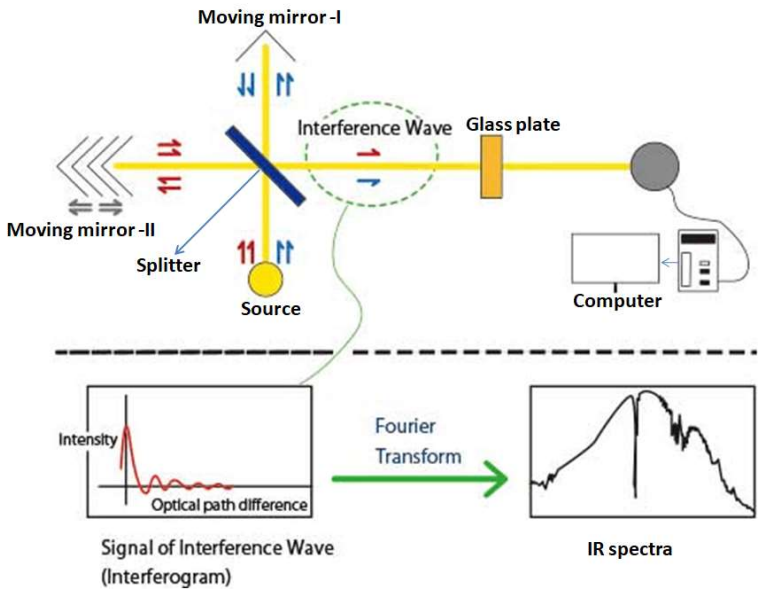


Fig. 3.5 An illustration of the principle of FTIR

The FTIR spectrum exhibits two fundamental vibration modes, i.e., symmetric stretching and bending modes which are active under infrared radiation. Particularly in the perovskite structured materials, the bending and stretching vibrations of the B-site cations and oxygen (B-O) give rise to the formation of bands of varying intensities [6]. Therefore, from the FTIR spectra, bond lengths and bond strength of the molecules can be determined, which could be correlated to the thermal expansion of the materials. In the present study, Spectrum RX-I

from Perkin Elmer was used to study the infrared spectra of the samples at room temperature. The spectra were recorded between 4000 and 400 cm^{-1}. However, for representative purposes, only the spectra between 1800 and 400 cm^{-1} are shown since the bands beyond 1800 cm^{-1} are generally of stretching and bending vibrations of adsorbed water molecules. ~20 mg of potassium bromide (KBr) was added to ~5 mg of the samples to obtain the transmission spectra.

3.3.4. Density and other physical parameters

For a better insight into the microstructural properties of perovskite oxides, it is preferred to know the density of the samples since density plays a vital role in controlling the properties of polycrystalline materials [7]. The density has been calculated based on the concept of Archimedes' principle. In this method, the ratio of the weight of the heat-treated pellet in the air to the weight of the pellet dipped in Xylene is measured. It is done to get a better idea about the structure of the material since the liquid gets absorbed in the pores of the sample, which is not possible in the case where density is calculated simply by the ratio of mass over the volume of the heat-treated pellets. The following formula is used to calculate the density (ρ) of the samples:

$$\rho = \frac{W_a}{W_a - W_x} \times \rho_x \tag{3.7}$$

where ρ_x is the density of Xylene, which is 0.863 gcm^{-3} at room temperature, W_a is the weight of the sample in air and W_x weight of the sample after dipping in Xylene. Xylene is chosen as the buoyant since it does not react and permeates quickly into the tiny pores of the samples due to its low density. Moreover, it evaporates quickly without any need for heat treatment.

With the help of density, various other physical parameters such as molar volume and ionic concentration are calculated, which are instrumental in the conductivity analysis. Molar volume and ionic concentration are calculated using the following formulas [8]:

$$V_m = \frac{m}{\rho} \tag{3.8}$$

$$N = \frac{\rho N_a}{100 \times m} \tag{3.9}$$

where N_a are the Avogadro's number (6.023×10^{23} mol^{-1}), and m is the molecular weight of dopant in the sample. The distance between dopant ions (R) and the polaron radius (r_p) are calculated using the ionic concentration. These parameters are calculated using the following formulas:

$$R = \sqrt[3]{\frac{1}{N}} \tag{3.10}$$

$$r_p = 0.5 \times \sqrt[3]{\frac{\pi}{6N}} \tag{3.11}$$

3.3.5. Scanning electron microscopy (SEM) and energy dispersive spectroscopy (EDS)

SEM is a widely used characterisation technique to study the morphology of ceramic materials. SEM provides information about the size and shape of the grains, porosity, presence of different elements, agglomeration, etc. In SEM, a beam of highly energetic electrons from an electron gun having a heated tungsten cathode is shown in Fig. 3.6 (a). The electron beam is then focused using two condenser lenses and one objective lens. Further, the beam is accelerated by applying a high voltage of 1000-50,000 Volts, which current up to 10^{-8} to 10^{-7} Ampere. A diffusion or a turbomolecular pump maintains the required vacuum. The electron beam then strikes the sample surface, as shown in Fig. 3.6 (b). An electron detector

collects the emitted electrons from the surface. These signals are amplified, and the required images are obtained and processed for further analysis [9].

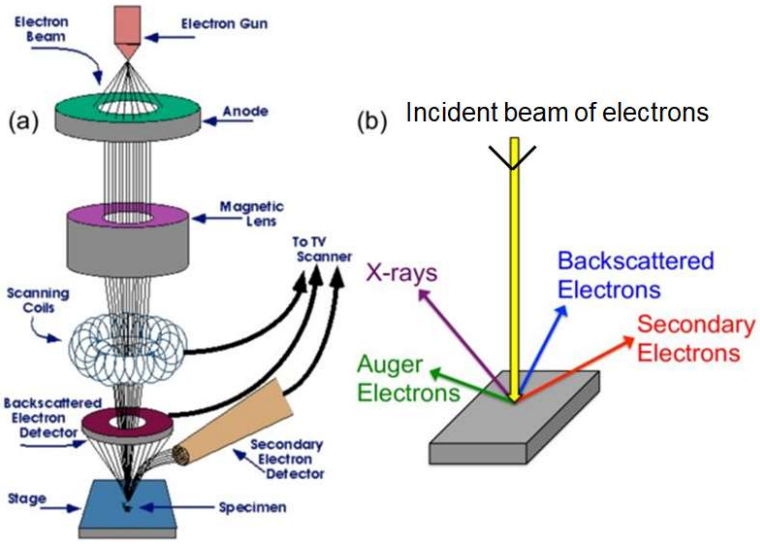


Fig. 3.6 Schematic of (a) SEM and (b) typical emissions emitted out from the sample when an incident beam interacts with a specimen [10]

In the present study, the SEM micrographs of the gold-coated surfaces and the fractured cross-sections of the samples were taken using JEOL, JSM-6510 LV scanning electron microscope. Since the ceramic samples are non-conducting at room temperature, a thin layer of an electrically conducting metal such as platinum or gold has to be sputtered onto the samples to prevent charging of the specimen. Due to charging, the SEM image becomes blurred and low in contrast.

Fig. 3.7 (a) shows the samples mounted over a stub and placed in a JEOL, JEC-1600 Auto fine coater (Fig. 3.7(b)) for sputtering. However, in the case of the diffusion couple, the pellet was cast in an acrylic mould shown in Fig. 3.7(c). For the SEM/EDS analysis, the mould was cut in two halves using a Buehler, IsoMet Low Speed precision cutter. In IS-4, i.e. the diffusion couple of SZC-15 with sealant heat-treated at 500 hrs, the morphology was observed using SU8010, Hitachi field emission scanning electron microscope (FE-SEM). The grain size measurements were done using SEM micrographs through the intercept method. In

this method, lines of known length are drawn over the SEM micrograph, and the numbers of grains cutting the lines are counted. The average grain size corresponds to the ratio of the length of the line to the number of grains intersecting that line.

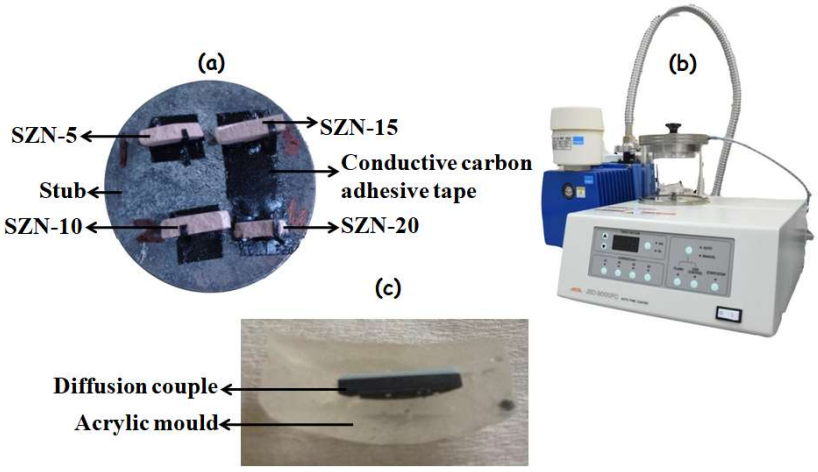


Fig. 3.7 (a) Sintered pellets placed on a stub for coating, (b) auto fine coater by JEOL, under which the samples are placed for coating, and (c) the diffusion couple placed in a mould

The effect of doping on the sample's chemical composition was determined using energy dispersive spectrometry (EDS) with an INCA setup coupled to the SEM setup. EDS uses the X-rays emitted out from the specimen to detect the elemental composition of the given sample. The entire pellet is scanned at first and then using the point analysis, different sections are scanned to find the elemental composition at that particular point. The output is given in the form of peaks corresponding to different elements with respect to energy at the *x*-axis. The intensity of the peaks depends on the percentage of elements present in the given sample. In the diffusion couple (IS-4) case, line and dot mapping were performed to observe the diffusion of elements from cathode to sealant and vice-versa.

3.3.6. X-ray photoelectron spectroscopy (XPS)

EDS gives an estimate of the atomic or weight % of the elements present in the composition. However, it does not give any information about the element's oxidation state present in the

samples. Therefore, XPS is used to get information about the elemental composition, empirical formula, chemical, and electronic state of the elements within the material. Particularly in the compositions involving transition metals, it is essential to know the element's oxidation state. Here, a beam of X-rays irradiates the sample under study, and the kinetic energy of the elements emitted from the top 1-10 nm of the sample surface is measured as shown in Fig. 3.8. The spectrum obtained plots the number of detected electrons per energy interval versus their kinetic energy. Each element has unique binding energy (BE) associated with the core electron levels. The following relation gives the relationship between the kinetic energy of the ejected photoelectron and the binding energy:

$$KE = h\nu - BE \tag{3.12}$$

Here, $h\nu$ refers to the incoming X-ray photon energy. Generally, XPS measurements use Al K_α (1486.6 eV) or Mg K_α (1253.7 eV) radiations. Quantitative data is obtained from the peak heights or peak areas, while the identification of chemical states is made from the exact measurement of peak positions and separations and certain spectral features. In the present case, an XPS spectrometer (PHI-5000 VersaProbe III, Physical Electronics) using Al-Kα radiation with carbon peak as the reference to analyse the oxidation states of Cu, Ni, and Mn in Cu and Ni-doped $SrZrO_3$ and $SrMnO_3$.

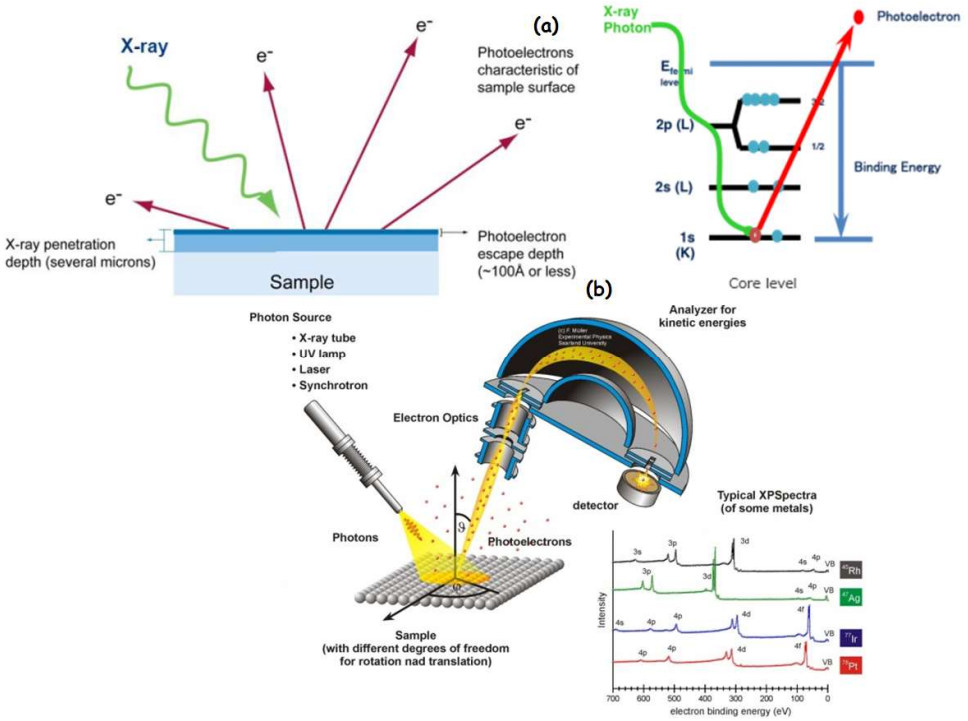


Fig. 3.8 An illustration of the (a) basic principle and (b) instrumentation of XPS

3.3.7. Dilatometry

The coefficient of thermal expansion (CTE) is an important parameter that all the SOFC components should satisfy. During the fabrication and thermal cycling of the SOFC, the CTE of the electrodes, electrolyte, interconnect, and glass sealants should match or fall within the tolerance limit, i.e., 9-13×10^{-6} °C^{-1} with each other. Dilatometry is an efficient technique used for CTE measurement. The thermal expansion is generally a consequence of the nature of interatomic forces. According to the Condon-Morse potential, the interaction energy between a cation and anion is a fine balance between the Coulombic attraction and the internuclear repulsion. The potential well determines how the atoms vibrate since they can neither come too close (to avoid repulsion) nor go too far, or there will be no restoring Coulombic attraction. Because of the asymmetry of the potential well, the average separation distance increases with temperature, resulting in an expansion of the crystal lattice. As the temperature rises, the CTE could be positive, negative, or anisotropic, depending on the nature of the material. However, any discontinuity in the CTE accounts for the phase transitions in the

materials [11, 12]. In the present case, a push-rod type Netzsch DIL 402 PC dilatometer was used to carry out the thermal expansion measurements (Fig. 3.9). The linear CTE of the sintered $SrM_{1-x}A_xO_{3-\delta}$ (M: Zr, Mn; A: Cu, Ni; $0.00 \leq x \leq 0.20$) samples were measured from 200-1000°C, and the CTE of diffusion couples was measured from 200-700°C at a heating rate of 5°C min^{-1} in air.

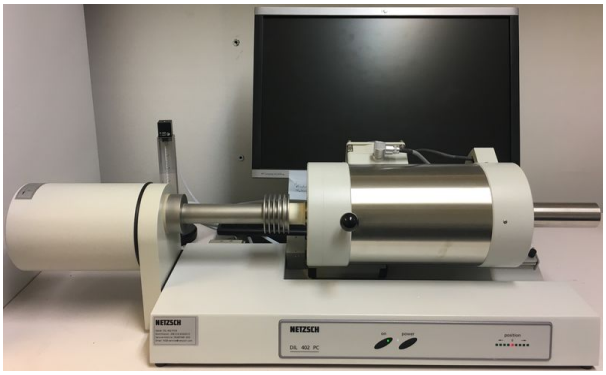


Fig. 3.9 Pictorial representation of a push rod type dilatometer

3.3.8. Thermogravimetric and differential thermal analysis (TG-DTA)

The ceramic samples usually change during the thermal cycle, such as phase transitions, melting, crystallisation, decomposition, etc. TG-DTA is a valuable and simple technique to understand the changes in the material with respect to temperature. From the TG curves, one can infer the changes in the sample composition, thermal stability, and material purity. On the other hand, DTA gives information about the change in the crystal structure with respect to temperature and atmosphere, oxidation, reduction in the form of endothermic and endothermic reactions. Since both processes' instrumentation is similar, TG and DTA are often coupled together in a single instrument. However, there is a difference in the working principle of the two processes. Both the systems are equipped with two aluminium/ alumina/ platinum pans containing the sample and the reference materials. The system is equipped with a built-in furnace, as shown in Fig. 3.10 (a, b). In TG, a balance compares the unknown mass with a standard mass by comparing their weights, whereas, in DTA, the temperature

difference between the sample and reference material is monitored against time or temperature in a specified atmosphere. The device is located in a block heated (or cooled) at a controlled temperature. The electric signal (emf) measured at the ends of the thermocouple is proportional to the temperature difference between the sample and reference pans. In the present study, Perkin Elmer's Diamond Pyris simultaneous TG-DTA setup was used to study the TG-DTA of the samples by placing them in alumina crucibles in the temperature range of RT-1000°C at a heating rate of 10°C min^{-1} in a nitrogen atmosphere to find out any phase transitions and thermal stability of the samples. For some samples, such as $SrZr_{1-x}Ni_xO_{3-\delta}$ ($0.00 \leq x \leq 0.20$), differential scanning calorimetry was conducted using Linseis' HDSC PT 1600 differential scanning calorimeter (DSC) to observe the phase transitions. The parameters for the measurements were the same as that of TG-DTA analysis.

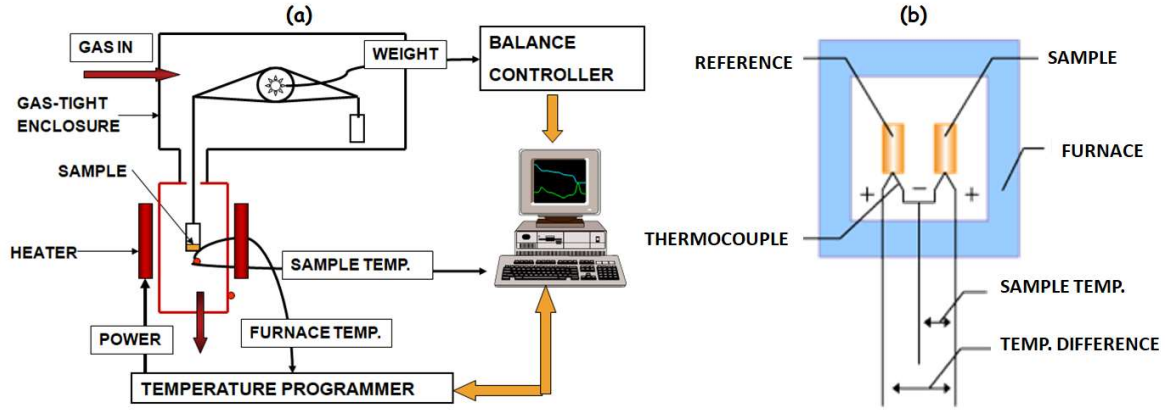


Fig. 3.10 Diagrammatic representation of the instrumentation of (a) TGA and (b) DTA/DSC setup

3.3.9. Impedance spectroscopy

For any electrical device, the higher the conductivity higher is the output. The materials used in the present study are ceramic, i.e., the conduction mechanism in these materials is usually temperature-dependent. At room temperature, these materials are insulators; therefore, doping of transition metals is done to enhance the conduction mechanism. Moreover, the conduction in SOFC is temperature-dependent; therefore, impedance spectroscopy is used to calculate

the conductivity of the samples. Impedance spectroscopy is an easy and reliable method of analysing the nature of electrical conduction, particularly for ionic solids, i.e., ceramics. It is a well-defined technique that correlates the electrical properties with the microstructure of various ceramic materials [13]. Using AC impedance spectroscopy, it is possible to analyse the conductivity of fuel cell materials. Impedance spectroscopy identifies the grains, grain boundaries and electrode effects by correlating the microstructure with equivalent electric circuits (Fig. 3.11). Each component can be considered as a combination of resistive and capacitive elements [14]. The combinations of resistive and capacitive elements are called equivalent circuits that vary with the microstructure change. The resistance and capacitance of an unknown component can be determined from the real and imaginary impedance over a wide range of frequencies [15].

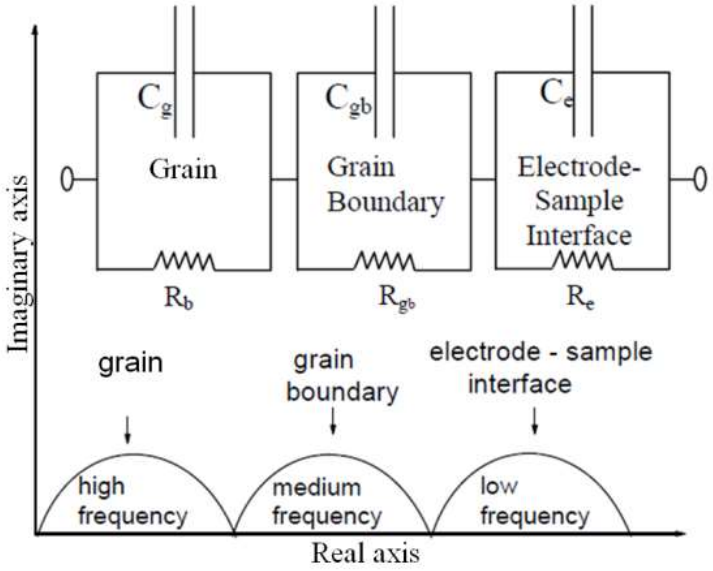


Fig. 3.11 An illustration of the relationship between the electrical properties with grain, grain boundary and interface [14]

In the present study, Solartron SI 1260 frequency response analyser shown in Fig. 3.12 was used to calculate the electrical conductivity of the sintered samples in the frequency range of 10^2-10^6 Hz with RMS value of AC signal ±0.1 V. The platinum/gold-coated sintered pellets were placed in between the two platinum electrodes, and the whole setup was further placed

inside a ProboStat by NORECS. ProboStat is a sample holder specially designed for high-temperature characterisations under controlled atmospheres. Z view software has been employed to study the electrical response of the various components. The resistance was calculated from the intercept of the real part of impedance with the *x*-axis. The capacitance plays a vital role in identifying the component of the material. From the capacitance values listed in Table 3.2, one can determine whether the contribution to the conductivity is from the grains, grain boundaries or the electrode interface [15].

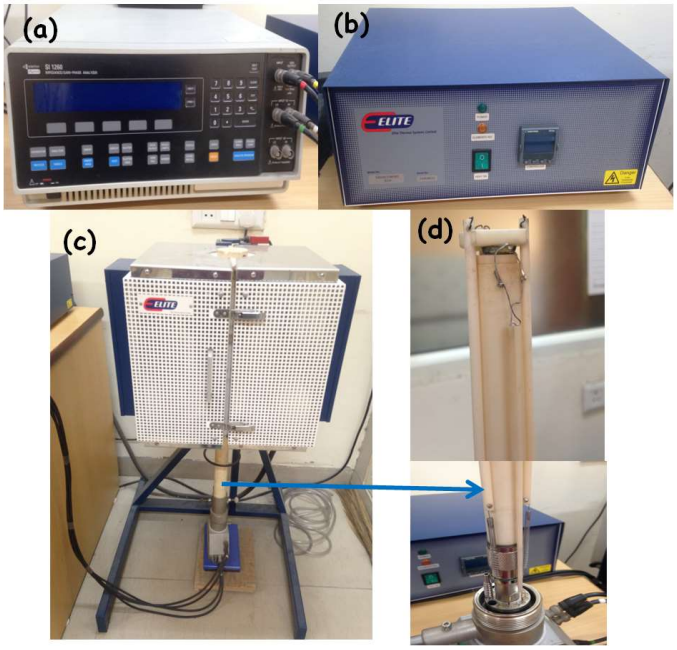


Fig. 3.12 (a) Solartron SI 1260 frequency response analyser, (b) temperature monitor showing the real and programmed temperature, (c) ProboStat containing the sample holder and (d) enlarged view of the sample holder

Table 3.2 Standard capacitance values of different microstructural parts of the sample and electrode [16]

Capacitance (F)	Microstructural parts and electrode
10^{-12}	Grain
10^{-11}-10^{-9}	Grain boundary
10^{-7}-10^{-5}	Electrode

The slope of the following Arrhenius equation gives the activation energy (E_a) of the system:

$$\sigma T = A\, exp^{-\frac{E_a}{kT}} \tag{3.13}$$

where A is a constant, T is the temperature in Kelvin, σ is the conductivity, and k is the Boltzmann constant. The change in the slope of the Arrhenius curve shown in Fig. 3.13 corresponds to the change in the charge carriers. The activation energy gives a fair idea about the type of conduction, i.e. ionic or electronic.

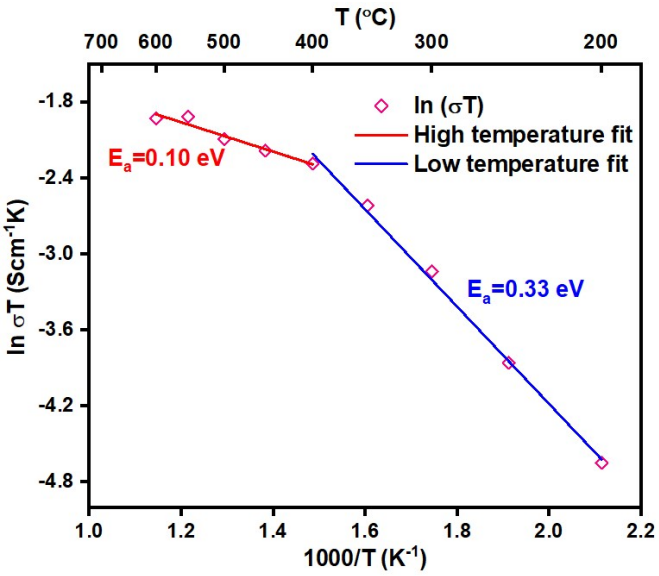


Fig. 3.13 Representative Arrhenius plot of SZC-20. The slopes of the two curves give the E_a of the low and high-temperature regions

3.3.10. Ultraviolet-visible (UV) spectroscopy

The optical band gap and defects are other ways to get indirect information about the conduction mechanism. Band gap refers to the energy difference between the top of the valence band and the conduction band's bottom. Based on the band gap, the conduction mechanism in different categories of materials such as insulators (>3 eV), semiconductors (≤0.5-3 eV) and metals (complete overlap) can be understood. UV-visible spectroscopy is used to find the band gap as well as the Urbach energy of the materials. Urbach energy is related to the different defects present in the sample. UV-Visible spectrometer measures the intensity of light passing through the sample (I) and compares it to the calibrated intensity

(I_o). The ratio I/I_o is called the transmittance for a particular wavelength [17]. The following relation defines the absorbance (A):

$$A = -\log\left(I/I_o\right) \tag{3.14}$$

Based on the optical absorption, Tauc proposed estimating the band gap energy of amorphous semiconductors. This method is based on the assumption that the energy-dependent absorption coefficient α can be expressed by the following equation [18]:

$$(\alpha h\nu)^{1/\gamma} = B(h\nu - E_g) \tag{3.15}$$

where h is the Planck constant, ν is the photon frequency, E_g is the band gap energy and B is a constant. The γ factor depends on the nature of the electron transition and is equal to 1/2 or 2 for the direct and indirect transition band gaps, respectively. Due to the internal inhomogeneity, the band gap energy is usually determined from diffuse reflectance spectra for the powdered (solid) samples. The propagation of light through such inhomogeneous media differs significantly from the propagation of light in a homogeneous material since the light scatters off points in its path. According to the theory presented by Kubelka and Munk [19], the measured reflectance spectra can be transformed to the corresponding absorption spectra by applying the following Kubelka-Munk function (F(R_∞)):

$$F(R_\infty) = \frac{K}{S} = \frac{(1-R_\infty)^2}{2R_\infty} \tag{3.16}$$

where $R_\infty = \frac{R_{sample}}{R_{standard}}$ is the reflectance of an infinitely thick specimen, while K and S are the absorption and scattering coefficients, respectively. Putting $F(R_\infty)$ instead of α into equation (3.15) yields the following form:

$$(F(R_\infty).h\nu)^{1/\gamma} = B(h\nu - E_g) \tag{3.17}$$

E_g is determined from the extrapolation of the linear portion of the plot of $(F(R)h\nu)^n$ against $h\nu$. The Urbach energy (E_u) which is the measure of the disorder is calculated from the plot of $F(R)$ vs $h\nu$. A double beam UV-Vis spectrophotometer with diffuse reflectance (Model: Shimadzu, UV-2600) was used in the present study. The measurements were made on finely powdered samples in the UV-Visible range, i.e. 250-800 nm with a slit width of 5 nm (Fig. 3.14).

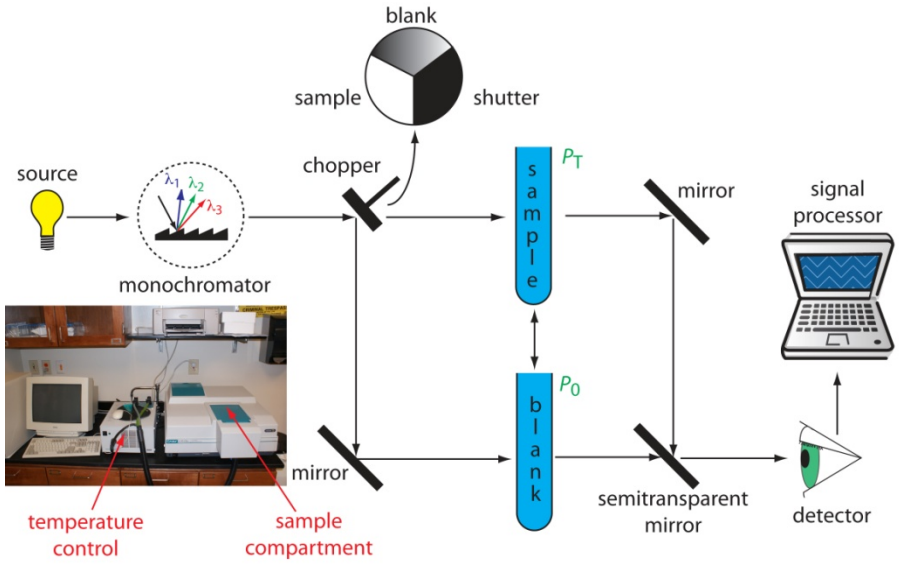


Fig. 3.14 Diagrammatic representation of a UV-Vis spectrometer setup

3.3.11. Photoluminescence (PL) spectroscopy

Impedance spectroscopy requires samples to be solid sintered pellets. However, one of the samples from the defined compositions, i.e. Ni-doped $SrZrO_3$, exhibited cracks and were very brittle; therefore, conductivity analysis using an impedance analyser was difficult. Therefore, optical and PL spectroscopy is performed to understand the nature of Ni-doped samples, variation of defects, and their types. PL spectroscopy is a contactless, non-destructive method of probing the electronic structure of materials. The PL data gives information about the kind of impurities, band gap, impurity activation energy, ordering and disordering of the system. The emission spectra arising in the visible region of the PL spectra denote defects originating from oxygen vacancies in the systems [20]. The intensity variations of the PL spectra peaks

give an account of the order or disorder in the system. An estimate of the composition of the compound can be made from the peak intensity of PL spectra.

In PL spectroscopy, light is directed onto the sample, where it is absorbed and imparts excess energy into the material in a process called photo-excitation. The sample can dissipate this excess energy through the emission of light or luminescence. In the case of photo-excitation, this luminescence is called photoluminescence. Photo-excitation causes electrons within a material to move into permissible excited states. When these electrons return to their equilibrium states, the excess energy is released, including the emission of light (a radiative process) or may not (a non-radiative process). The energy of the emitted light (photoluminescence) relates to the difference in the energy levels between the two-electron states involved in the transition between the excited state and the equilibrium state. The quantity of the emitted light is related to the relative contribution of the radiative process. The measurements for the present study were performed using a fluorescence spectrophotometer (Model: Agilent Carry Eclipse, G9800A) equipped with a xenon flash lamp.

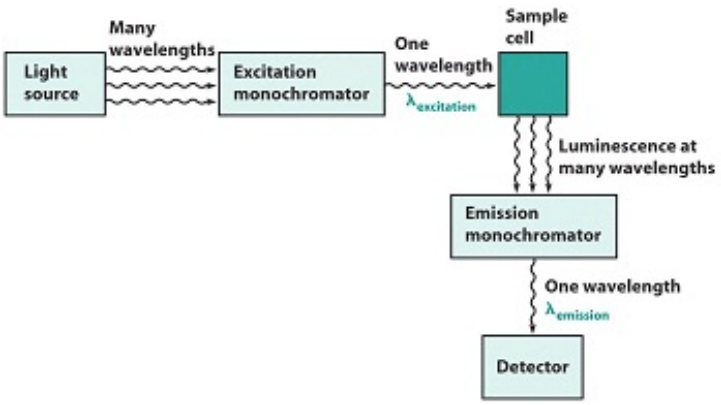


Fig. 3.15 Diagrammatic representation of the PL setup [21]

3.3.12. Vickers hardness

Anomalies in the thermal expansion give rise to the thermal strain in the samples. Furthermore, these strains lead to separation, delamination, cracks etc., in the different SOFC components. Moreover, the SOFC can be developed as anode supported or cathode

supported, i.e. the thickest layer corresponds to either anode or cathode, respectively. In both cases, mechanical properties play a significant role to support the cell units. Therefore, the mechanical properties of SOFC components are essential for the durability and lifetime of the cell. Mitutoyo MVK-H0, Vickers micro indentation tester, was used to measure the hardness of the samples (Fig. 3.16).



Fig. 3.16 Pictorial representation of a Mitutoyo MVK-H0 Vickers micro indentation tester

Before the measurements, the sintered pellets were polished using SiC emery paper having a grit size of 2000 to get a smooth flat surface. After ultrasonically cleaning the samples in acetone media, the samples were subjected to an indentation test. An indentation load of 3 kgf was applied onto the pellets with a dwell time of 15 sec. The indents and the crack length were measured directly from the micro-hardness tester with the help of an optical microscope using the following equation:

$$HV = 1.8544 \frac{F}{d^2} \tag{3.18}$$

where HV is the Vickers hardness number, F is the applied force, and d is the diagonal length of the indentation. An average of five indentations at different locations over the test surface was used for the hardness measurement. From the indentation, the fracture toughness can also

be calculated, which gives information about the SOFC components. The life of the cell can be predicted based on this.

References

[1] M. Stygar, P. Kurtyka, T. Brylewski, W. Tejchman, R. Stasko, Metall. Foundry Eng. 39(2) (2013) 47-58.

[2] B.D. Cullity, Second ed., Addison-Wesley Publishing Company Inc., Reading (USA), 1978.

[3] G. Caglioti, A. Paoletti, F.P. Ricci, Nucl. Instrum. 3(4) (1958) 223-228.

[4] B.H. Toby, Powder Diffr. 21(1) (2006) 67-70.

[5] R. Sindhu, P. Binod, A. Pandey, First ed., in: A. Pandey, R, Hofer, M. Taherzadeh, K.M. Nampoothiri, C. Larroche (eds.), Elsevier, Amsterdam (Netherlands), 2015.

[6] J.K. Gill, O.P. Pandey, K. Singh, Int. J. Hydrog. Energy 37 (2012) 3857-3864.

[7] P.P. Khirade, A.B. Shinde, A.V. Raut, S.D. Birajdar, K.M Jadhav, Ferroelectrics 504 (2016) 216-229.

[8] I. Kashif, A. Ratep, Appl. Phys. A Mater. Sci Process. 120 (2015) 1427-1434.

[9] J.I. Goldstein, D.B. Williams, Amer. Soc. Metals, Ohio (USA), 1985.

[10] M. Walock, PhD thesis, University of Alabama, Birmingham (USA), 2012.

[11] M. Hunkel, H. Surm, M. Steinbacher, Second ed., Elsevier, Amsterdam (Netherlands), 2018.

[12] J.E. Shelby, Second ed., Royal Society of Chemistry, Cambridge (UK), 2005.

[13] A. Kumar, B.P. Singh, R.N.P. Choudhary, A.K. Thakur, J. Alloys Compd. 394 (2005) 292-302.

[14] B. Tiwari, R.N.P. Choudhary, IEEE Trans. Dielectr. Electr. Insul. 17 (2010) 5-17.

[15] E. Barsoukov, J.R. Macdonald, Second ed., John Wiley & Sons, New Jersey (USA), 2005.

[16] J.T.S. Irvine, D.C. Sinclair, A.R. West, Adv. Mater. 2(3) (1990) 132-138.

[17] Makula, J. Phys. Chem. Lett. 9 (2018) 6814-6817.

[18] E. Davis, N. Mott, Philos. Mag. 22 (1970) 0903-0922.

[19] P. Kubelka, F. Munk, Technol. Phys. 12 (1931) 593-599.

[20] G. Madhu, V. Biju, Physica E 60 (2014) 200-205.

[21] D.C. Harris, Eighth ed., W. H. Freeman and Company, New York (USA), 2006.

Overview

This chapter deals with undoped and systematic doping of Cu and Ni in $SrZr_{1-x}A_xO_{3-\delta}$ (A: Cu, Ni; $0.00 \leq x \leq 0.20$). XRD, SEM, FTIR, TG-DTA, dilatometry, and impedance spectroscopy are used to explore their structural, thermal, physical, and electrical properties. The results are discussed in light of crystal structure, oxygen vacancies distribution and their ordering, thermal expansion coefficient, etc., to check their suitability as cathode materials for SOFCs.

4.1. Undoped and Cu-doped $SrZr_{1-x}Cu_xO_{3-\delta}$ ($0.00 \leq x \leq 0.20$)

Strontium zirconate is a perovskite structure material having inherent vacant octahedral and tetrahedral sites in a simple cubic lattice. It is predominantly an ionic (protonic) conductor and exhibits a conductivity of the order of 10^{-6}-10^{-9} Scm^{-1} between 300-600°C [1]. The selection of aliovalent dopants at B sites leads to the creation of vacancies depending on the chemical nature of dopants, their amount and process parameters. In this chapter, the effect of copper doping into $SrZrO_3$ is studied. Different properties such as structural, thermal, physical and electrical are explored to check the suitability of these materials as SOFC cathodes.

4.1.1. XRD analysis

As given in Chapter 3, the samples were prepared by the solid-state reaction method. The final heat-treatment to the undoped and Cu-doped $SrZrO_3$ was given at 1500 and 1200°C, respectively, for 5 hrs. Various experimental techniques were used to investigate these heat-treated samples. The XRD patterns of $SrZr_{1-x}Cu_xO_{3-\delta}$ ($0.00 \leq x \leq 0.20$) shown in Fig. 4.1(a) corresponds to the orthorhombic phase (*Pbnm*) of $SrZrO_3$. Furthermore, the obtained XRD results have been verified using Rietveld refinement. The samples were refined with orthorhombic and cubic phases since $SrZrO_3$ has been reported to be stable at room temperature with an orthorhombic crystal structure. $SrZrO_3$ has multiple polymorphs and there are transformations between these depending on the temperature [2]. Although, the best fit was observed for the orthorhombic phase in the present case. The Rietveld refinement of the samples shows good agreement between the observed and the calculated pattern since the goodness of fit parameter (χ^2) value of all the samples approaches 1. For representation purposes, the refined pattern of SZC-10 is shown in Fig. 4.1 (b), while Table 4.1 lists the lattice parameters of all the samples.

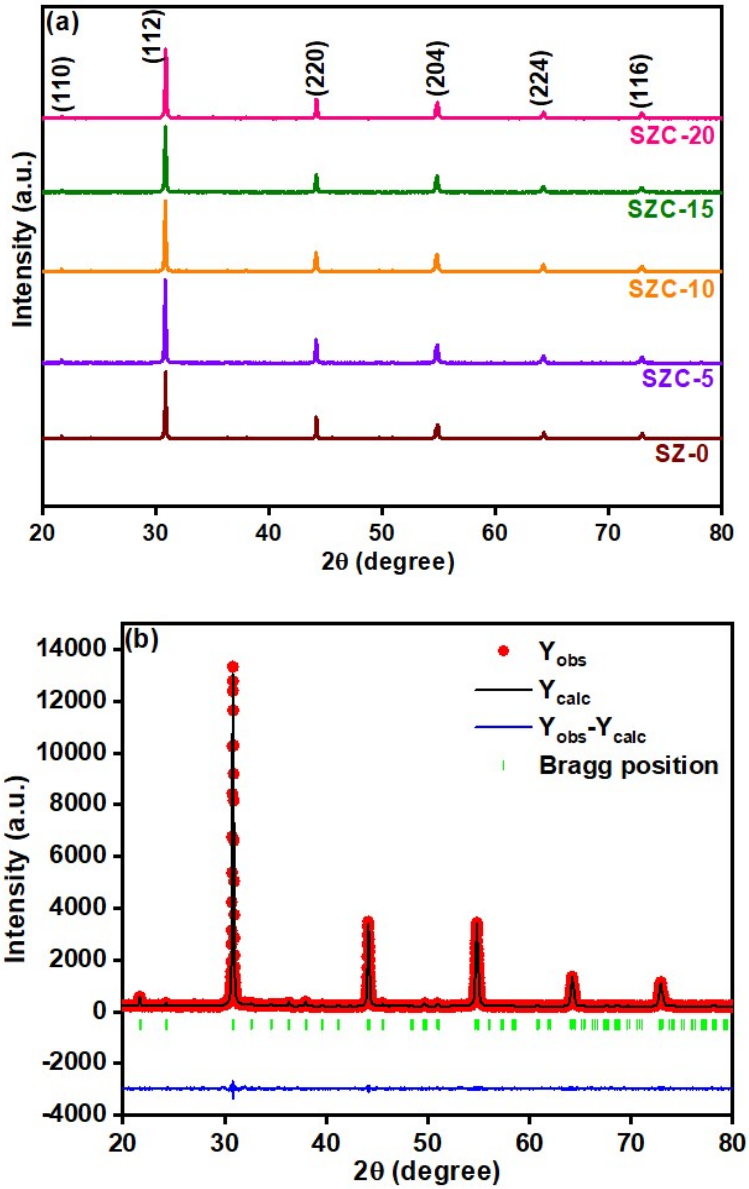


Fig. 4.1 (a) XRD patterns of $SrZr_{1-x}Cu_xO_{3-\delta}$ ($0.00 \leq x \leq 0.20$) and (b) refined XRD pattern of SZC-10 confirming orthorhombic structure with *Pbnm* space group

Table 4.1 shows the variation of the lattice parameters, which is in accordance with the shifting of the XRD peaks with respect to doping concentration. The lattice parameters vary linearly with the doping, indicating a single-phase formation [3]. The tolerance factor (t) of 0.71-0.9 confirms the orthorhombic phase formation [4]. On calculating the tolerance factor of the present samples using equation (1.6), it is inferred that the system is indeed orthorhombic since the value of t is 0.85. It is consistent with the XRD results. The copper

ions are expected to occupy the Zr site since the ionic radii difference is minimal compared with the Sr site [5]. Since the ionic radii of the host, Zr^{4+} is slightly lesser than the dopant, Cu^{2+} (0.073 nm) and Cu^{1+} (0.077 nm) in the coordination of 6; therefore, the incorporation of copper into the host lattice does not change the overall crystal structure of $SrZrO_3$ as given in the Appendix. However, the local structure of $SrZrO_3$ gets modified due to the charge difference between $Cu^{1+/2+}$ and Zr^{4+}. These modifications are related to the bending of the Zr-O octahedra [6].

Table 4.1 Lattice parameters of $SrZr_{1-x}Cu_xO_{3-\delta}$ ($0.00 \leq x \leq 0.20$) calculated from Rietveld refinement

Sample label	a (Å)	b (Å)	c (Å)	V (Å^3)	χ^2
SZ-0	5.785	5.812	8.194	275.54	1.00
SZC-5	5.788	5.812	8.194	275.75	1.00
SZC-10	5.792	5.813	8.196	276.03	1.03
SZC-15	5.789	5.812	8.194	275.76	1.03
SZC-20	5.792	5.813	8.198	275.07	1.75

It is well-known that doping leads to a shift in the XRD peaks and variation in the peak intensity. Fig. 4.2 shows the marginal shifting of the XRD peaks of the doped samples towards lower diffraction angles. It is due to incorporating a larger ionic radii dopant $Cu^{1+/2+}$ (0.077/0.073 nm) in place of Zr^{4+} (0.072 nm). On the other hand, the formation of oxygen vacancies can also shift the XRD peaks towards a higher diffraction angle since the ionic radii of oxygen vacancy is lower than that of the oxygen ion [7]. Furthermore, shifting of the SZC-20 peak towards higher angles could be attributed to the change in the valence state of copper since the ionic radii of $Cu^{1+/2+}$ is slightly greater than Zr^{4+}. There might be a possibility of copper being in the Cu^{1+} state initially (SZC-5 and SZC-10), which gradually changes into a Cu^{2+} state, particularly in SZC-15 and SZC-20. This change in the oxidation state of copper has been verified from the XPS results.

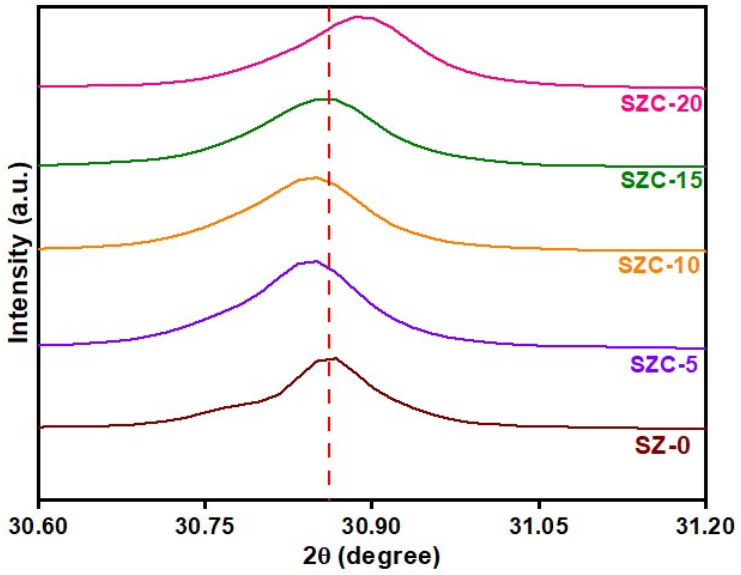


Fig. 4.2 Shifting of the highest intense XRD peak (112) with the incorporation of copper in the $SrZrO_3$ system

As seen in Fig. 4.3, copper is in the mixed-valence state, particularly in SZC-5 and SZC-10; however, in SZC-20, the effect of the Cu^{1+} state diminishes while Cu^{2+} becomes prominent. The presence of mixed-valence states of copper could also be associated with the broadening of the XPS peaks of SZC-5 and SZC-10. The XPS spectra of the SZC-20 sample have sharp peaks, which might correspond to the presence of fully oxidised Cu^{2+}. Since the XPS spectra of Cu_2O do not have any satellite peaks, copper's oxidation state is only +2. Moreover, the common and more stable oxidation state of copper is +2. It can also be manifested from their melting points since the melting point of CuO (1326°C) is higher than Cu_2O (1232°C), indicating that the CuO phase is more stable [8].

As for the intensity of the XRD peaks, copper doped samples exhibit higher full width at half maxima (FWHM) than the undoped sample. However, the FWHM could not show any trend with the dopant concentration, as shown in Table 4.2. The XPS results confirm the presence of copper in mixed states. The increasing dopant concentration increases the Cu^{2+} state, due

to which the vacancy formations reduce as compared with Cu^{1+} in $SrZrO_3$. Moreover, it could be possible that Cu might have also occupied Sr-site, particularly in SZC-20.

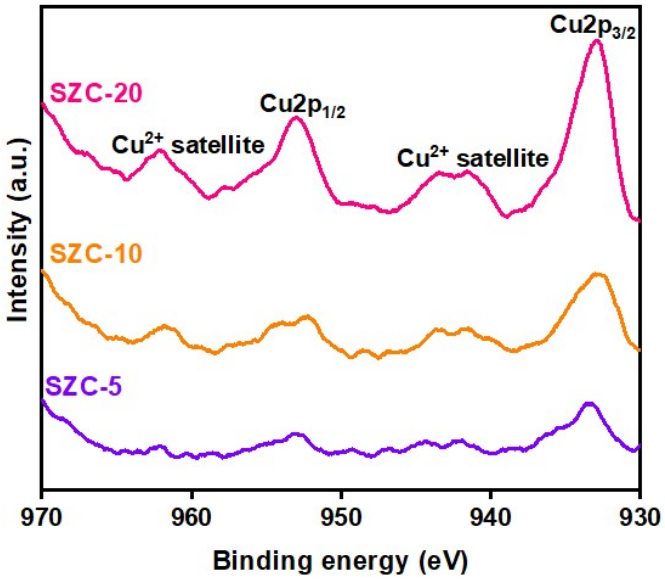


Fig. 4.3 XPS spectra of (a) SZC-5, (b) SZC-10 and (c) SZC-20

Table 4.2 FWHM and mean crystallite size of $SrZr_{1-x}Cu_xO_{3-\delta}$ ($0.00 \leq x \leq 0.20$) calculated for (112) peak

Sample Id	SZ-0	SZC-5	SZC-10	SZC-15	SZC-20
FWHM (°)	0.150	0.161	0.160	0.164	0.163
Crystallite size (nm)	66.95	57.50	57.66	54.59	56.26

The change in the valence of copper and the charge difference between Zr^{4+} and $Cu^{1+/2+}$ ions are responsible for the introduction of vacancies into the system. These vacancies cause a local modification in the parent lattice of $SrZrO_3$, which tilts the BO_6 (ZrO_6) octahedra, an orthorhombic crystal structure. The following defect relation represents the vacancies introduced in the system on doping Cu in place of Zr in $SrZrO_3$ [9]:

$$CuO \rightarrow Cu''_{Zr} + O_o^X + V_o^{\cdot\cdot} \tag{4.1}$$

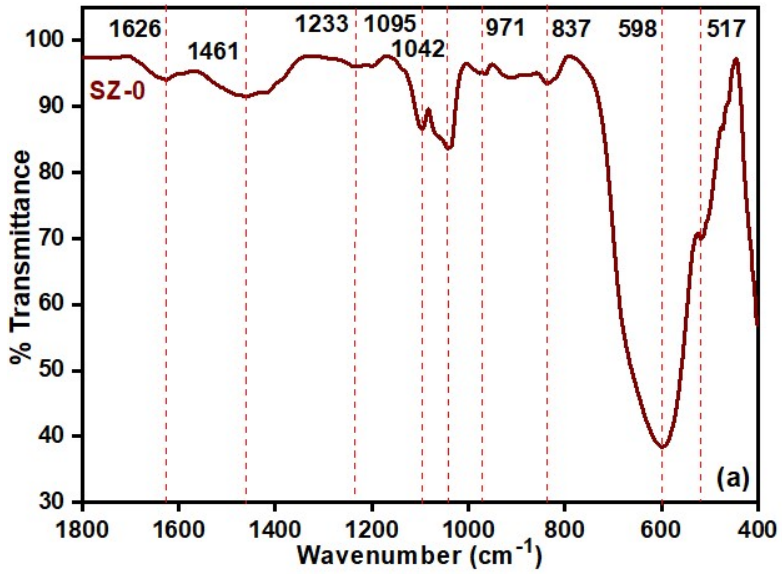
The following equation represents the defect equilibrium:

$$\frac{1}{2} O_2\,(g) + V_o^{\cdot\cdot} \leftrightarrow O_o^X + 2h^{\cdot} \tag{4.2}$$

These equations are according to the Kröger-Vink notation where Cu''_{Zr} denotes the copper ion at the Zr site, O_O^X represents the oxygen ion at the lattice and $V_O^{\cdot\cdot}$ represents the vacant oxygen site. The presence of these vacancies is essential for the conduction mechanism in perovskite oxides [10].

4.1.2. FTIR analysis

Fig. 4.4 (a) and (b) shows the FTIR spectra of $SrZr_{1-x}Cu_xO_{3-\delta}$ ($0.00 \leq x \leq 0.20$) having seven bands positioned around 1632, 1472, 1210, 1092, 993, 860 and 588 cm^{-1}, respectively. The variation in the position of the bands of the undoped and doped samples could be attributed to the change in the bond length and the presence of oxygen vacancies in the system [11].



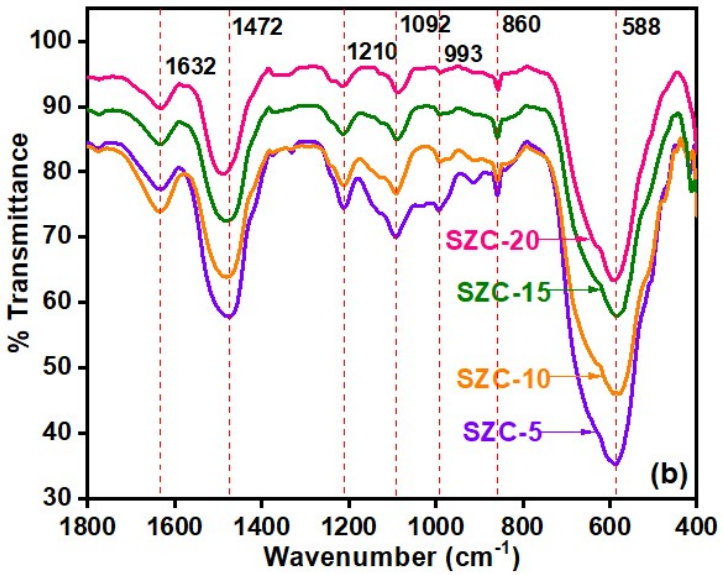


Fig. 4.4 FTIR spectra of (a) undoped and (b) Cu-doped $SrZrO_3$

The region between 850-400 cm^{-1} is attributed to the B-O vibrations, which, in this case, can either be of Zr-O or Cu-O [12]. The bands at 598 and 588 cm^{-1} for the undoped and doped samples correspond to the Zr-O stretching vibrations [13, 14]. In ceramic materials, the shifting of peaks towards higher or lower wavenumbers is related to the formation of stronger and weaker B (Zr)-O bonds, respectively. Therefore, shifting the bands ~598, 1095 and 1233 cm^{-1} towards lower wavenumber is associated with the partial substitution of $Cu^{1+/2+}$ in place of Zr^{4+}. Since the force constant decreases on doping $Cu^{1+/2+}$ into the $SrZrO_3$ system, due to the longer bond length of Cu-O bond than Zr-O bond in $SrZr_{1-x}Cu_xO_{3-\delta}$ ($0.00 \leq x \leq 0.20$) system. It, in turn, causes the bands to shift towards the lower wavenumber [15]. Also, introducing Cu into the $SrZrO_3$ system induces oxygen vacancies, which might be responsible for shifting these bands towards the lower wavenumber [16]. The bands at 1461 and 1472 cm^{-1} in the undoped and doped samples, respectively, could be due to the reaction of the samples with atmospheric CO_2. The water-related bands (O-H) at ~1626 and 1632 cm^{-1} in the undoped sample shift towards a higher wavenumber while the intensity of these bands increases with the increase in the dopant concentration, thereby confirming the hydrophilic nature of the

doped samples that might be related to a higher disorder/ defects containing surfaces of the samples [17-19].

4.1.3. Physical parameters

Table 4.3 lists the physical parameters such as relative density, molar volume, concentration, polaron radius and the distance between dopant ions. The hardness of these samples is also given in addition to the physical parameters in Table 4.3. An increase in the copper concentration leads to a significant increase in the density of the samples. In the present case, copper doping increases the sinterability of the samples, as observed in the following section, leading to an increase in the relative density and crystallinity, as discussed in Section 4.1.1. The sample with the maximum amount of dopant (SZC-20) is denser than any other sample. Since density is an additive property of material, this increase is attributed to the doping of CuO (6.31 gcm^{-3}), denser than ZrO_2 (5.68 gcm^{-3}). As seen in Table 4.3, the increase in the dopant concentration leads to an increase in the hardness of the samples. The hardness of the doped samples is comparable to the literature [20]. The molar volume of the samples is also following the expected results. Since CuO (79.545 $gmol^{-1}$) has a lesser molar mass than ZrO_2 (123.218 $gmol^{-1}$); therefore, there is a decrease in the values of the molar volume. The most dense SZC-20 has the lowest molar volume in the present samples. The concentration of ions per unit volume helps calculate the distance between Cu^{2+} ions and the polaron radius. The decrease in the concentration of dopant ions (N) leads to an increase in the distance between the Cu^{2+} ions. Therefore, SZC-5 has the lowest value of R. Since the polaron radius of all the samples is smaller than R but higher than the ionic radii of Cu^{2+}, it is inferred that the electrons in the system are localised [21].

Table 4.3 Relative density, hardness, molar volume, concentration, polaron radius and the distance between Cu^{2+} ions of $SrZr_{1-x}Cu_xO_{3-\delta}$ ($0.00 \leq x \leq 0.20$)

Sample label	ρ (%)	Hardness (GPa)	V_m (cm^3 $mole^{-1}$)	N ($\times 10^{22}$ cm^{-3})	r_p (cm)	R ($\times 10^{-8}$ cm)
SZ-0	70.73	1.39	30.89	-	-	-
SZC-5	85.57	3.89	25.19	7.57	9.52×10^{-9}	2.36
SZC-10	90.04	2.72	23.66	3.95	1.18×10^{-8}	2.93
SZC-15	92.32	4.19	22.78	2.68	1.34×10^{-8}	3.33
SZC-20	93.08	4.95	22.30	2.01	1.48×10^{-8}	3.67

4.1.4. Microstructural analysis

Fig. 4.5 (a-e) illustrates the SEM of $SrZr_{1-x}Cu_xO_{3-\delta}$ ($0.00 \leq x \leq 0.20$). They show the formation of grains, their shape and size with dopant concentration. Change in the morphology of the samples could be related to the doping effect. SZ-0, SZC-5, and SZC-20 samples exhibit homogeneously distributed spherical shaped grains. However, in the case of SZC-10, the grains are intact but not uniform in shape. Instead, there is a transition from spherically shaped grains to cubic shaped grains. The spherically shaped grains change into inhomogeneously distributed, agglomerated, and distorted cubic-shaped grains in SZC-15 (Fig. 4.5 (d)).

The intergranular connectivity confirms good sinterability with doping of copper into the $SrZrO_3$ system; however, it seems that the doping also acts as a grain growth inhibitor. It is supported by the decrease in the grain size and increase in the grain boundaries of the doped samples compared to the undoped sample. The grain size decreases up to SZC-15 and again increases for SZC-20. The change in the broadening of the XRD peaks also supports this change in the morphology of the samples with increasing grain boundaries. Table 4.4 lists the average grain size values of $SrZr_{1-x}Cu_xO_{3-\delta}$ ($0.00 \leq x \leq 0.20$). The grain size of the samples varies between 0.4-1.0 μm. The SEM results are consistent with the results of FTIR and physical parameters of these samples. Moreover, they are also consistent with the XRD

results since the FWHM of the doped samples increases in comparison with the undoped sample indicating higher disordering. As discussed in the XRD section, the Cu-doping also increases the sinterability of the samples, as evident from the relative density listed in Table 4.3.

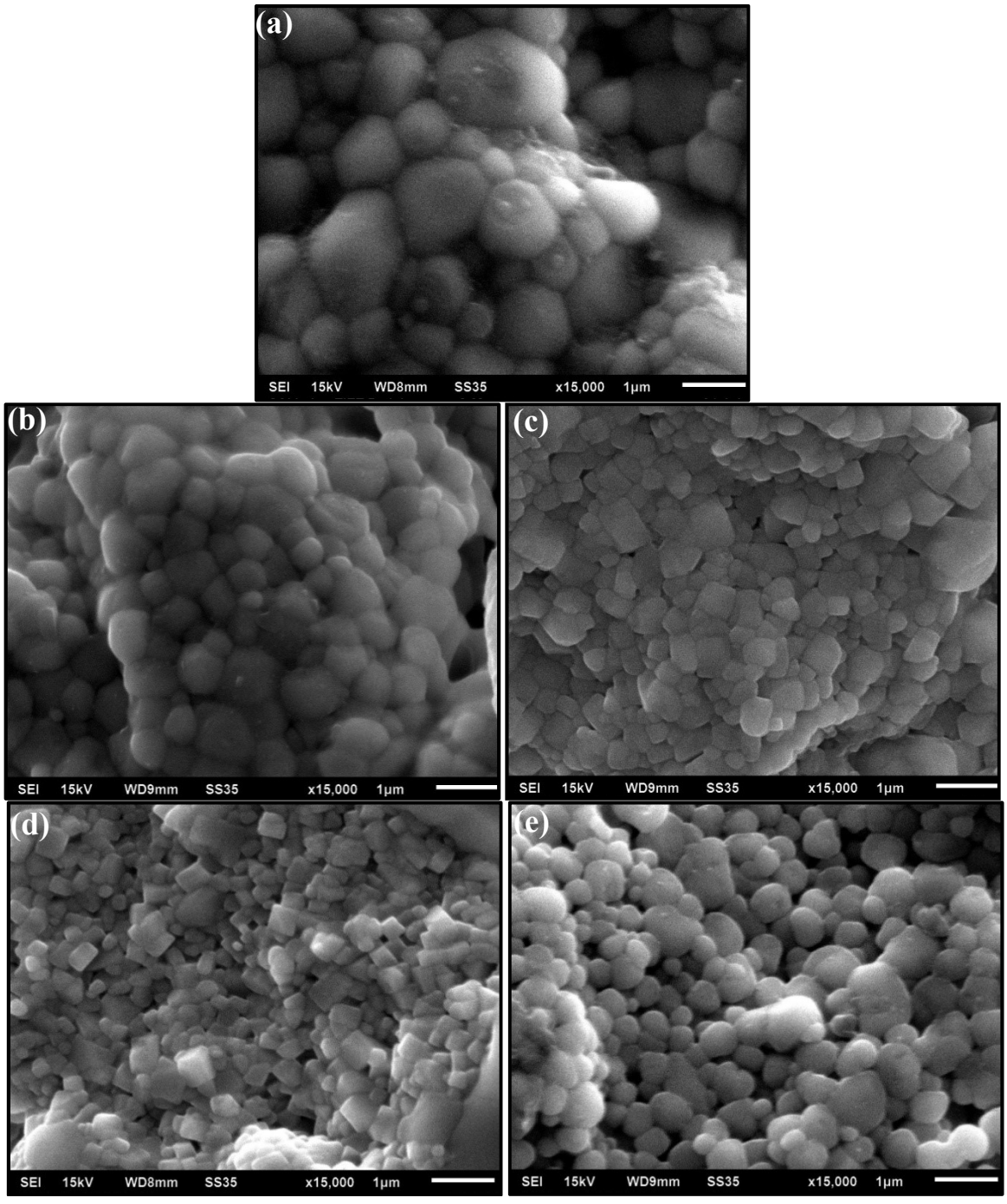


Fig. 4.5 SEM micrographs of (a) SZ-0, (b) SZC-5, (c) SZC-10, (d) SZC-15 and (e) SZC-20

The micrographs of the surface, particularly SZ-0, look dense; however, the relative density does not verify this observation. Since the relative density of SZ-0 is only ~70%, SEM of the fracture surface was also taken to confirm the presence of porosity in the samples. The representative fractured surface micrograph of SZ-0 shown in Fig. 4.14 (a) confirms the porosity in the present samples. The addition of copper has been known to refine the microstructure and increase the density of the samples leading to lower sintering temperatures. The lower melting point of copper favours the liquid phase sintering, which leads to higher density due to the increased diffusion process [22]. The density measurements of the samples also support this argument (Fig. 4.6).

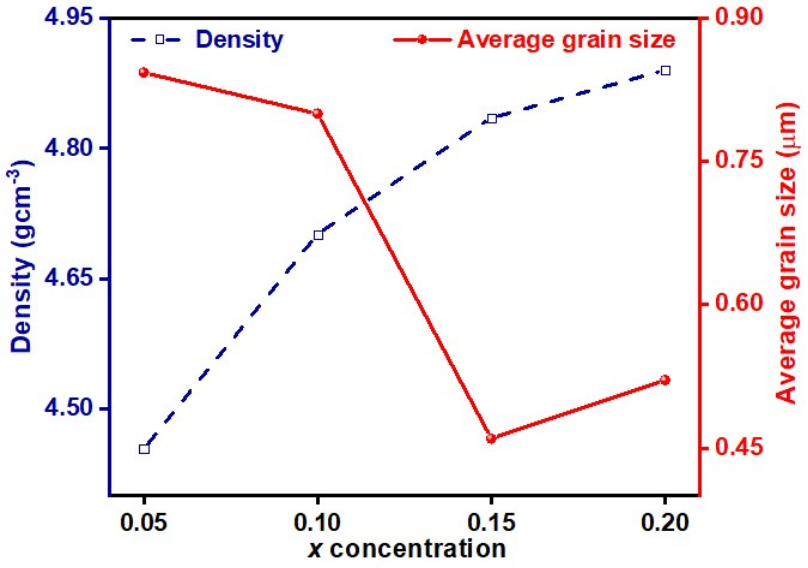


Fig. 4.6 Variation of density and grain size with an increasing Cu-dopant concentration in $SrZr_{1-x}Cu_xO_{3-\delta}$

The EDS data listed in Table 4.4 confirmed that the required stoichiometry is maintained even after sintering at a higher temperature of the undoped and doped samples.

Table 4.4 Average grain size and EDS data of $SrZr_{1-x}Cu_xO_{3-\delta}$ ($0.00 \leq x \leq 0.20$)

Sample label	Average grain size (µm)	Sr	Zr	Cu	O
		(wt %)			
SZ-0	1.03	36.77	41.84	-	21.39
SZC-5	0.84	37.02	41.48	0.16	21.35
SZC-10	0.80	38.90	39.71	0.29	21.05
SZC-15	0.46	38.88	39.11	0.95	21.06
SZC-20	0.52	38.37	40.31	0.13	21.19

4.1.5. TG-DTA analysis

Fig. 4.7 (a, b) shows the TG and DTA plots of SZ-0, SZC-10 and SZC-20 to get an idea about thermal stability and know about any phase transition of as-prepared samples up to the working temperature of SOFC. All the samples undergo discontinuous weight loss when heated up to 1000℃, which is correlated to the loss of water or lattice oxygen from the system. The weight loss in the undoped and doped samples occurs at three different stages. The first stage of the weight loss occurs until ~500℃. It is less than 0.5% due to the evaporation of water (H_2O) from the pores or the relaxation processes occurring within the system [23, 24]. Between 500℃ to 800℃, all the samples show weight loss; however, it is higher in the doped samples, i.e. SZC-10 and SZC-20. This weight loss might be associated with the lattice oxygen loss due to the change in the oxidation states of the transition element, i.e. $Cu^{1+/2+}$ in the samples. Above 800℃ till 1000℃, the change in the weight becomes constant in all the samples. It means that the system is stable in this range and could be suitable for use as cathode material for SOFCs above 800℃. Fig. 4.7 (b) shows the DTA curves of the undoped and doped samples. Above 700℃, no particular endothermic or exothermic peaks were observed, as reported in the literature [25-27]. However, many disturbances in this temperature range are observed, which might be related to the instrument or signal fluctuations during the experiment.

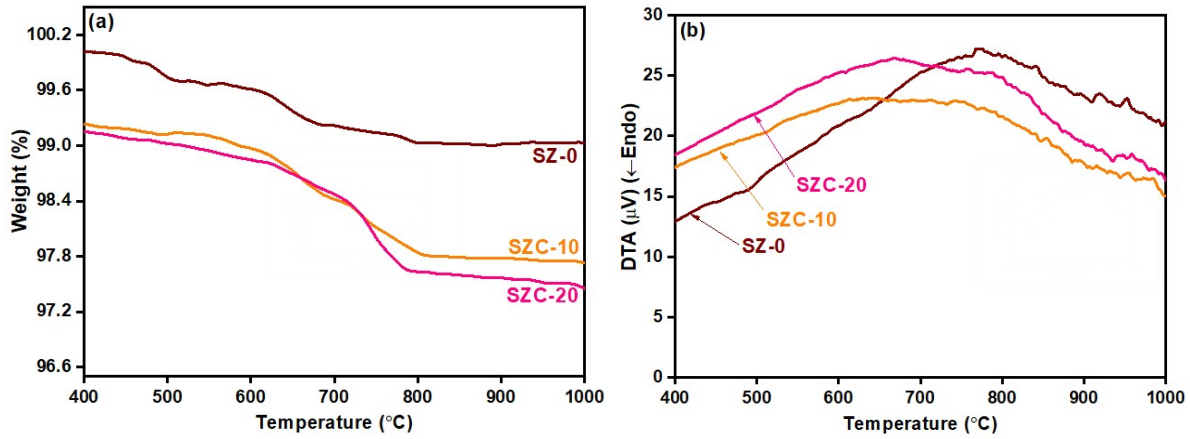


Fig. 4.7 Representative (a) TG plots (b) DTA curves of SZ-0, SZC-10 and SZC-20

4.1.6. Thermal expansion analysis

Fig. 4.8 shows all the samples' linear thermal expansion curves, indicating continuous linear thermal expansion with temperature. All the samples expand linearly with a slight difference in their slopes. The CTE of SZ-0, SZC-5, SZC-10, SZC-15 and SZC-20 is 12.68, 14.37, 14.11, 11.85 and 11.70×10^{-6} $°C^{-1}$, respectively, in the temperature range of 200-600°C. Initially, doped samples have higher CTE than the undoped sample; however, SCZ-15 and SCZ-20 have lower CTE than the undoped sample. It might be due to oxygen vacancies in the system because of $Cu^{1+/2+}$ doping for Zr^{4+} in $SrZrO_3$. The missing oxygen from the lattice lowers the interatomic bond strength and increases the CTE. The shifting of the bands towards lower wavenumber in the FTIR spectra of the doped samples also supports this decrease in the bond strength [28]. It is also supported by the difference in the field strength (F) of the cations calculated using the following formula:

$$F = \frac{z}{r_c + r_a} \tag{4.3}$$

where z is the charge of the element, r_c and r_a are the ionic radii of the cation and oxygen, respectively. As seen in the Appendix, copper's field strength is less than zirconia, which

implies that the bond strength decreases with copper substitution. Therefore, the decrease in bond strength increases the CTE of the doped samples compared to the undoped samples.

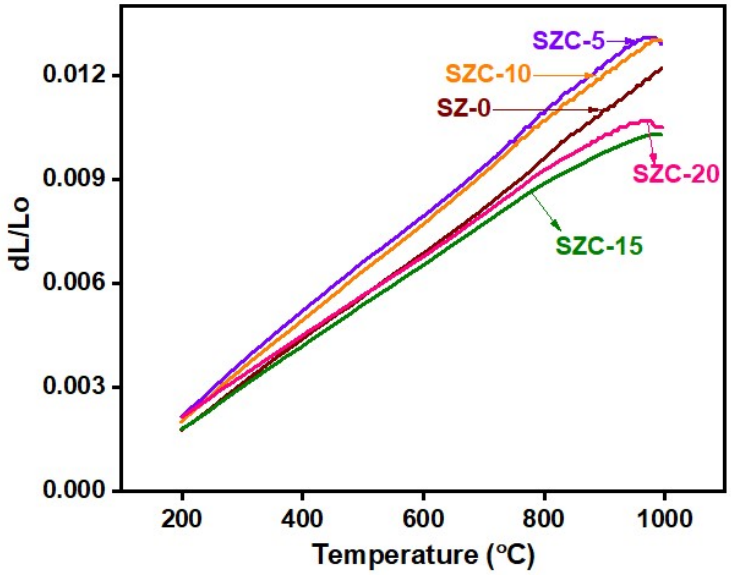


Fig. 4.8 Thermal expansion curves of $SrZr_{1-x}Cu_xO_{3-\delta}$ ($0.00 \leq x \leq 0.20$) measured in the temperature range of 200-1000°C

As the dopant concentration increases, a considerable decrease in the CTE values is observed. This decrease could be related to the ordering of oxygen vacancies with the copper concentration. An increase in the vacancies leads to a point where the vacancy concentration becomes ordered [29]. Since the interaction energy between a cation and anion is a fine balance between the Coulombic attraction and the internuclear repulsion. The ordering of oxygen vacancies makes the potential energy more symmetric, reducing the CTE [30, 31]. Also, the higher electro-negativity of copper compared to zirconia leads to an increase in the cation-anion bond (Appendix). It also leads to a decrease in the CTE of the system [32]. Conclusively, the CTE values of some samples such as SZ-0, SZC-15 and SZC-20 are in the required SOFC range ($9\text{-}13\times10^{-6}$ $°C^{-1}$), making them suitable for use as cathode materials for SOFCs.

4.1.7. Conductivity analysis

The impedance spectroscopy has been extensively utilised to check the suitability of ion conductors for major electrochemical devices such as SOFCs [33, 34]. The conductivity of the $SrZr_{1-x}Cu_xO_{3-\delta}$ ($0.00 \leq x \leq 0.20$) is calculated from the Nyquist plots. Fig. 4.9 shows the representative Nyquist plot of SZC-10 along with the corresponding equivalent circuit. The equivalent circuit consists of a series-connected parallel R-C circuit. Due to depressed semi-circles, the constant phase element (CPE) is taken instead of the capacitor. The capacitance of the two semi-circles is of the order of 10^{-10} F and 10^{-8} F, respectively. Since the capacitance of the second semi-circle is two orders higher than the first, it corresponds to the grain boundary, while the first corresponds to the grain contribution. Since grain boundaries are disordered than grains, depressed semi-circles observed in the samples might be due to varied reasons such as the polycrystalline nature of the samples, surface defects, multiple relaxations, inhomogeneity, and dispersion electrodes [35, 36]. It is observed that the resistance of all the samples decreases considerably with an increase in temperature and the dopant concentration.

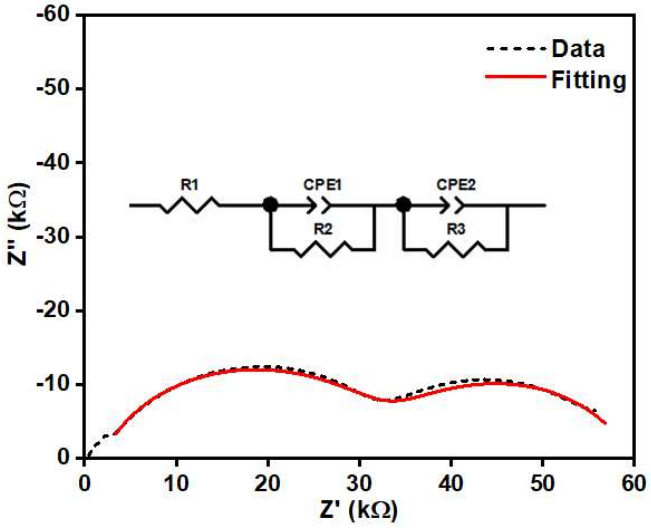


Fig. 4.9 Representative Nyquist plot of SZC-10 along with equivalent circuit measured at 350°C

An increase in the temperature gives rise to increased thermal motion of the ions, thereby resulting in higher conductivity. An increase in the dopant concentration enhances the conductivity of the samples due to the electron transfer between the ions of different oxidation states. Since copper has multiple valence states, it gets randomly distributed in the system. The lower valence dopant also creates oxygen vacancies providing adequate sites for ionic conduction to maintain the overall neutrality of the system. Zr^{4+}, on the other hand, could not contribute much to the conduction phenomena because of the absence of multiple valence states. Therefore, doping of Cu^{2+} into the system gives rise to electrical conduction [37]. Table 4.5 lists the conductivity values of $SrZr_{1-x}Cu_xO_{3-\delta}$ ($0.00 \leq x \leq 0.20$). The conductivities of low dopant concentrations, i.e. SZ-0 and SZC-5, are of the order of 10^{-5} Scm^{-1} at 600°C. While the conductivities of the highly doped samples, i.e. SZC-10, SZC-15 and SZC-20, are of the order of 10^{-4} Scm^{-1} at 600°C. These conductivity values are higher than that of the Fe-doped $SrZrO_3$, as reported by Misra et al. [37].

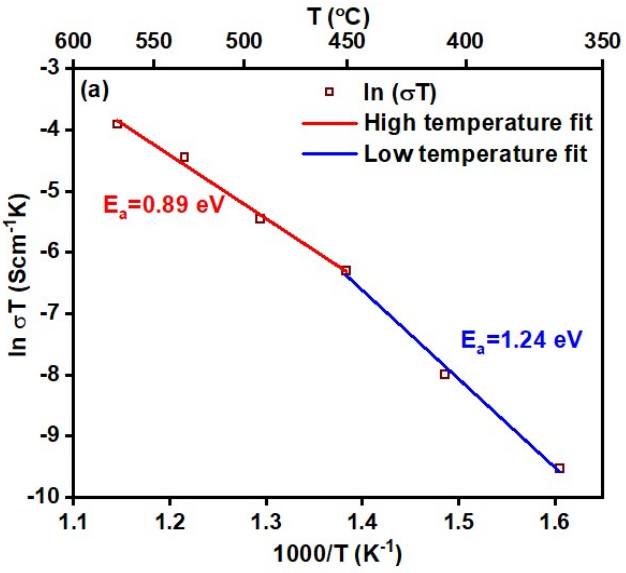
Table 4.5 Total conductivity (σ) of $SrZr_{1-x}Cu_xO_{3-\delta}$ ($0.00 \leq x \leq 0.20$)

Sample label	σ (Scm^{-1})		
	200°C	**400°C**	**600°C**
SZ-0	-	5.02×10^{-7}	2.29×10^{-5}
SZC-5	-	4.35×10^{-6}	8.47×10^{-5}
SZC-10	9.81×10^{-7}	1.26×10^{-5}	1.06×10^{-4}
SZC-15	1.72×10^{-5}	7.79×10^{-5}	2.63×10^{-4}
SZC-20	2.01×10^{-5}	1.50×10^{-4}	1.66×10^{-4}

As seen in the SEM micrographs, the grain size of the samples decreases with the increase in the copper concentration. It increases the number of grain boundaries per unit cross-sectional area also. The role of grain boundaries becomes vital in the low-temperature region than in the high-temperature region. According to the results, with an increase in the dopant concentration, the grain size decreases while the total conductivity increases due to the higher contribution of ionic conductivity. Generally, oxygen is released at elevated temperatures in

perovskite materials, increasing the number of randomly distributed oxygen vacancies. Large amounts of oxygen release lead to oxygen vacancy ordering that decreases the system's total conductivity, resulting in the decomposition of perovskite oxides into sub-oxides and pure metals [38, 39]. It might be the case with the decreasing conductivity in SZC-20 at 550°C in comparison to the undoped and doped samples.

The activation energy of the samples is calculated using the Arrhenius equation (equation 3.5) [40, 41]. The different slopes in the Arrhenius plot (Fig. 4.10 (a-c)) attribute to the change in the charge carriers with the temperature rise. Two different values of E_a as listed in Table 4.6 show that the copper doped samples have at least two different conduction mechanisms that could be associated with mixed electronic and ionic (protonic) conduction (MIEC). However, a further experiment in variable oxygen partial pressure is required to confirm the contribution of electronic and ionic conduction in the overall conductivity.



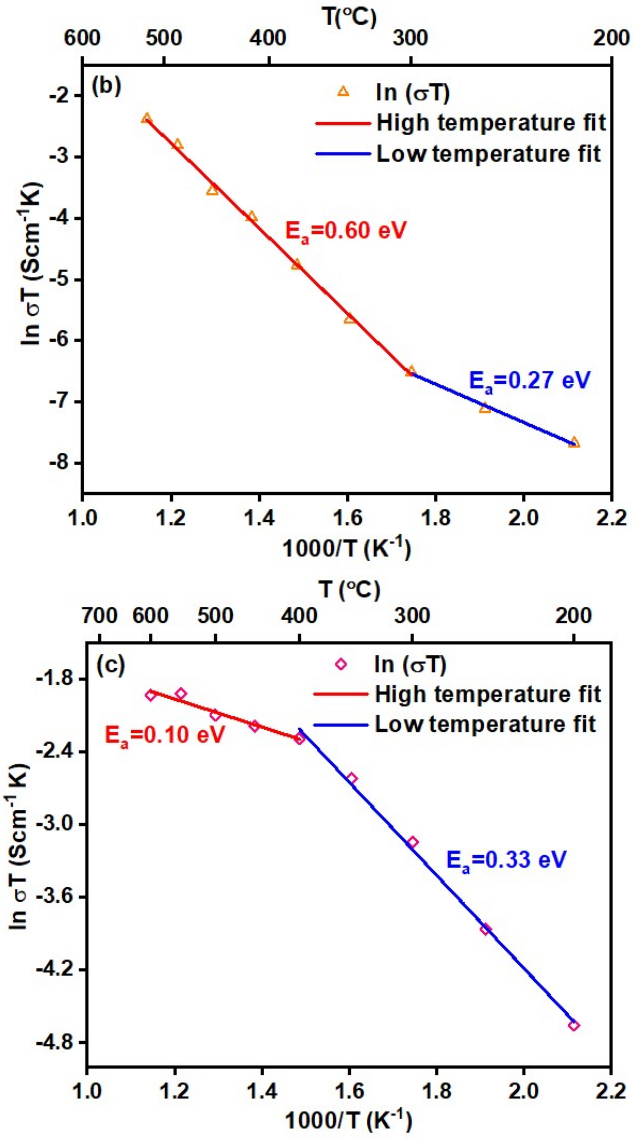


Fig. 4.10 Representative Arrhenius plots of (a) SZ-0, (b) SZC-10 and (c) SZC-20

Table 4.6 Activation energies (E_a) of $SrZr_{1-x}Cu_xO_{3-\delta}$ ($0.00 \leq x \leq 0.20$)

Sample label	E_a (eV)	Temperature range (°C)
SZ-0	1.24	350-450
	0.89	450-600
SZC-5	0.93	250-450
	0.71	450-600
SZC-10	0.27	200-300
	0.60	300-600
SZC-15	0.19	200-300
	0.37	300-600
SZC-20	0.33	200-400

4.2. Undoped and Ni-doped $SrZr_{1-x}Ni_xO_{3-\delta}$ ($0.00 \leq x \leq 0.20$)

In this section, nickel is doped in $SrZrO_3$, very similar to copper doping. Different characterisations have been performed to study the suitability of these materials for use as SOFC cathodes. However, due to the brittleness of these materials, the sintered pellets exhibit some cracks. Therefore, some characterisations such as density, hardness and conductivity analysis of these materials could not be performed. However, supporting characterisations such as UV-visible and photoluminescence spectroscopy have been performed to understand the presence of defects and their nature. The knowledge of defects is useful for conductivity analysis in these materials.

4.2.1. XRD analysis

The XRD patterns of $SrZr_{1-x}Ni_xO_{3-\delta}$ ($0.00 \leq x \leq 0.20$) are shown in Fig. 4.11 (a), while the refined representative patterns of SZN-5 are shown in Fig. 4.11 (b). As observed in the case of copper doped $SrZrO_3$, the XRD patterns of nickel doped $SrZrO_3$ are also monophasic and indexed with orthorhombic structure [42]. The well-defined intensity of the peaks confirms the highly crystalline nature of the samples. The refinement of all the samples confirms that the samples are monophasic without any impurity phase. The results are consistent with copper doped $SrZrO_3$ results. The increase in the substitution of Ni^{2+} increases the FWHM of the XRD peaks compared to the undoped sample. After doping Ni^{2+}, it becomes fairly constant (Table 4.7). It means grain size decreases and defects increase with Ni^{2+} substitution, as confirmed from the mean crystallite size of the samples listed in Table 4.7.

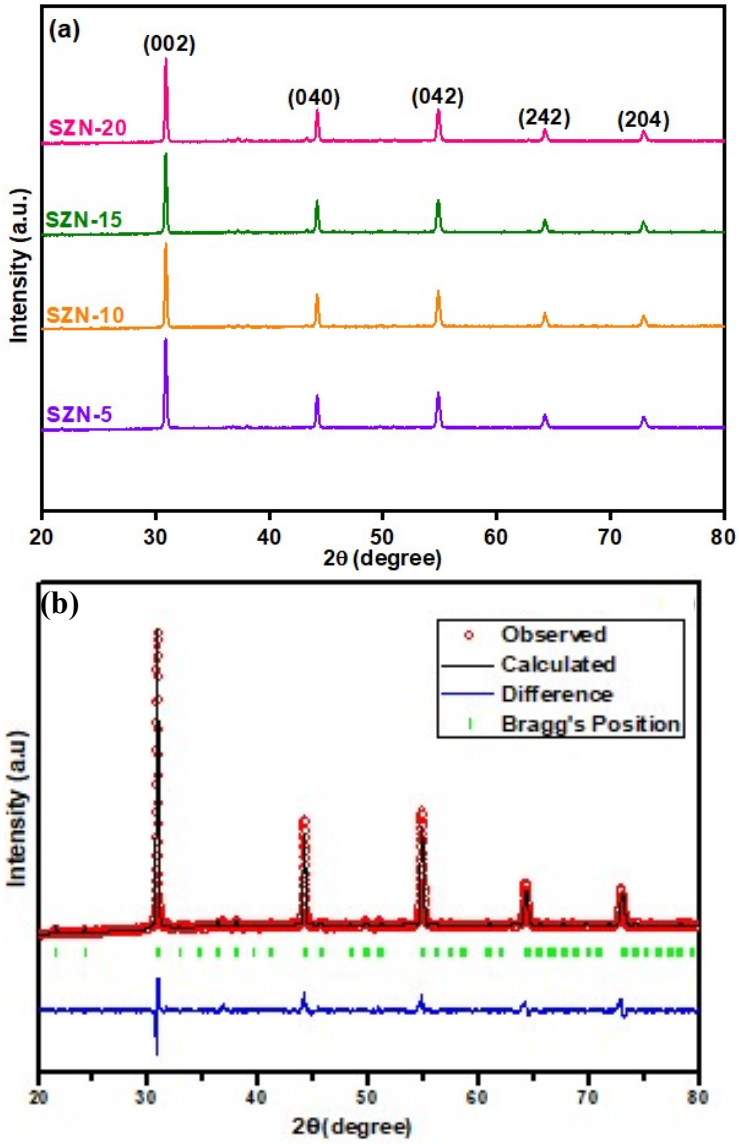


Fig. 4.11 (a) XRD patterns of $SrZr_{1-x}Ni_xO_{3-\delta}$ ($0.00 \leq x \leq 0.20$) showing the formation of a single-phase and (b) representative refined pattern of SZN-5

Table 4.7 FWHM and mean crystallite size of $SrZr_{1-x}Ni_xO_{3-\delta}$ ($0.00 \leq x \leq 0.20$)

Sample Id	SZ-0	SZN-5	SZN-10	SZN-15	SZN-20
FWHM (°)	0.150	0.224	0.218	0.226	0.218
Crystallite size (nm)	66.95	39.56	40.90	40.07	40.68

In Fig. 4.12, a slight shift in the peak positions towards higher angles implies that adding Ni^{2+} into the $SrZrO_3$ lattice induces compressive strain in all the samples except SZN-15. It is related to the lower ionic radii of Ni^{2+} (0.069 nm) than that of the host lattice (Zr^{4+}; 0.072

nm). Similar to Cu-doped samples, the doping does not change the overall crystal structure of $SrZrO_3$; however, it does introduce slight structural distortion into the BO_6, i.e. ZrO_6 octahedral. The partial substitution of Ni^{2+} at the Zr^{4+} site modifies the local structure due to the changes in their valence states, leading to the formation of oxide ions vacancies. Since these substitution ions occupy the perovskite structure's B-site, the modifications are related to the ZrO_6 octahedron [6].

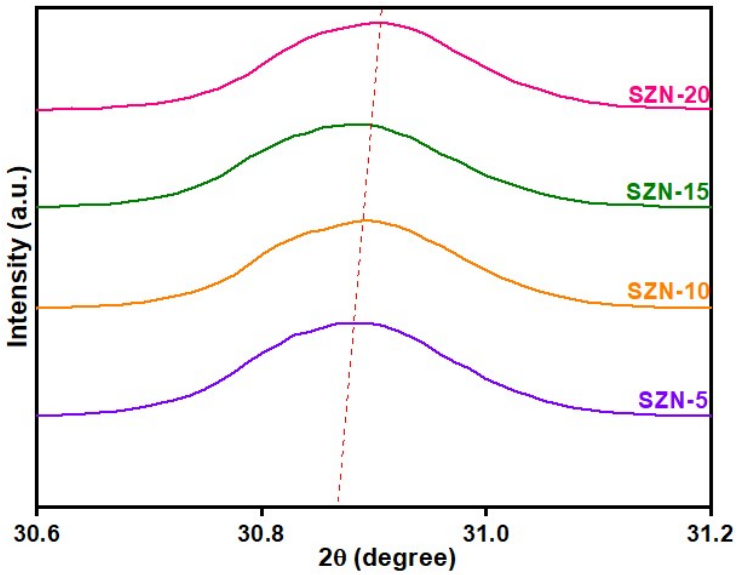


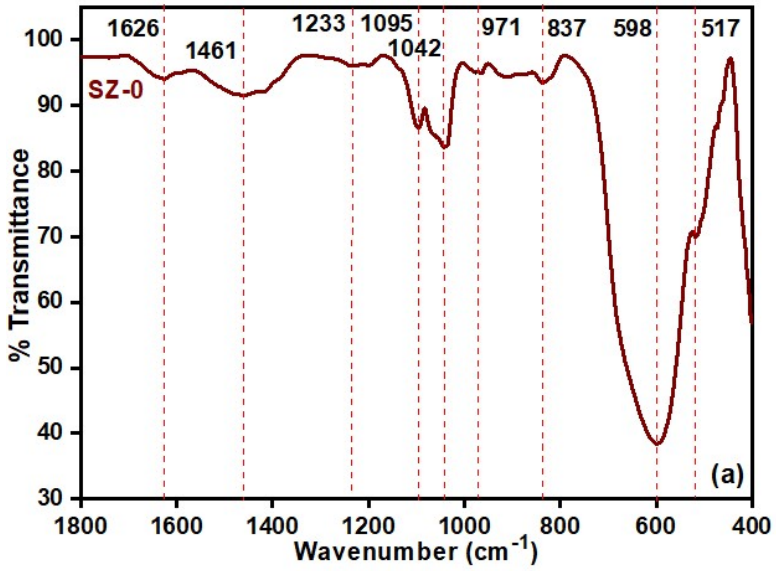
Fig. 4.12 Slight shifting of the XRD peaks corresponding to the (002) peak towards higher angles confirming compressive strain in the lattice

4.2.2. FTIR analysis

Fig. 4.13 (a) and (b) represent the FTIR spectra of the undoped and Ni-doped $SrZrO_3$. Five major absorption bands are observed at 598, 860, 966, 1222 and 1494 cm^{-1}, along with some minor bands at 421, 1075, 1134, 1216, 1627 and 1778 cm^{-1}. As in the case of $SrZr_{1-x}Cu_xO_3$ ($0.00 \leq x \leq 0.20$), the modes above 500 cm^{-1} represent the bond stretching of Zr-O. The bands ~421 and 520 cm^{-1} in the doped samples and 517 cm^{-1} in the undoped samples are related to ZrO_2. The spectrum shows a broad absorption band ~598 cm^{-1}. This band could be due to the

Zr-O stretching vibrations. The variation in the FTIR spectra of doped and undoped samples can be attributed to oxygen vacancies in the system [11, 43].

Shifting of bands towards higher wavenumber is related to the formation of shorter and stronger metal-oxygen bonds. Shifting of the band ~598 cm^{-1} towards a higher wavenumber was observed for SZN-20, which can be attributed to the partial substitution of Ni for Zr with increased Zr-O bond strength [15, 16]. The band at 1626 cm^{-1} in the undoped sample also shifted towards a higher wavenumber, i.e. 1706 cm^{-1} and became sharpened in SZN-20, whereas it remains approximately the same in all other samples. Moreover, the band ~1771 cm^{-1} corresponds to the stretching and bending of O-H species. Particularly in the doped samples, the bands ~1494 cm^{-1} shift towards the lower wavenumber. As in Cu-doped samples, lower wavenumber bands are related to the octahedral of B-site cations in ABO_3 ($SrZrO_3$), and the intensity of the water-related bands ~1494, 1626 and 1778 cm^{-1} increases with the Ni doping [13, 19].



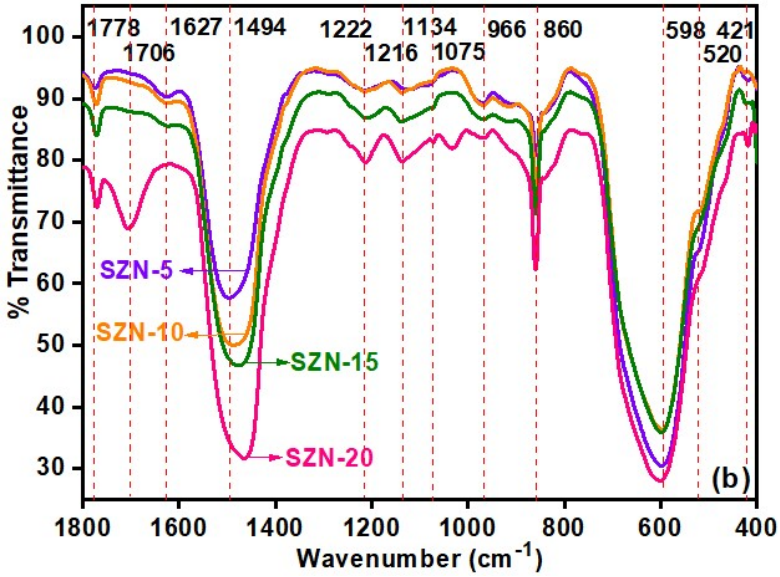


Fig. 4.13 FTIR spectra of (a) undoped and (b) doped $SrZr_{1-x}Ni_xO_{3-\delta}$ ($0.05 \leq x \leq 0.20$)

4.2.3. Microstructural analysis

The SEM micrographs of the fractured surfaces of $SrZr_{1-x}Ni_xO_{3-\delta}$ ($0.00 \leq x \leq 0.20$) are shown in Fig. 4.14 (a-e). These micrographs exhibit non-uniform morphology and a porous agglomerated form of the grains. The grains in the doped samples are of an equiaxed faceted type with pores. However, in the undoped sample, there are many open pores along with the coalescence of $SrZrO_3$ particles. As the Ni^{2+} concentration increases, the grains interlink, which justifies the single phase. It is consistent with the XRD results. Although the size of the crystallites increases with the increase in the Ni concentration, there is an increase in the agglomeration, which could be possible due to the presence of Ni^{2+} in the system.

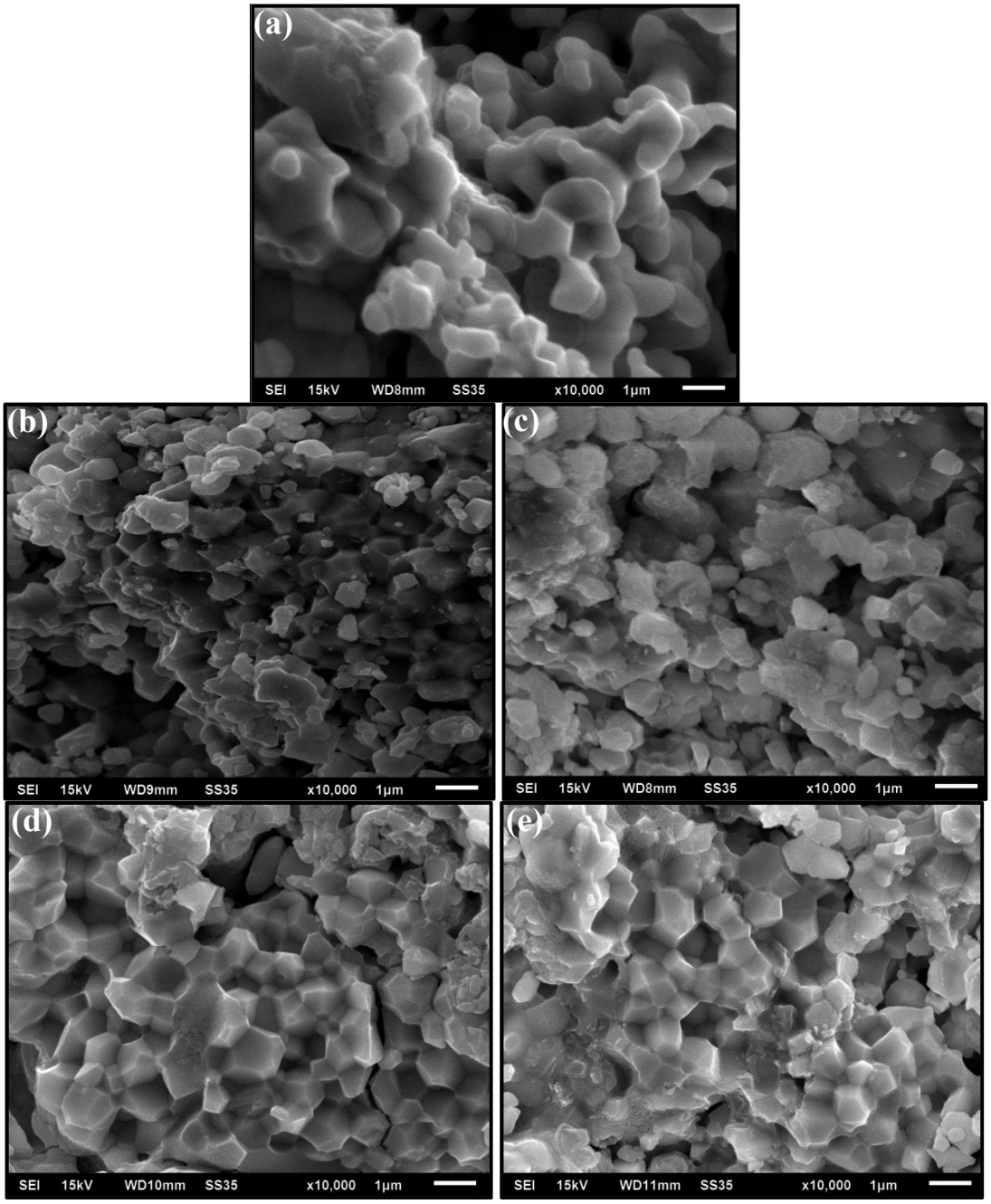


Fig. 4.14 SEM micrographs of fractured surfaces of (a) SZ-0, (b) SZN-5, (c) SZN-10, (d) SZN-15 and (e) SZN-20

Interestingly, in contrast to the Cu-doped samples, SZ-0 (undoped) sample shows some liquid phase sintering while the Ni-doped $SrZrO_3$ shows distinct and even more uniform grains. It implies that Ni doping changes the shape of the grains. The elemental composition of the

doped samples as listed in Table 4.8 confirms Sr, Zr and Ni elements without any impurity elements. It suggests that the expected stoichiometry did not deviate in the heat-treated samples.

Table 4.8 Elemental composition (wt. %) of $SrZr_{1-x}Ni_xO_{3-\delta}$ ($0.00 \leq x \leq 0.20$) obtained from EDS analysis

Sample label	Sr	Zr	Ni	O
	(wt. %)			
SZ-0	37.81	40.93	-	21.26
SZN-5	35.55	42.32	0.63	21.51
SZN-10	37.98	38.81	2.09	21.12
SZN-15	40.26	36.58	2.34	20.82
SZN-20	42.17	34.86	2.39	20.58

4.2.4. TG-DTA analysis

The TG plots of $SrZr_{1-x}Ni_xO_{3-\delta}$ ($0.05 \leq x \leq 0.20$) are shown in Fig. 4.15 (a). The weight loss is more distinct and increases with Ni-doping as compared with Cu-doped samples. Above 800°C, the weight loss in this case also becomes constant, denoting the system's good thermal stability in this temperature range. The initial weight loss is associated with the lattice oxygen loss and the removal of moisture from the samples. The DTA curves of the samples shown in Fig. 4.15 (b) are similar to the Cu-doped samples, with no prominent exothermic or endothermic peaks between 800-1000°C, indicating the stability of the orthorhombic crystal structure [26-28].

However, the pellets of these samples exhibit some cracks and are broken as observed after heat treatment. Therefore, to understand the reason for these cracks, more precise DSC measurements were done, particularly for these samples. Fig. 4.15 (c) shows endothermic peaks ~700 and 877°C, which, interestingly, could not be detected by DTA. According to the literature, these peaks correspond to orthorhombic to a pseudo tetragonal structure at ~730 °C and pseudo tetragonal to a tetragonal structure at ~860 °C, respectively [27]. Furthermore, it

is reported that the crystal structure and temperature of these transitions vary due to the presence of impurities, stoichiometry deviations and other processing parameters [27, 44-46]. As the dopant concentration increases, these phase transitions become more prominent. These phase transitions might be responsible for the crack development in the Ni-doped samples since the phase changes are related to the volume change during phase transformation in the samples. These transitions are also observed in the thermal expansion measurement of these materials, as discussed in the next section.

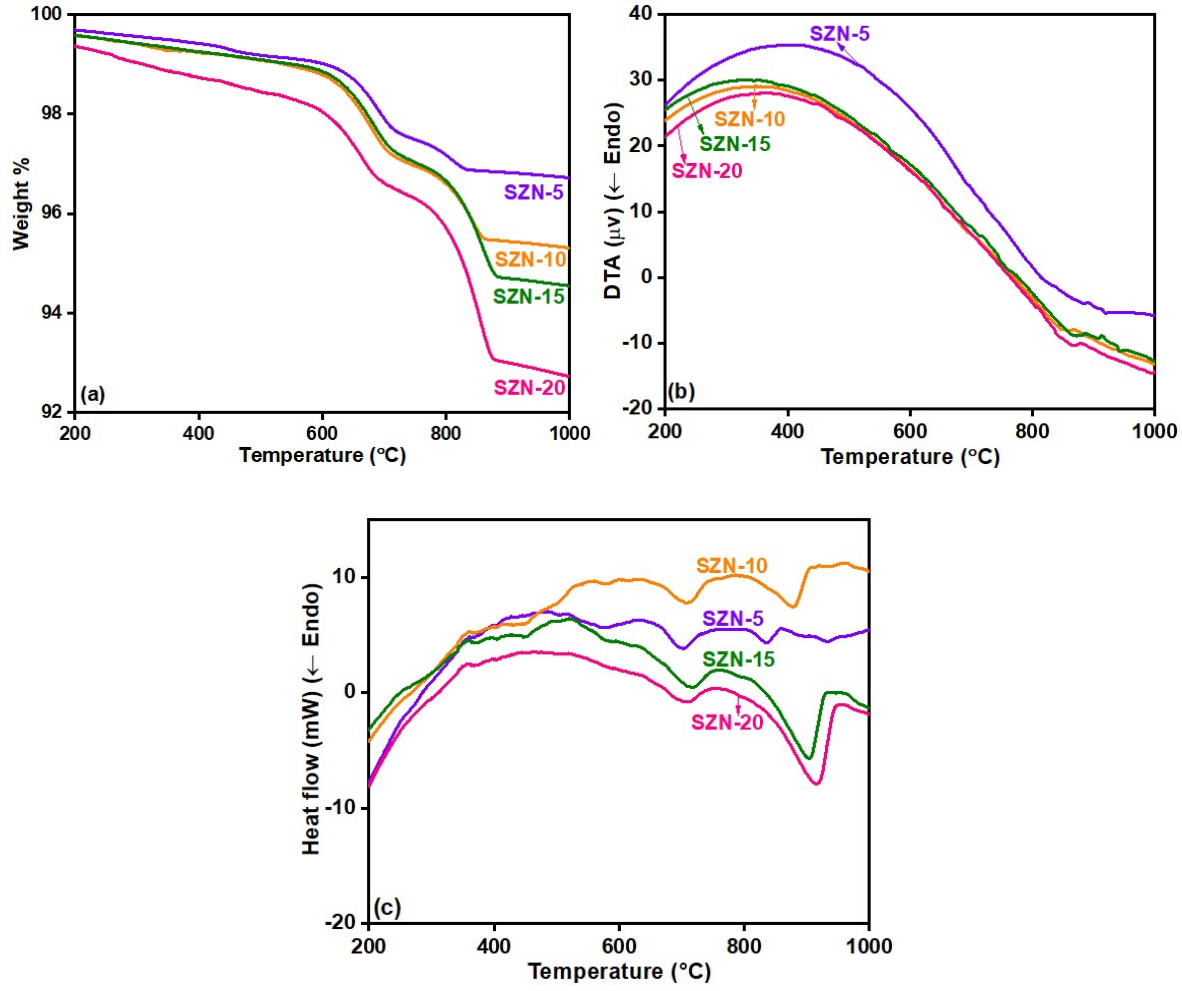


Fig. 4.15 (a) TG plots, (b) DTA and (c) DSC curves of $SrZr_{1-x}Ni_xO_{3-\delta}$ ($0.05 \leq x \leq 0.20$)

4.2.5. Thermal expansion analysis

Fig. 4.16 shows the linear thermal expansion curves of $SrZr_{1-x}Ni_xO_{3-\delta}$ ($0.00 \leq x \leq 0.20$). The CTE of SZ-0, SZN-10, SZN-15 and SZN-20 are 12.68×10^{-6}, 11.72×10^{-6}, 10.46×10^{-6} and 9.90×10^{-6} °C^{-1}, respectively. The CTE of the samples decreases considerably on doping Ni^{2+} due to the ordering of the oxygen vacancies as well as increasing bond strength with the increasing Ni^{2+} concentration. It is in correlation to the SEM results.

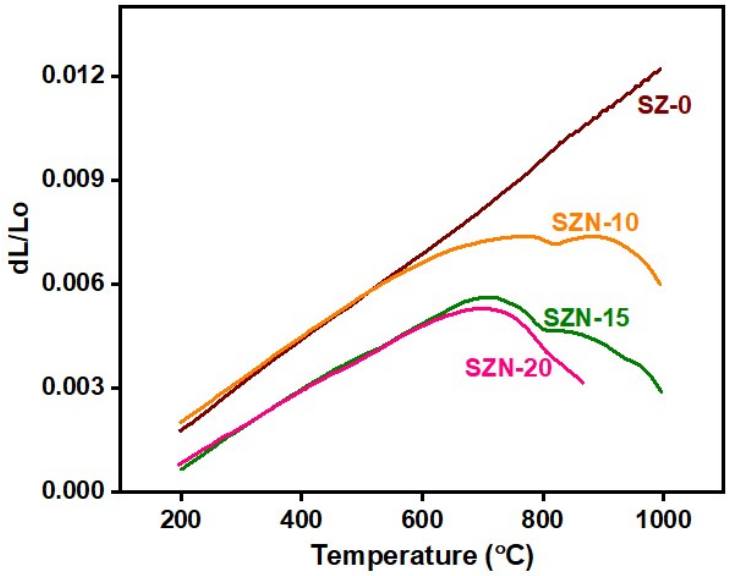


Fig. 4.16 Dilatometry curves of $SrZr_{1-x}Ni_xO_{3-\delta}$ (x=0.00, 0.10, 0.15, 0.20)

The charge difference between Ni^{2+} and Zr^{4+} gives rise to randomly distributed oxygen vacancies in the system. However, with higher Ni^{2+} concentration, these oxygen vacancies get ordered, thereby decreasing the CTE of the doped samples. The ordering of the oxygen vacancies makes the potential energy well more symmetric, resulting in the reduction of the CTE [30, 31]. The overall decrease in the CTE of the samples could also be due to the smaller ionic radii and larger electro-negativity of Ni^{2+} in comparison with Zr^{4+} (Appendix). However, the CTE of the $SrZr_{1-x}Ni_xO_{3-\delta}$ ($0.00 \leq x \leq 0.20$) is in the required SOFC range, i.e. $9\text{-}13\times10^{-6}$ °C^{-1}, making them suitable SOFC candidates. However, further research is required to qualify them as cathode materials for SOFC.

As a distinction from the Cu-doped samples, the temperature of maximum expansion known as the softening temperature is observed in the Ni-doped samples at higher temperatures (≥700°C). The presence of softening temperature in the doped samples could be due to the change in the crystal structure as observed from the DSC curves in Fig. 4.15 (c). At high temperatures, i.e. >600°C, the doped samples undergo a change in the crystal structure. The doping of Ni in $SrZrO_3$ decreases the phase transition temperature, as observed in Fig. 4.15 (c).

4.2.6. Band gap analysis

The sintered pellets of Ni-doped samples exhibit some cracks. So, it is challenging to find the conductivity of the sintered pellets. Because of these limitations, the optical band gap of these samples was performed to know at least their nature, whether they are wide band gap semiconductors or insulators. As observed from the inset of Fig. 4.17, SZN-5 has maximum reflectance of about 60%, which decreases considerably with the increase in the Ni^{2+} concentration.

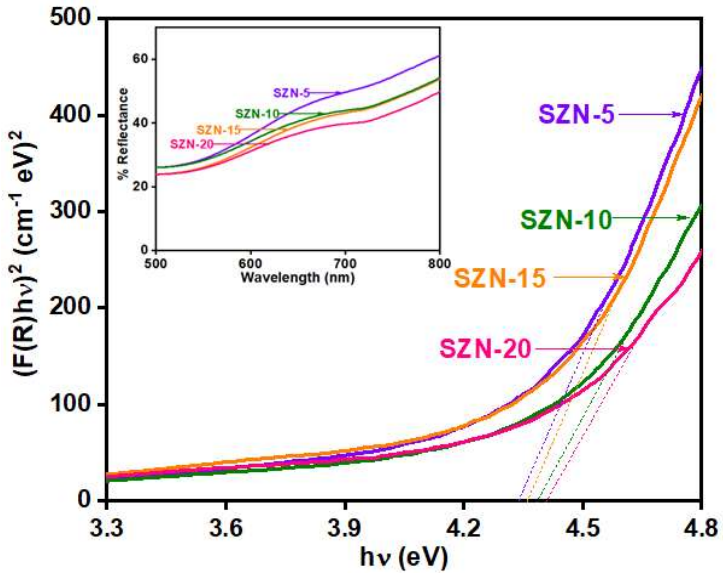


Fig. 4.17 Tauc plot of $SrZr_{1-x}Ni_xO_{3-\delta}$ ($0.05 \leq x \leq 0.20$) with diffuse reflectance spectra in the inset

The optical band gap is obtained using equation 3.17. It is in the insulating range for n=2, i.e. indirectly allowed transitions. According to the literature that $SrZrO_3$ has an indirect band gap since the valence band maxima do not lie at the same wave vector as the conduction band minima [47]. On the introduction of a divalent Ni^{2+}in place of Zr^{4+}, the Urbach energy (E_u) also increases with the increase in the band gap since Ni^{2+} creates some disorder in the structure [48].

The increase in the band gap on doping is attributed to the Moss-Burstein effect. Moss-Burstein effect states that with the increase in the dopant concentration, certain donor states are created, which push the Fermi level close to the conduction band above the occupied donor states. For an electron to jump from the valence band to the conduction band, more energy is required as the electron would have to cross the Fermi level. It leads to a large optical band gap [49]. In this case, the increase in the band gap may be attributed to the ordering of the structure, which is in accordance with the SEM micrographs. With the increase in the grain size, the number of energy levels due to defects between the conduction and valence bands starts decreasing, and the width of the impurity bands becomes narrow. Due to this, the gap between the valence and the conduction band increases with the defects [50]. This increase in the band gap and the ordering of the system suggest that the conductivity of such materials might decrease with increasing dopant concentration (Fig. 4.18). However, increasing defects suggests there is a possibility for ionic motion.

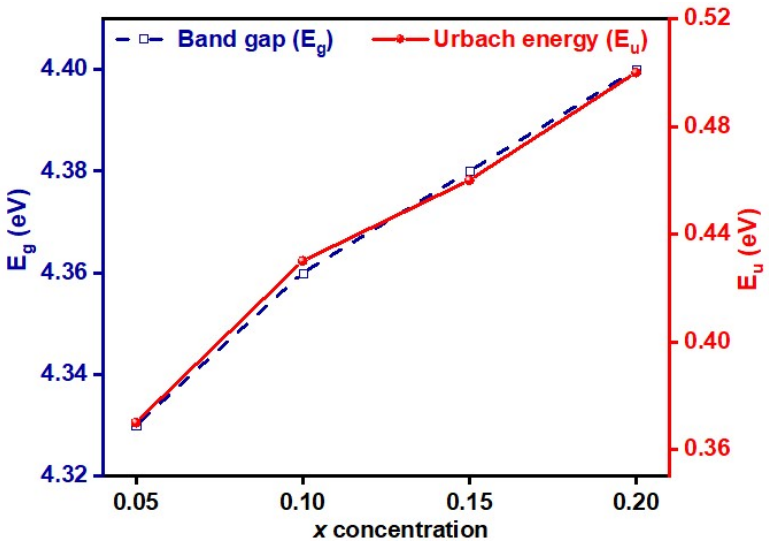


Fig. 4.18 Variation of E_g and E_u with increasing Ni-dopant concentration in $SrZr_{1-x}Ni_xO_{3-\delta}$

4.2.7. Photoluminescence analysis

The optical band gap and Urbach energy both increase with the dopant concentration. It indicates that the present samples might be having competitive conductors means electronic conduction decreases with increasing ionic conduction due to defects related to the Urbach energy. However, to confirm this hypothesis, the conductivity measurement could be performed on crack-free pellets. Based on the optical band gap results, the excitation wavelength of 237 nm was used to study the emission spectra of $SrZr_{1-x}Ni_xO_{3-\delta}$ ($0.00 \leq x \leq 0.20$) to find out more details of the defects and their distribution in the samples. As seen in Fig. 4.19 (a), the emission spectra cover part of the visible and ultraviolet spectrum.

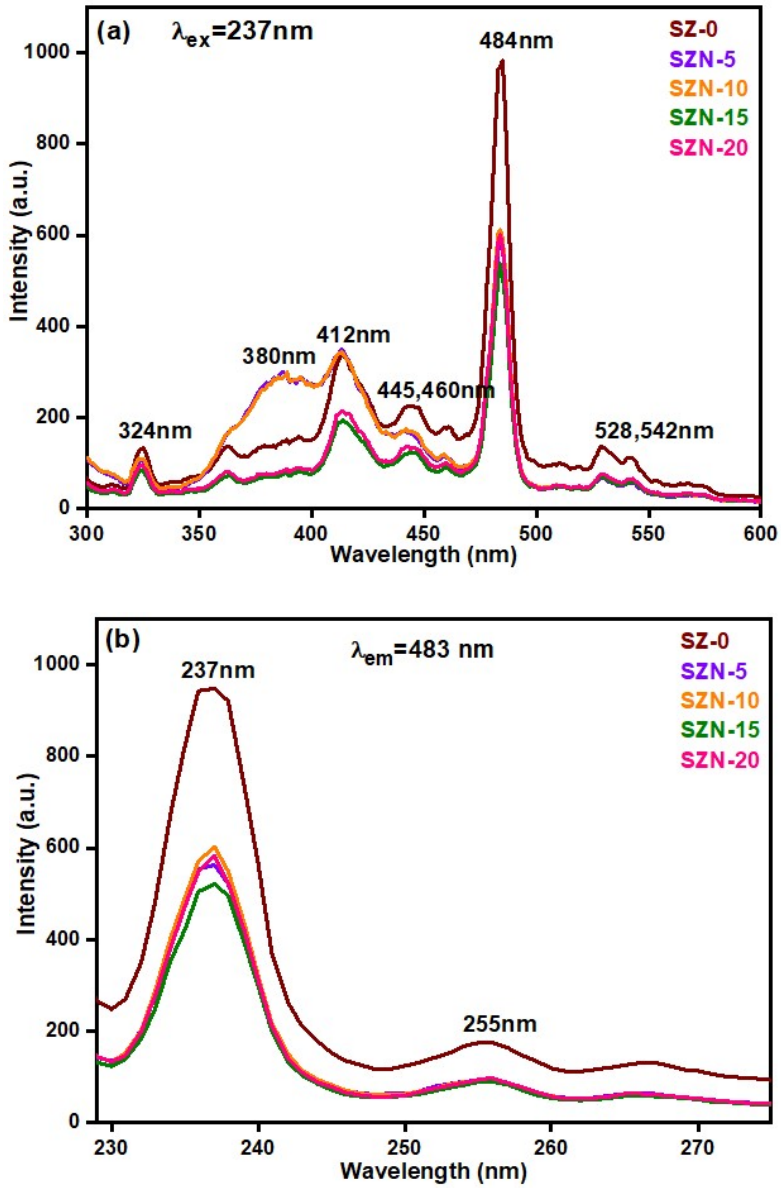


Fig. 4.19 PL (a) emission and (b) excitation spectra of $SrZr_{1-x}Ni_xO_{3-\delta}$ ($0.00 \leq x \leq 0.20$)

Major emission peaks observed are ~324, 380, 412, 445, 460, 484, 528 and 542 nm. As studied by Longo et al. [51], the violet and blue emissions observed in the Ni-doped $SrZrO_3$ PL spectra correspond to the shallow defects of Sr^{2+} while the green emissions are due to the ZrO_3^{2-} ions. Peak ~484 nm is a prominent one with the highest intensity. As reported by Gonzalez et al. [52], ZrO_2 exhibits two major emission peaks, which are ~447 nm and 485 nm. Therefore, the blue emission peak ~484 nm is thought to have aroused from interstitial defects in the lattice, oxygen vacancies and defect states in the $SrZrO_3$, while the emission

peaks ~520 nm originate when the holes trapped in deep level oxygen vacancies recombine with the electrons trapped at the shallow level located below the conduction band. The emission peaks in the UV region (380 nm) are due to the recombination of electrons and holes in the conduction and valence bands, respectively. While the emission peaks observed in the visible region are due to defects originating from deep level emissions (DLE) arising from oxygen vacancies [13, 53]. It is due to the large band gap of the present samples.

As shown in (Fig. 4.19 (b)), the excitation spectrum exhibits quite an intense peak at ~237 nm. According to the literature, this peak corresponds to the host absorption band (HAB). In this case, the charge transfer from the oxygen ligands to the ZrO_3^{2-}group takes place [42]. Elements having d^0 configuration shows no characteristic feature in the visible region, i.e. above 400 nm, due to which the absorption edges of all the samples, in this case, lie below 300 nm. As reported in the literature, the fundamental edge in $SrZrO_3$ perovskite is due to the transition from the O-2p valence band to the Zr-4d conduction band. The valence band in $SrZrO_3$ consists of Sr-4p and O-2s, whereas the conduction band consists of Zr-4d and O-2p [54].

The emission spectrum shows significant intensity variation in the peaks of the doped and undoped samples. The decrease in the intensity of the emission peaks of the doped samples could be attributed to the ordering of oxygen vacancies which is well reported in the perovskite and aurivillius structured materials [53, 55]. The oxygen vacancy distribution becomes more ordered in the lattice instead of random distribution. It is also seen from the Urbach energy results (Fig. 4.18). So, there is a significant increase in the oxygen vacancies and defects with the increase in the Ni^{2+} concentration in the present case. This increase in the defects is essential for the movement of oxygen ions in the lattice for conduction. However, ordering restricts the movement of ions which might lower the conduction

phenomenon. The vacancies might follow an order in the lattice, leading to a decrease in the intensity of the emission peaks. Quenching of the emission spectra is observed in the case of substituted samples [56]. The quenching phenomenon is due to the excitation energy being transferred between two nearest neighbouring Ni^{2+} ions. This transfer occurs through multiple non-radiative transitions. After these transitions, the excitation energy reaches the defect states. The quenching phenomenon is due to concentration quenching [56, 57]. Another possibility could be the reduction of Zr^{4+} in the presence of $Ni^{2+,}$ which led to an increase in the oxygen vacancies in the doped systems. However, the Urbach energy did not support this possibility in the present samples since Ni^{2+} or, broadly, transition elements, when substituted into self-luminescent materials, act as killers of luminescence [58].

As mentioned in Section 4.2.6, due to the sintered pellets' cracks, the conductivity measurements could not be performed on the Ni-doped $SrZrO_3$. However, to get an idea about the nature of Ni-doped samples, the variation of defects and their types were evaluated by optical band gap and PL measurement. In comparison with Cu-doped $SrZrO_3$ samples, the Ni-doped $SrZrO_3$ perovskites are more brittle. In other words, the covalent bond characteristic increases with Ni-dopant concentration. It seems that overall conductivity might be less than Cu-doped samples. PL shows the presence of different types of defects and their quenching at higher concentrations.

Summary

Undoped and doped $SrZrO_3$ are single-phase systems. The dopants increase the grain refinement with increasing density. CTE is observed in the required range of SOFC, i.e. 9-14×10^{-6} $°C^{-1}$ in the temperature range of 200-1000°C. The conductivity of Cu-doped $SrZrO_3$ increases from 10^{-7} Scm^{-1} to 10^{-4} Scm^{-1} with increasing dopant concentration. Ni-doped $SrZrO_3$ exhibits cracks in the sintered samples due to phase transition during processing.

References

[1] N.F. Muhamad, R.A.M. Osman, M.S. Idris. M.N.M. Yasin, EPJ Web of Conferences 162 (2017) 01052(1)-(4).

[2] Z. Feng, H. Hu, S. Cui, C. Bai, Solid State Commun. 148 (2008) 472-475.

[3] K. Sood, K. Singh, S. Basu, O.P. Pandey, Ionics 21(10) (2015) 2839-2850.

[4] V.M. Goldschmidt, Naturwissenschaften 14(21) (1926) 477-485.

[5] R.D. Shannon, Acta Cryst. A32 (1976) 751-767.

[6] A. Slodczyk, M. Limage, P. Colomban, O. Zaafrani, F. Grasset, J. Loricourt, B. Sala, J. Raman Spectrosc. 42 (2011) 2089-2099.

[7] S. Omar, J.C. Nino, Acta Mater. 61 (2013) 5406-5413.

[8] V.K. Kaushik, Spectrochim. Acta 44(6) (1989) 581-587.

[9] P.J. Gellings, H.J.M. Bouwmeester, CRC Press, Boca Raton (USA), 1997.

[10] S. Thakur, M. Devi, K. Singh, Ionics 20 (2014) 73-81.

[11] S. Thakur, O.P. Pandey, K. Singh, J. Mol. Struct. 1074 (2014) 186-192.

[12] V. Prakash, R.K. Diwan, U.K. Niyogi, Indian J. Pure Appl. Phys. 53 (2015) 753-758.

[13] L. Zhang, J. Wang, D. Peng, F. Long, S. Mo, Y. Wu, Z. Zou, J. Phys. Chem. Solids 104 (2017) 1-7.

[14] Y.S. Malghe, U.C Yadav, J. Therm. Anal. Calorim. 122 (2015) 589-594.

[15] C. Ostos, L. Mestres, M.L. Martínez-Sarrión, J.E. García, A. Albareda, R. Perez, Solid State Sci. 11 (2009) 1016-1022.

[16] S. Parida, SK. Rout, V. Subramanian, P.K. Barhai, N. Gupta, V.R. Gupta, J. Alloys Compd. 528 (2012) 126-134.

[17] J. Chandradas, K.H. Kim, J. Alloys Compd. 481 (2009) L31-L34.

[18] A. Wokaun, B. Schrader, VCN, Weinheim (Germany), 1995.

[19] P.P. Khirade, A.B. Shinde, A.V. Raut, S.D. Birajdar, K.M. Jadhav, Ferroelectrics 504(1) (2016) 216-229.

[20] D. Hassan, S. Janes, R. Clasen, J. Eur. Ceram. Soc. 23 (2003) 221-228.

[21] I. Kashif, A. Ratep, Appl. Phys. A 120(4) (2015) 1427-1434.

[22] T.A.G. Restivo, S.R.H. Mello-Castanho, Int. J. Mat. Res. 101 (2010) 128-132.

[23] K. Sood, K. Singh, O.P. Pandey, J. Mater. Sci. 47 (2012) 4520-4529.

[24] S. Thakur, O.P. Pandey, K. Singh, Particul. Sci. Technol. 33 (2015) 178-183.

[25] A. Ahtee, M. Ahtee, A.M. Glazer, A.W. Hewat, Acta Cryst. B32 (1976) 3243-3246.

[26] B.J. Kennedy, C.J. Howard, B.C. Chakoumakos, Phys. Rev. B 59(6) (1999) 4023-4027.

[27] L. Carlsson, Acta Cryst. 23 (1967) 901-905.

[28] S. Thakur, O.P. Pandey, K. Singh, Particul. Sci. Technol. 33 (2015) 178-183.

[29] J.C. Boivin, G. Mairesse, Chem. Mater. 10 (1998) 2870-2888.

[30] J.E. Shelby, Second ed., Royal Society of Chemistry, Cambridge (UK) 2005.

[31] S. Thakur, O.P. Pandey, K. Singh, Ceram. Int. 40 (2014) 16371-16379.

[32] K. Sood, K. Singh, S. Basu, O.P. Pandey, J. Eur. Ceram. Soc. 36(13) (2016) 3165-3171.

[33] H. Borkar, A. Barvat, P. Pal, A.K. Shukla, J.J. Pulikkotil, A. Kumar, J. Appl. Phys. 119 (2016) 214101(1)-(6).

[34] JTS. Irvine, D.C. Sinclair, A.R. West, Adv. Mater. 2(3) (1990) 132-138.

[35] X. Yuan, C. Song, H. Wang, J. Zhang, Springer-Verlag, London (UK), 2010.

[36] B. Tiwari, R.N.P. Choudhary, IEEE Trans. Dielectr. Electr. Insul. 17(1) (2010) 5-17.

[37] S. Misra, Mater. Chem. Phys. 190 (2017) 1-7.

[38] J. Richter, P. Holtappels, T. Graule, L.J. Gauckler, Solid State Ion. 179 (2008) 2284-2289.

[39] G. Kostogloudis, N. Vasilakos, C. Ftikos, Solid State Ion. 106 (1998) 207-218.

[40] A.M. Hussain, K. Pan, Y. Huang, I.A. Robinson, C. Gore, E.D. Wachsman, ACS Appl. Mater. Interfaces 10 (2018) 36075-36081.

[41] S. Omar, E.D. Wachsman, J.C. Nino, Solid State Ion. 177 (2006) 3199-3203.

[42] S. Das, S. Som, C. Yang, S. Chavhan, C. Lu, Sci. Rep. 6 (2016) 25787 (1)-(13).

[43] SD. Meetei, S.D. Singh, J. Alloys Compd. 587 (2014) 143-147.

[44] T. Matsuda, S. Yamanaka, K. Kurosaki, S. Kobayashi, J. Alloys Compd. 351 (2003) 43-46.

[45] D. de Ligny, P. Richet, Phys. Rev. B 53 (6) (1996) 3013-3022.

[46] Y. Zhao, D.J. Weidner, Phys. Chem. Miner. 18 (1991) 294-301.

[47] Q. Liu, Z. Liu, Y. Liu, L. Feng, H. Tian, J. Ding, Solid State Commun. 150 (2010) 2032-2035.

[48] S. Singh, K. Singh, J. Mol. Struct. 1081 (2015) 211-216.

[49] A.A. Saad, W. Khan, P. Dhiman, A.H. Naqvi, M. Singh, Electron. Mater. Lett. 9 (1) (2013) 77-81.

[50] L.S. Cavalcante, J.C. Sczancoski, V.M. Longo, F.S. De Vicente, J.R. Sambrano, A.T. De Figueiredo, C.J. Dalmaschio, M.S. Li, J.A. Varela, E. Longo, Optic. Commun. 281 (2008) 3715-3720.

[51] V.M. Longo, L.S. Cavalcante, R. Erlo, V.R. Mastelaro, A.T. de Figueiredo, J.R. Sambrano, S. De Lazaro, A.Z. Freitas, L. Gomes, N.D. Vieira Jr., J.A. Varela, E. Longo, Acta Mater. 56 (2008) 2191-2202.

[52] R.E. Gonzalez, E. Mosquera, I. Moglia, R. Villarroel, V.M. Fuenzalida, Ceram. Int. 40 (10) (2014) 15577-15584.

[53] G. Madhu, V. Biju, Physica E 60 (2014) 200-205.

[54] E. Mete, R. Shaltaf, S. Ellialtioglu, Phys. Rev. B 68 (2003) 035119 (1)-(4).

[55] I.C. Nogueira, L.S. Cavalcante, P.F.S. Pereira, M.M. Jesus, J.M.R. Mercury, N.C. Batista, M.S. Lid, E. Longo, J. Appl. Crystallogr. 46 (2013) 1434-1446.

[56] G.T. Pott, W.H.J. Stork, Catal. Rev. Sci. Eng. 12 (1) (1975) 163-199.

[57] V. Ramasamy, K. Praba, G. Murugadoss, Spectrochim. Acta A 96 (2012) 963-971.

[58] L. Fabbrizzi, M. Licchelli, P. Pallavicini, D. Sacchi, A. Taglietti, Analyst 121 (1996) 1763-1768.

Overview

The chapter reports the effect of doping Cu and Ni in $SrMnO_3$. The structural, thermal, and conducting properties are analyzed using XRD, FTIR, SEM, TG-DTA, dilatometry, and impedance analyzer. The basis of the study is to observe the changes in the $SrMnO_3$ system based on vacancy formation, phase transitions, homogeneity, etc., on doping lower valence Cu^{2+} and Ni^{2+} in place of Mn^{4+} in $SrMnO_3$. The samples are investigated for use as SOFC cathode materials.

5.1. Undoped and Cu-doped $SrMn_{1-x}Cu_xO_{3-\delta}$ ($0.00 \leq x \leq 0.20$)

Strontium manganite is a perovskite structured material having unique structural properties, as discussed below. The hexagonal and cubic $SrMnO_3$ is semiconducting in nature [1]. The temperature of heat-treatment, heat durations and synthesis procedures affect the formation of cubic $SrMnO_3$. Incorporating lower valence transition metals introduces oxygen vacancies in the system that may enhance the ionic conduction of $SrMnO_3$. Various characterisation techniques are used to analyse the effect of dopants on the structural, thermal, and electrical properties to check these materials' suitability as SOFC cathodes.

5.1.1. XRD analysis

As mentioned in Chapter 3, the undoped and doped samples were prepared via the solid-state reaction method and heat-treated at 1300 and 1250°C, respectively, for 4 hrs. The phase analysis has been done using XRD. The XRD patterns of $SrMn_{1-x}Cu_xO_{3-\delta}$ ($0.00 \leq x \leq 0.20$) are shown in Fig. 5.1 (a). They exhibit highly intense peaks, which indicate the good crystalline nature of the as-prepared samples. The highest intense peak corresponds to the hexagonal $SrMnO_3$; however, with the gradual increase in the Cu-dopant concentration, the hexagonal $SrMnO_3$ changes into orthorhombic $SrMnO_{2.5}$.

The change in the crystal structure of $SrMnO_3$ suggests that an increase in the dopant concentration leads to structural stability. However, this change is also observed with the rise in the heat treatment temperature, as shown in Fig. 5.1 (b). It implies that both dopant and the heat-treatment temperature affect the crystal structure of $SrMnO_3$. The structural changes in $SrMnO_3$ with the temperature rise are well-reported in the literature [2]. The presence of orthorhombic $SrMnO_{2.5}$ suggests an anionic deficiency in $SrMnO_3$ due to the reduction of Mn^{4+} to Mn^{3+} [2].

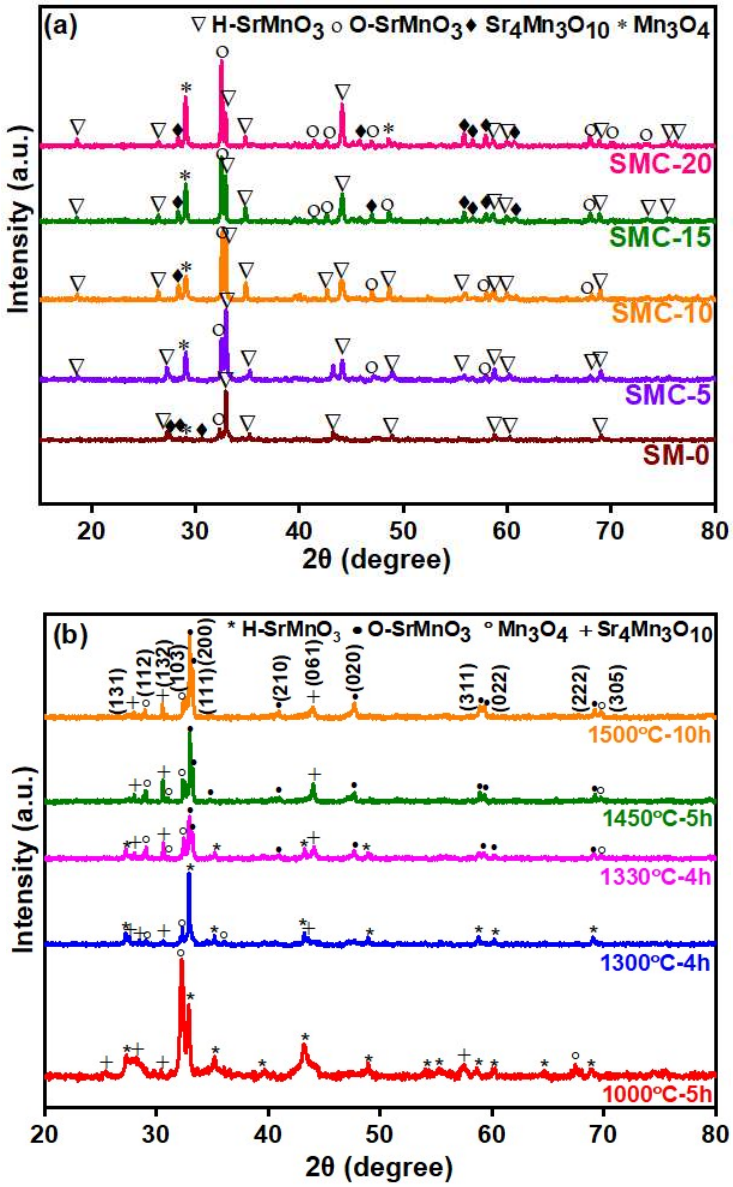


Fig. 5.1 XRD patterns of (a) $SrMn_{1-x}Cu_xO_{3-\delta}$ ($0.00 \leq x \leq 0.20$) and (b) $SrMnO_3$ with respect to different temperatures and time durations

XPS of SM-0 and SMC-10 was carried out to confirm the state of manganese and copper in undoped and doped $SrMnO_3$, and the results are shown in Fig. 5.2 (a-c). A distinction between trivalent and tetravalent manganese can be made from the $2p$ peak positions. The manganese XPS spectra generally have a trivalent state $2p_{3/2}$ positioned below 641 eV while the tetravalent manganese is positioned around 642 eV [3, 4]. From the XPS spectra shown in

Fig. 5.2 (a-c), it is observed that the $2p_{3/2}$ and $2p_{1/2}$ peaks are positioned at 642.5 and 654.2 eV, respectively. It implies that the undoped and doped samples have tetravalent manganese. Also, the difference between the 2p peaks (11.7eV) confirmed that Mn is present in the Mn^{4+} state only [5, 6]. The XPS spectra of copper are shown in Fig. 5.2 (c), where the presence of strong satellite peaks confirms the presence of Cu^{2+} state [7, 8].

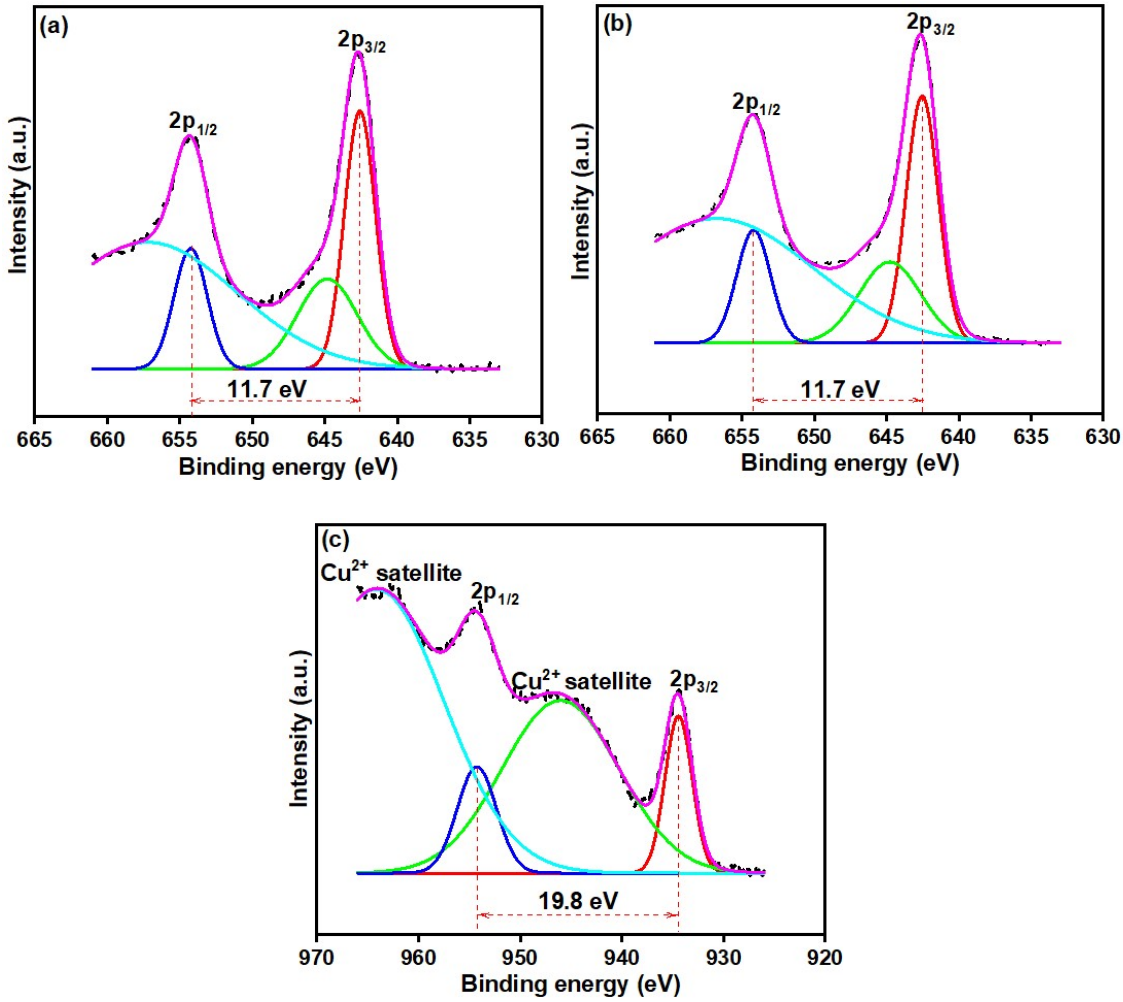


Fig. 5.2 XPS spectra of (a) Mn^{4+} in SM-0, (b) Mn^{4+} in SMC-10 and (c) Cu^{2+} in SMC-10

Apart from this, secondary phases are also formed, namely, Hausmannite (Mn_3O_4) and Ruddlesden-Popper ($Sr_4Mn_3O_{10}$). The volume fraction of the Mn_3O_4 phase increases with the dopant concentration; however, the volume fraction of $Sr_4Mn_3O_{10}$ decreases gradually, as shown in Fig. 5.3. The gradual increase in Mn_3O_4 compared with $Sr_4Mn_3O_{10}$ implies that Mn^{4+} is converted into Mn^{3+}/Mn^{2+} oxidation states in the presence of Cu dopant. However,

the XPS results suggest otherwise. The presence of Mn_3O_4 during the synthesis of $SrMnO_3$ has been reported in the literature; however, the formation of $Sr_4Mn_3O_{10}$ is reported rarely [9].

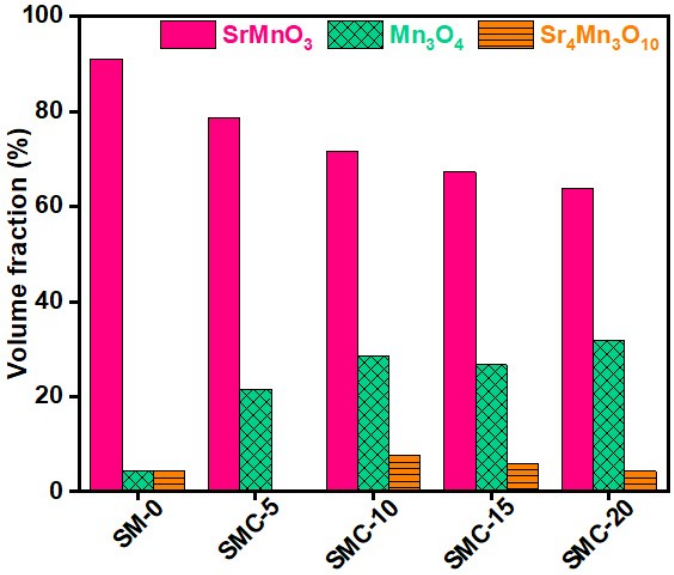


Fig. 5.3 Variation in the volume fraction of the different crystalline phases with an increasing dopant concentration of Cu in $SrMnO_3$

Based on the ionic radii difference of the host and dopant cation, the doping of Cu is expected to take place at the Mn-site of $SrMnO_3$ [10]. Due to the doping of a larger ionic radii Cu^{2+} (0.073 nm) in place of a smaller Mn^{4+} (0.053 nm), the XRD peaks shift towards lower diffraction angles, as shown in Fig. 5.4. Even if manganese is present in +2 and +3 state their ionic radii (Appendix) is much smaller than Cu^{2+}. Therefore, the XRD peak shifting towards lower angles is justified. Lower diffraction angle shifting suggests an increase in the d-space between the different planes, corresponding to the tensile strain in the lattice of $SrMnO_3$. This shifting could also be due to the change in the crystal structure of $SrMnO_3$ from hexagonal to orthorhombic. Also, the secondary phases present in the system could lead to the shifting of XRD peaks.

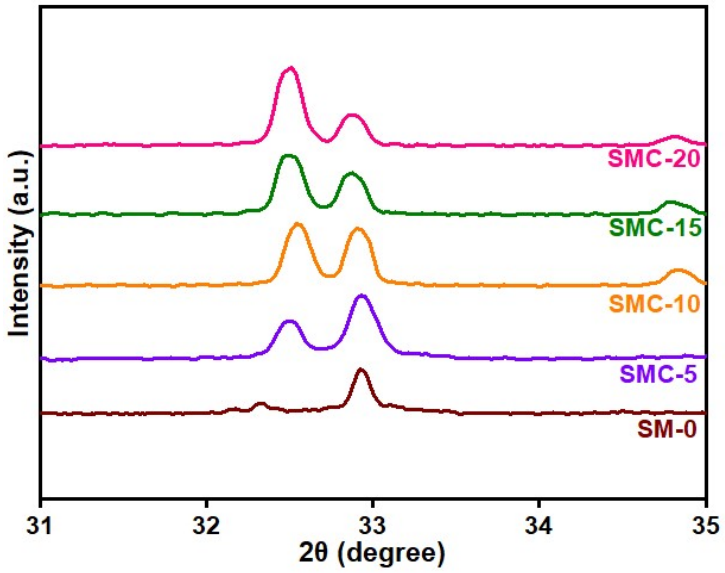


Fig. 5.4 Slight shifting of the highest intense peak of $SrMn_{1-x}Cu_xO_{3-\delta}$ ($0.00 \leq x \leq 0.20$) towards lower diffraction angles signifies the effective doping of higher ionic radii dopant in place of a lower ionic radii host

Table 5.1 lists the FWHM and the mean crystallite size of $SrMn_{1-x}Cu_xO_{3-\delta}$ ($0.00 \leq x \leq 0.20$). The sudden increase in the FWHM (SMC-5) could be due to the introduction of copper in $SrMnO_3$. Also, the presence of minor phases could be the possible reason for the broadening. According to the Scherrer formula (equation 3.2), the FWHM is inversely proportional to the crystallite size. In the present case, the FWHM follows the rule mentioned above. However, no particular trend due to the presence of secondary phases is observed in the samples.

Table 5.1 FWHM and mean crystallite size of $SrMn_{1-x}Cu_xOO_{3-\delta}$ ($0.00 \leq x \leq 0.20$)

Parameters	**SM-0**	**SMC-5**	**SMC-10**	**SMC-15**	**SMC-20**
FWHM (°)	0.128	0.176	0.147	0.151	0.145
Crystallite size (nm)	66.00	46.99	59.00	55.52	59.00

The decreased crystallite size of SMC-5 denotes structural disorder in the system. It is due to the doping of larger radii Cu^{2+} in place of a smaller $Mn^{4+,}$ which delays crystallite growth. However, increasing dopant concentration increases the crystallite size, thereby narrowing

the XRD peaks. The narrowing of the peaks can also be associated with the shift in the crystal structure of $SrMnO_3$ from hexagonal to the orthorhombic structure.

5.1.2. FTIR analysis

Fig. 5.5 (a, b) shows the FTIR spectra of the undoped and Cu-doped $SrMnO_3$. Five significant bands are observed at ~441, 544, 632, 1463 and 1630 cm^{-1}. The strong bands observed at 544 and 632 cm^{-1} are due to the stretching vibration of the Mn-O bond lengths, justifying the presence of Mn in MnO_2. The presence of Mn-O bonds is essential since they affect the BO_6 octahedra of the $SrMnO_3$ perovskite. This peak is attributed to the Mn-O vibrations of the MnO_6 octahedra. A similar peak has also been reported in the MnO_2 crystals [11-14]. Broadening of the band, ~544 cm^{-1}, signifies disorder in the undoped sample. It could be due to the heat-treatment, inhomogeneity or presence of strain in the sample. Also, the shifting of the ~544 and 632 cm^{-1} bands towards lower wavenumbers suggests some slight structural modifications with Cu^{2+} doping since the bond strength of Cu-O is weaker than Mn-O bonds.

Moreover, the lower valence dopant Cu^{2+} replaces the Mn^{4+} in the $SrMnO_3$ system, leading to the creation of oxygen vacancies in the system. The creation of vacancies could also be the reason for shifting the bands towards lower wavenumbers, i.e. lower energy side. The slight dip in the FTIR spectra of the doped and the undoped samples at ~1463 and ~1630 cm^{-1} corresponds to the presence of CO_2 and OH bands in the spectra. The CO_2 might be due to the reaction of the samples with CO_2 present in the environment.

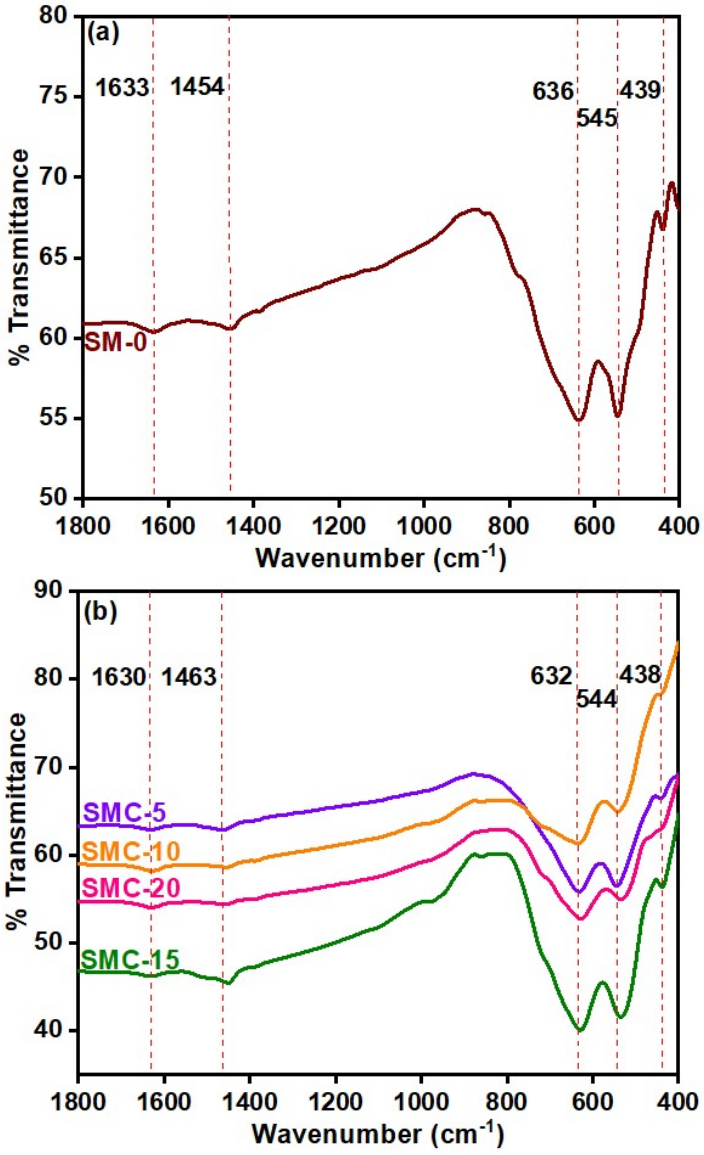


Fig. 5.5 FTIR spectra of (a) $SrMnO_3$ and (b) $SrMn_{1-x}Cu_xO_{3-\delta}$ ($0.05 \leq x \leq 0.20$)

5.1.3. Physical parameters

Table 5.2 lists the physical parameters such as relative density, molar volume, concentration, polaron radius and the distance between dopant ions. Additionally, the hardness of the samples is also given in Table 5.2. Doping increases the densification of $SrMnO_3$. An increase in the copper concentration leads to a significant increase in the density of the samples. The higher density of CuO (6.31 gcm^{-3}) compared with MnO_2 (5.03 gcm^{-3}) can be attributed to this increase. As seen in Table 5.2, the increase in the dopant concentration leads to an increase in the hardness of the sample. The hardness of the doped samples is

comparable to the literature [9]. The molar volume of the samples follows the expected results. Since CuO (79.545 $gmol^{-1}$) has a lesser molar mass than MnO_2 (86.936 $gmol^{-1}$); therefore, there is a decrease in the values of the molar volume. The decrease in the concentration of ions per unit volume leads to an increase in the distance between the Cu^{2+} ions. Since the polaron radius of all the samples is smaller than R but higher than the ionic radii of Cu^{2+}, it is inferred that the electrons in the system are localised [15].

Table 5.2 Density, hardness, molar volume, concentration, polaron radius and the distance between Cu^{2+} ions of $SrMn_{1-x}Cu_xO_{3-\delta}$ ($0.00 \leq x \leq 0.20$)

Sample label	ρ (g cm^{-3})	Hardness (GPa)	V_m (cm^3 $mole^{-1}$)	N ($\times 10^{22}$ cm^{-3})	r_p ($\times 10^{-8}$ cm)	R ($\times 10^{-8}$ cm)
SM-0	3.01	0.71	31.16	-	-	-
SMC-5	3.40	1.03	27.55	4.90	1.01	2.73
SMC-10	4.03	5.88	23.19	2.90	1.31	3.25
SMC-15	4.27	3.87	21.89	2.04	1.47	3.66
SMC-20	4.24	3.02	22.01	1.51	1.63	4.04

5.1.4. Microstructural analysis

The SEM micrographs of the undoped and Cu-doped $SrMnO_3$ are shown in Fig. 5.6 (a-e). The increasing dopant concentration leads to a change in the shape as well size of the grains. The SEM micrograph of the undoped $SrMnO_3$ has compact, non-uniformly distributed unevenly shaped grains with some pores. On the other hand, Cu-doped $SrMnO_3$ exhibits a range of microstructural features with randomly distributed non-uniform grains with increasing grain size. Generally, grain growth occurs in two ways, i.e. normally and abnormally, depending on the diffusion. Many conditions like the size of the ions, concentration, temperature etc., influence it [16]. Normal grain growth refers to the uniform growth of the grains, while abnormal grain growth refers to the rapid increase in the grain sizes of some of the grains leading to a difference in the grain sizes. From the grain size

values listed in Table 5.3, it is clear that the grain growth is abnormal with a gradual increase in the size of the grains.

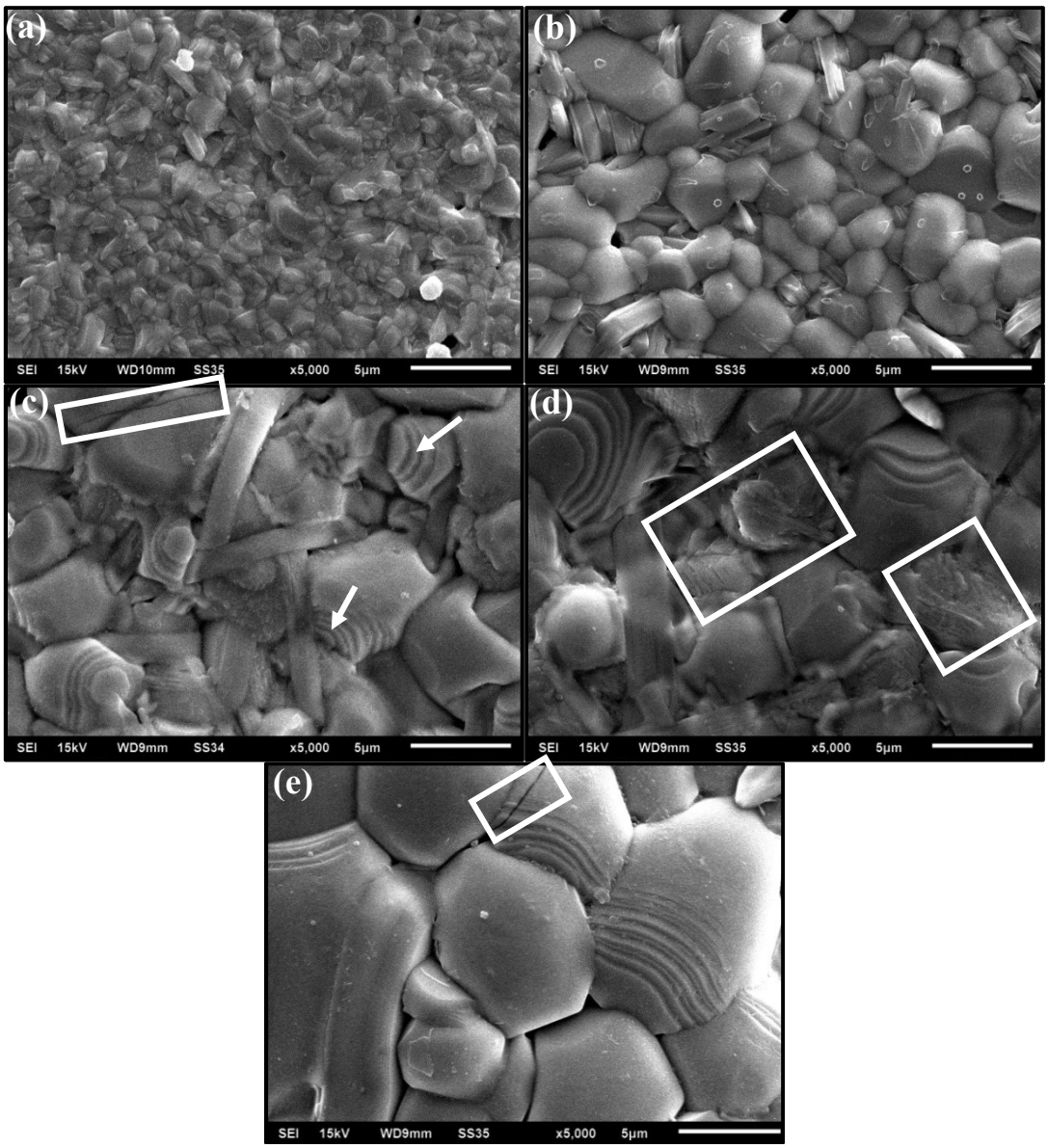


Fig. 5.6 SEM micrographs of (a) SM-0, (b) SMC-5, (c) SMC-10, (d) SMC-15 and (e) SMC-20

The arrows in Fig. 5.6 (c) point towards distinct stepped surface patterns. Similar patterns have been observed previously for other perovskite-structured ceramics; however, they are seldom reported for $SrMnO_3$ [17-19]. These patterns arise either due to grain spiral growth or two-dimensional nucleation. In the present case, this phenomenon could be due to the two-

dimensional nucleation since it requires melting the sample to provide a supersaturation level for the two-dimensional crystal growth [20]. The boxes in Fig. 5.6 (d) show distorted grains due to the partial melting of CuO. It is well reported in the literature that CuO is known to refine the microstructure [21]. Also seen from the density of the samples (Fig. 5.7), CuO increases the sinterability of $SrMnO_3$ by exhibiting partial liquid phase sintering in the doped samples similar to the case of Cu-doped $SrZrO_3$ (Section 4.1.4, Chapter 4). Also, in this case, the density is lower than Cu-doped $SrZrO_3$, which could be due to the porosity of the samples.

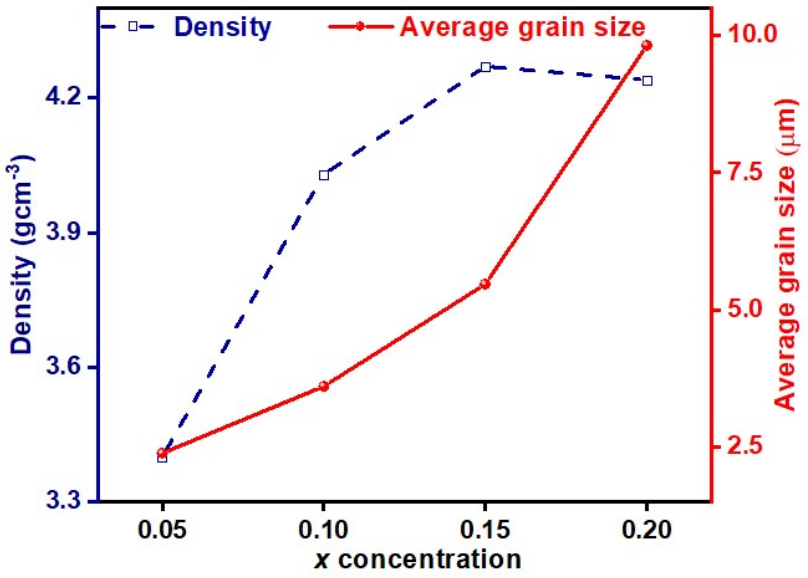


Fig. 5.7 Variation in the density and average grain size of Cu-doped $SrMnO_3$ with increasing dopant concentration

The inset boxes in Fig. 5.6 (c) and (e) represents another striking feature. The formation of a crack could be attributed to the presence of inherent strain in the sample probably created by the dopant. It correlates with the XRD of the samples since the presence of tensile strain might be responsible for such cracks in the sintered samples. The elemental variation of the different elements of the composition is given in Table 5.3. It is observed that the concentration of Cu increases gradually with a slight decrease in the SMC-15 sample. This

decrease might be due to the liquid phase sintering of this particular sample. However, the required stoichiometry is maintained even after heat treatment.

Table 5.3 Weight % of the different elements of the composition $SrMn_{1-x}Cu_xO_{3-\delta}$ ($0.00 \leq x \leq 0.20$)

Sample Id	Average grain size (µm)	Sr	Mn	Cu	O
		wt%			
SM-0	1.22	51.39	30.38	-	18.23
SMC-5	2.39	52.28	23.61	6.14	17.97
SMC-10	3.61	50.15	24.09	7.65	18.10
SMC-15	5.47	51.52	26.05	4.34	18.09
SMC-20	9.82	49.80	23.25	8.86	18.09

5.1.5. TG-DTA analysis

Fig. 5.8 (a, b) shows the representative TG-DTA curves of the SM-0, SMC-10 and SMC-20 up to 1000°C. From the TGA curves of the samples, it is evident that the samples undergo weight loss on heating up to 1000°C. Contrary to Cu-doped $SrZrO_3$, where the weight loss was drastic here, the weight is rather continuous. The doped samples show a weight loss ~200-400°C, attributed to the loss of moisture from the system and the relaxation processes occurring within the system from the samples [14, 22]. The plateau region between 400-800°C can be attributed to the rearrangement of the internal structure of $SrMnO_3$. It can also be correlated to the shifting of the XRD peaks towards lower diffraction angles due to the presence of tensile strain in the samples.

In the DTA curves showed in Fig. 5.8 (b), not much change was observed in the samples up to 1000°C. It suggests that the samples are stable up to 1000°C and is consistent with the literature since the phase transitions in $SrMnO_3$ occur beyond 1035°C [2].

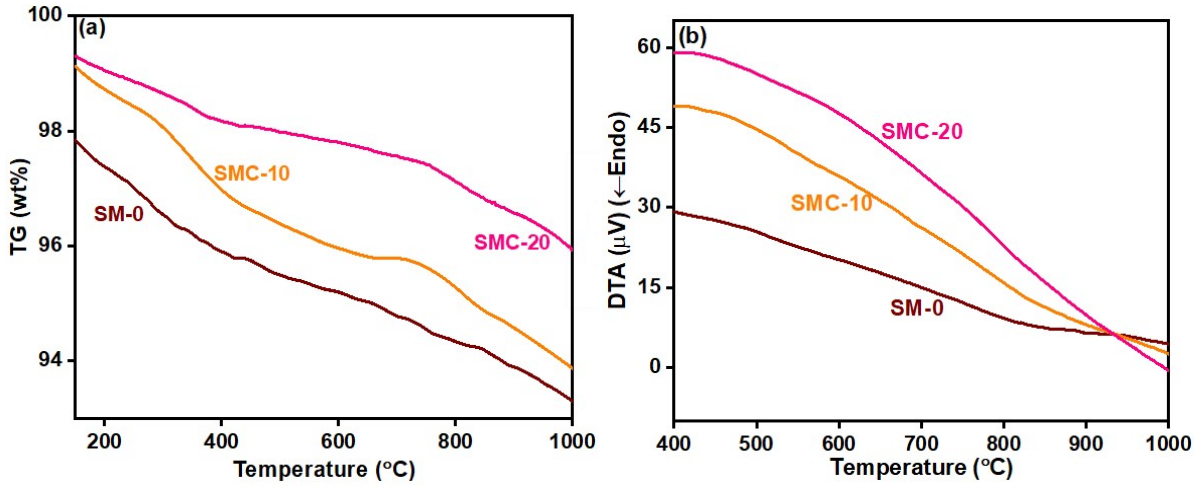


Fig. 5.8 Representative (a) TG plots and (b) DTA curves of $SrMn_{1-x}Cu_xO_{3-\delta}$ (x=0.00, 0.10, 0.20)

5.1.6. Thermal expansion analysis

Fig. 5.9 shows all the samples' thermal expansion curves indicating linear expansion with temperature with a slight difference in their slopes. The CTE of SM-0, SMC-5, SMC-10, SMC-15 and SMC-20 are 9.52, 10.34, 9.53, 10.19 and 9.0×10^{-6} $°C^{-1}$, respectively, in the temperature range of 200-1000°C. The doped samples have a slightly higher CTE than the undoped sample, which might be due to the presence of oxygen vacancies in the system generated on the doping of Cu^{2+} in place of Mn^{4+} in $SrMnO_3$. It is a well-known fact that the missing oxygen from the lattice lowers the interatomic bond strength and increases the CTE.

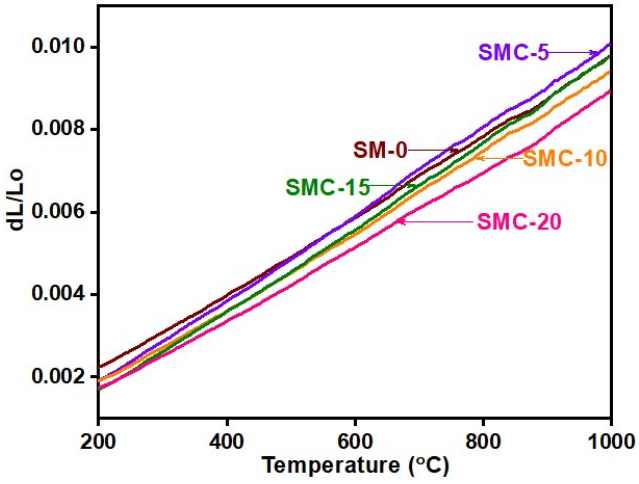


Fig. 5.9 Thermal expansion curves of $SrMn_{1-x}Cu_xO_{3-\delta}$ ($0.00\leq x\leq0.20$)

The results are in accordance with the FTIR analysis results since the shifting of the bands towards the lower wavenumber suggests a decrease in the bond strength [23, 24]. It is also supported by the difference in the field strength (F) of the cations mentioned in the Appendix. The field strength of Cu^{2+} is less than Mn^{4+}, which implies that the bond strength decreases with copper substitution. However, with the increase in the dopant concentration, there is a slight decrease in the CTE of the doped samples. The higher electro-negativity of Cu^{2+} compared with Mn^{4+} justifies the decrease in the CTE [25]. Although the CTE varies between $9\text{-}10\times10^{-6}$°C^{-1}, this decrease might result from ordering the oxygen vacancies [26, 27]. The CTE results are comparable with Ce-doped $SrMnO_3$ as well as Cu-doped $SrZrO_3$ [28]. Overall, the CTE values of the doped and undoped samples are within the tolerance limit of SOFC, making them suitable for use as cathode materials.

5.1.6. Conductivity analysis

Impedance spectroscopy was employed to observe the effect of doping on the conductivity of $SrMn_{1-x}Cu_xO_{3-\delta}$ ($0.00\leq x\leq0.20$). Fig. 5.10 (a, b) show the Nyquist plots of $SrMn_{1-x}Cu_xO_{3-\delta}$ ($0.00\leq x\leq0.20$) at room temperature and the equivalent circuit corresponding to SMC-20. The capacitance of SMC-20 is of the order of 10^{-9} F, which implies that the effect of grain boundaries is prominent in the conduction phenomenon of Cu-doped $SrMnO_3$ [29]. Well-defined single semi-circular curves are observed; however, as the dopant concentration increases, slight depression is observed in the Nyquist curves. As in the Cu-doped $SrZrO_3$ samples (Section 4.1.7, Chapter 4), the depressed Nyquist plots could be due to various reasons [30-32].

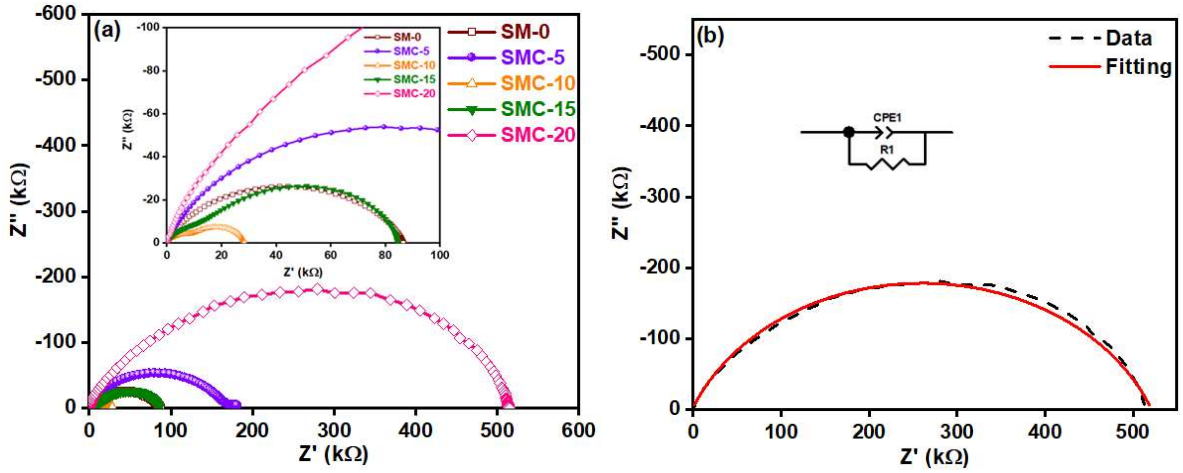


Fig. 5.10 (a) Room-temperature Nyquist plots of $SrMn_{1-x}Cu_xO_{3-\delta}$ ($0.00 \leq x \leq 0.20$) with the inset showing the magnified exhibiting the distortion of the semi-circle and (b) fitted SMC-20 with the equivalent circuit

However, the presence of semi-circular Nyquist plots is observed only at room temperature. There is a distortion observed at higher temperatures (>600°C). In the present case, several processes affect the conductivity of the system. The first is the electron transfer between the ions of multiple oxidation states of the transition metals (Mn and Cu), which account for the electronic conduction. The second could be doping a lower valence cation (Cu^{2+}) in place of a higher valence host cation (Mn^{4+}), creating oxygen vacancies in the system necessary for ionic transport. Apart from this, temperature also plays a vital role in enhancing the ionic conductivity of the system. Since ions are heavier than electrons, therefore, increasing thermal motion leads to an increased ion movement.

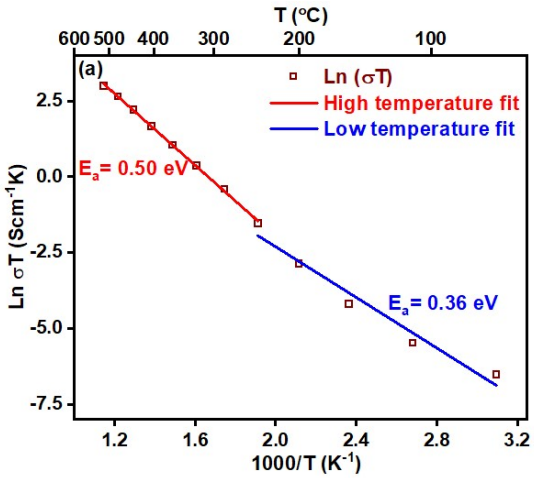
From the conductivity values listed in Table 5.4, it is observed that the conductivity of the samples increases with the increase in the temperature exhibiting the semiconducting nature of the samples. Doping, on the other hand, is expected to increase the conduction phenomenon. However, in the present case, doping does not change the order of conductivity somewhat decreases at higher concentrations of copper, i.e. SMC-20. Based on stoichiometry, the doping of copper is expected to increase the conductivity of $SrMnO_3$.

However, the change in the oxidation states of manganese and the presence of multi phases, as mentioned in Section 5.1.5, could be the reason for the decrease in conductivity in the doped samples. The number of vacancies that would have been generated on doping Cu^{2+} in place of Mn^{4+} is reduced due to the change in the oxidation states of manganese from Mn^{4+} to $Mn^{2+/3+}$. Also, the merging of the semi-circles in the Nyquist plots suggests the influence of grain boundaries is more on the conductivity than the grains. It is confirmed by the increasing average grain size of the samples in the SEM micrographs. Therefore, it can be concluded that the electronic conduction increases at the cost of ionic conduction.

Table 5.4 Total conductivity (σ) of $SrMn_{1-x}Cu_xO_{3-\delta}$ ($0.00 \leq x \leq 0.20$)

Sample	σ (Scm^{-1})			
	RT	200°C	400°C	600°C
SM-0	2.83×10^{-6}	1.20×10^{-4}	4.27×10^{-3}	2.32×10^{-2}
SMC-5	1.30×10^{-6}	6.82×10^{-5}	2.39×10^{-3}	1.64×10^{-2}
SMC-10	7.83×10^{-6}	3.80×10^{-4}	1.00×10^{-2}	4.20×10^{-2}
SMC-15	2.67×10^{-6}	1.27×10^{-4}	5.74×10^{-3}	2.86×10^{-2}
SMC-20	4.48×10^{-7}	1.82×10^{-5}	9.14×10^{-4}	7.49×10^{-3}

The activation energy of the system is calculated from the slopes of Arrhenius plots shown in Fig. 5.11 (a-c) [33, 34]. Two slopes are observed in the Arrhenius plots, which might be due to the change in the charge carriers.



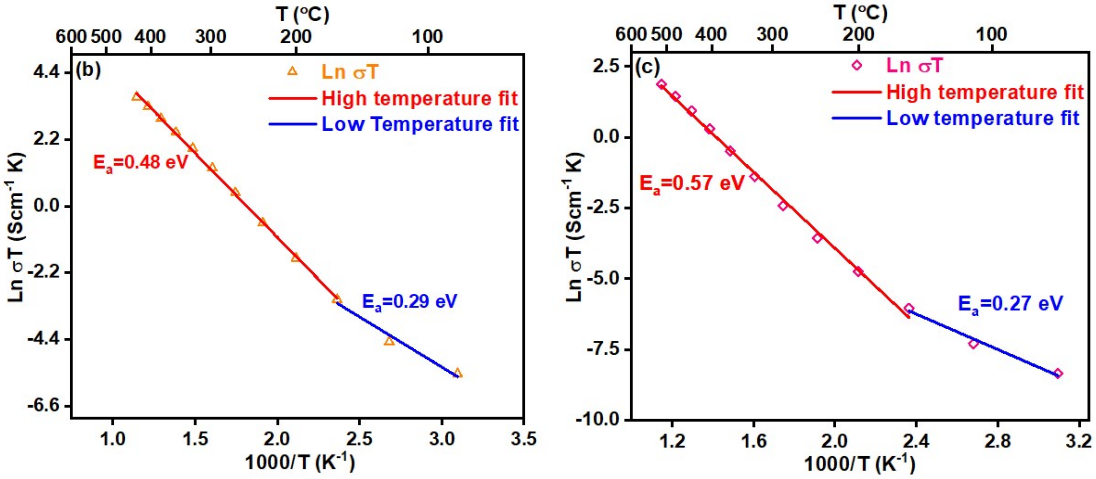


Fig. 5.11 Representative Arrhenius plots of (a) SM-0, (b) SMC-10 and (c) SMC-20

The E_a values listed in Table 5.5 show that the samples have higher activation energies in the high-temperature region. High activation energy is generally expected where the conduction process is carried out by carriers requiring high energy to cross the potential barrier [35]. In the present case, the conduction is thermally activated since there is not much change in the activation energy at low temperatures. As discussed earlier, doping creates vacancies in the system; however, limited oxygen vacancies are created due to the change of Mn^{4+} to $Mn^{2+/3+}$. Furthermore, the oxygen vacancies might be ordered, leading to the lowering of the system's conductivity. Overall, the effect of electronic conduction is due to the reduction of Mn^{4+} to $Mn^{2+/3+}$ and doping of Cu^{2+} while the ionic conduction is thermally activated.

Table 5.5 Activation energy (E_a) of $SrMn_{1-x}Cu_xO_{3-\delta}$ ($0.00 \leq x \leq 0.20$)

Sample label	E_a (eV)	Temperature range (°C)
SM-0	0.36	50-250
	0.50	300-600
SMC-5	0.29	50-150
	0.54	200-600
SMC-10	0.29	50-150
	0.48	200-600
SMC-15	0.28	50-150
	0.53	200-600
SMC-20	0.27	50-150
	0.57	200-600

5.2. Undoped and Ni-doped $SrMn_{1-x}Ni_xO_{3-\delta}$ ($0.00 \leq x \leq 0.20$)

In this section, similar to copper doping, nickel is doped in $SrMnO_3$. The doped samples have been characterised using different techniques to study their structural, thermal and conducting properties.

5.2.1. XRD analysis

Fig. 5.12 shows the XRD patterns of $SrMn_{1-x}Ni_xO_{3-\delta}$ ($0.00 \leq x \leq 0.20$), indicating the good crystalline nature of these samples. The XRD patterns of Ni-doped samples are similar to that of Cu-doped $SrMnO_3$. The XRD patterns reveal the presence of three phases, namely hexagonal and orthorhombic $SrMnO_3$ (ICDD: 01-084-1612, 00-024-1220), $Sr_4Mn_3O_{10}$ (ICDD: 01-086-0650) and Mn_3O_4 (ICDD: 01-075-1560). Similar to the case of Cu-doped samples, the highest intense peak of Ni-doped $SrMnO_3$ also corresponds to the hexagonal $SrMnO_3$.

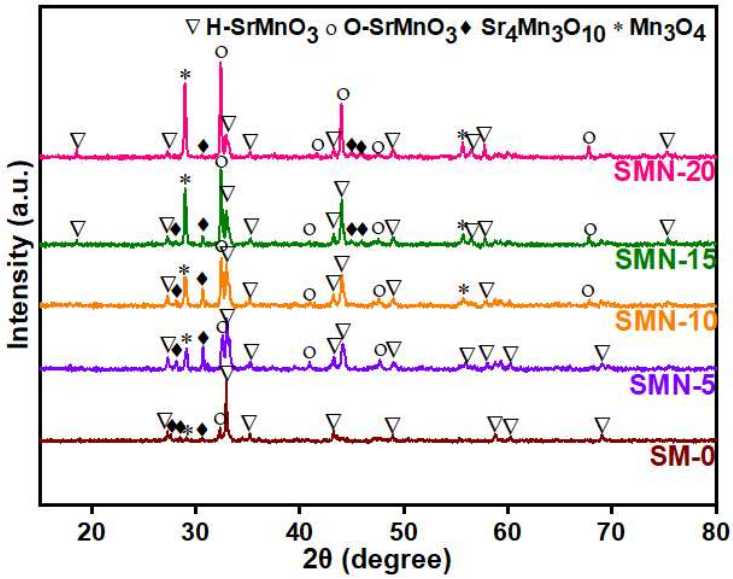


Fig. 5.12 XRD patterns of $SrMn_{1-x}Ni_xO_{3-\delta}$ ($0.00 \leq x \leq 0.20$) showing the presence of secondary phases

With the increase in the dopant concentration, the hexagonal $SrMnO_3$ changes to orthorhombic $SrMnO_{2.5}$ signifying anionic deficiency in the system. The change in the crystal

structure of $SrMnO_3$ suggests that an increase in the dopant concentration leading to the structural stability of the system. As observed from the XPS spectra of the SM-0 and SMN-10 in Fig. 5.13 (a-c), Mn is present in $SrMnO_3$ only in the +4 state. The $2p\,^3/_2$ and $2p\,^1/_2$ peaks of Ni positioned at 855.5 and 873.1 eV confirm the presence of the +2 state of Ni [36]. The XRD analysis of the Ni-doped samples is in line with the Cu-doped samples. It implies that doping of Ni has the same effect as Cu on the secondary phase formations and the oxidation state of the $SrMnO_3$.

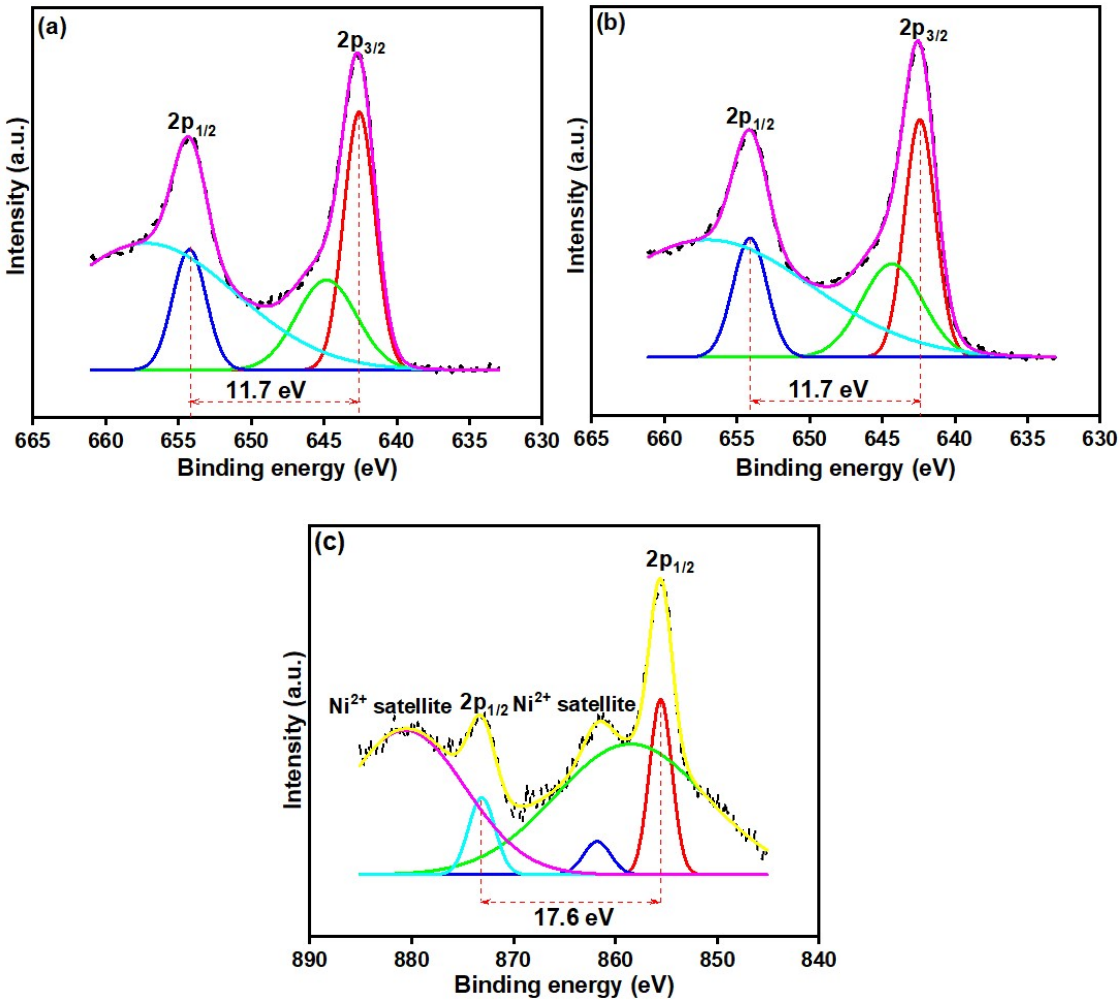


Fig. 5.13 XPS spectra of (a) Mn^{4+} in SM-0, (b) Mn^{4+} in SMN-10 and (c) Ni^{2+} in SMN-10

From the volume fraction of the different phases shown in Fig. 5.14, it is observed that the increase in the dopant concentration leads to an increase in the amount of Mn_3O_4 at the cost

of $Sr_4Mn_3O_{10}$. The presence of Mn_3O_4 suggests manganese to be in $Mn^{2+/3+}$ state; however, the XPS results reveal the manganese to be in a +4 state.

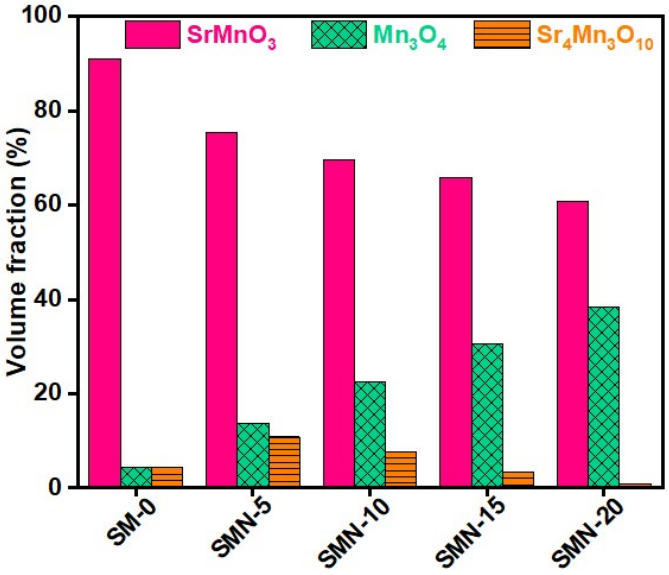


Fig. 5.14 Variation in the volume fraction of the different crystalline phases with an increasing dopant concentration of Ni in $SrMnO_3$

The doping is expected to occur at the Mn-site in $SrMnO_3$ due to the comparable ionic radii of Ni^{2+} (0.069 nm) with Mn^{4+} (0.054 nm), nickel being larger in radii than $Mn^{2+/3+/4+}$ shifts the XRD peaks towards lower angles, as observed in Fig. 5.15. The presence of tensile strain in $SrMnO_3$ is evident in the Ni-doped samples also. Also, the secondary phases present in the system could lead to the shifting of XRD peaks.

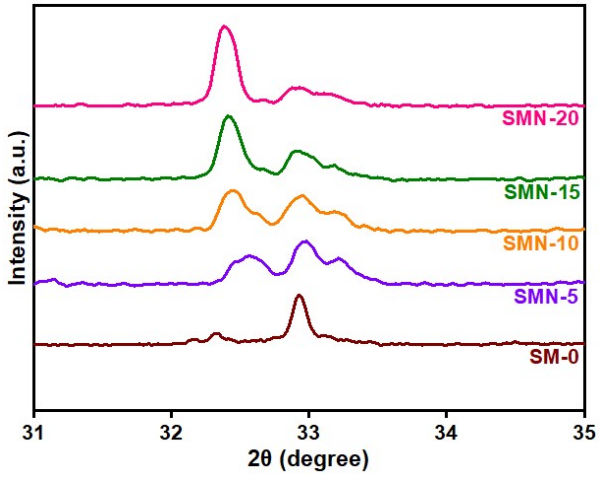


Fig. 5.15 Shifting of the highest intense peak of $SrMn_{1-x}Ni_xO_{3-\delta}$ ($0.00 \leq x \leq 0.20$)

Table 5.6 lists the FWHM and the crystallite size of $SrMn_{1-x}Ni_xO_{3-\delta}$ ($0.00 \leq x \leq 0.20$). Since the ionic radii of the Ni^{2+} dopant are larger than the host, it has the same effect in broadening the peaks and corresponding crystallite size as Cu-doped samples.

Table 5.6 FWHM and mean crystallite size of $SrMn_{1-x}Ni_xO_{3-\delta}$ ($0.00 \leq x \leq 0.20$)

Parameters	SM-0	SMN-5	SMN-10	SMN-15	SMN-20
FWHM (°)	0.128	0.290	0.283	0.250	0.260
Crystallite size (nm)	66.00	32.46	33.76	37.82	40.05

The crystallite size and the FWHM show the opposite trend as per the formula (equation 3.2). The crystallite size in the Ni-doped samples is smaller than the undoped $SrMnO_3$ as well as Cu-doped $SrMnO_3$. However, contrary to the Cu-doped samples, the broadening of the doped samples decreases with increasing dopant concentration indicating better crystallinity of the Ni-doped samples.

5.2.2. FTIR analysis

Fig. 5.16 (a, b) show the FTIR spectra of the undoped and Ni-doped $SrMnO_3$. Five major bands ~441, 544, 632, 1463 and 1630 cm^{-1} are observed. Slight shifting of the FTIR band positions is observed in the undoped and doped samples can be attributed to the change in the bond lengths and the presence of oxygen vacancies. The bands ~441, 544 and 632 cm^{-1} belong to the Mn-O stretching [13, 37, 38].

The shifting of these bands towards lower wavenumber on doping is due to the long bond length of Ni-O than Mn-O. Also, the oxygen vacancies created on doping Ni^{2+} in place of Mn^{4+} are the possible cause of the shifting. The bands ~1447 and 1637 cm^{-1} belong to CO_2 and OH groups, thus confirming moisture content in the samples. The broadening of the bands is associated with the variation in the microstructure due to the processing parameters, multiphase nature of the samples and the presence of strain in the undoped and doped samples. It is in correlation with the XRD results.

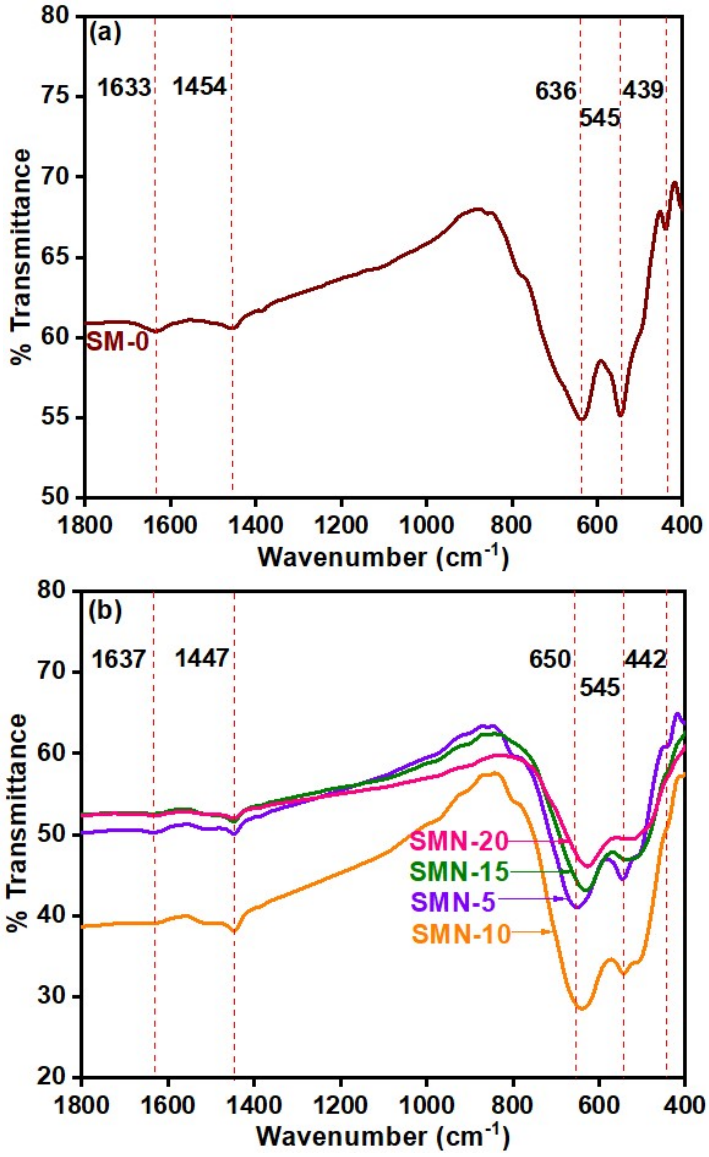


Fig. 5.16 FTIR spectra of (a) $SrMnO_3$ and (b) $SrMn_{1-x}Ni_xO_{3-\delta}$ ($0.05 \leq x \leq 0.20$)

5.2.3. Physical parameters

To better understand the microstructural features of the system, it is, therefore, necessary to know some of the physical properties such as density, molar volume, the concentration of ions, etc. Table 5.7 lists the different physical parameters calculated for the undoped and doped $SrMnO_3$.

Table 5.7 Density, hardness, molar volume, concentration, polaron radius and the distance between Ni^{2+} ions of $SrMn_{1-x}Ni_xO_{3-\delta}$ ($0.00 \leq x \leq 0.20$)

Sample label	ρ ($g\ cm^{-3}$)	Hardness (GPa)	V_m ($cm^3\ mole^{-1}$)	N ($\times 10^{22}\ cm^{-3}$)	r_p ($\times 10^{-8}$ cm)	R ($\times 10^{-8}$ cm)
SM-0	3.01	0.71	31.16	-	-	-
SMN-5	3.47	1.45	26.96	5.31	1.07	2.66
SMN-10	3.46	1.42	26.97	2.64	1.35	3.36
SMN-15	3.36	1.85	27.70	1.70	1.57	3.89
SMN-20	3.31	2.04	28.05	1.26	1.73	4.30

In contrast to the density of the Cu-doped $SrMnO_3$, the incorporation of Ni in $SrMnO_3$ leads to a significant decrease in the density. This decrease might be due to the presence of open pores in the microstructure of Ni-doped samples. The hardness of Ni-doped samples, on the other hand, increases considerably. The molar volume is inversely proportional to density increases as the density decreases. It could be due to the lower molar mass of NiO (74.692 $gmol^{-1}$) than MnO_2 (86.936 $gmol^{-1}$). The trend observed in the N, R and r_p is similar to the Cu-doped $SrMnO_3$.

5.2.4. Microstructural analysis

In contrast to the Cu-doped samples, there is not much variation observed in the microstructure of the Ni-doped $SrMnO_3$. Moreover, the grain sizes of Ni-doped samples, as seen in Table 5.8, are comparatively smaller than Cu-doped samples, which might be better for the ionic conduction. The grains of the Ni-doped samples are heterogeneous in size and shape as shown in Fig. 5.17 (a-e).

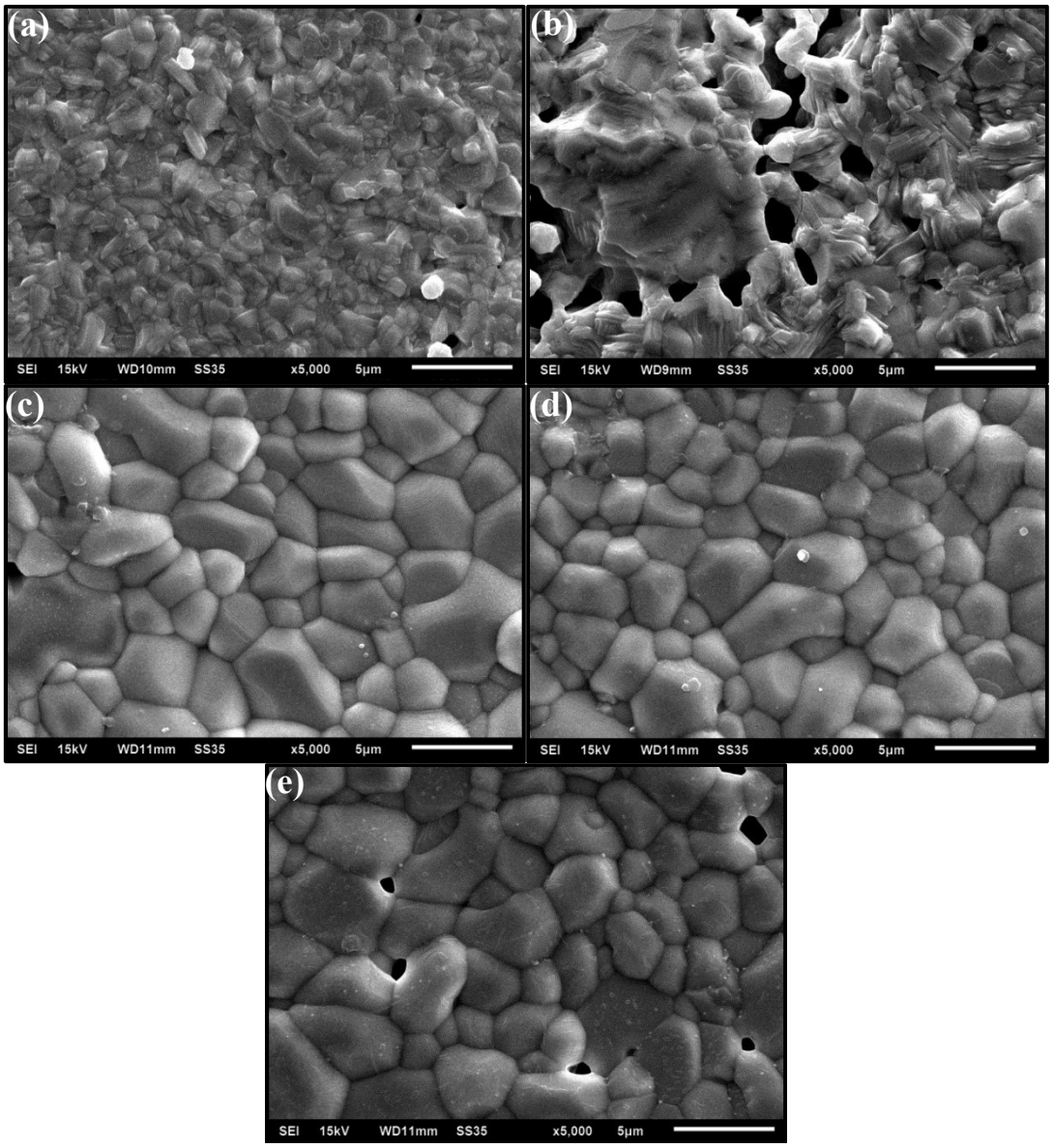


Fig. 5.17 SEM micrographs of (a) SM-0, (b) SMN-5, (c) SMN-10, (d) SMN-15 and (e) SMN-20

The interconnectivity of the grains and change in the grain size could be related to the effective doping of Ni in $SrMnO_3$ and open porosity, as seen in Fig. 5.17 (b). Partial melting is observed in SMN-5, which leads to the non-uniformity in the sizes of the grains. The change in the grain size is in accordance with the FWHM of the XRD peaks. The increase in the grain size of SMN-20 might be due to abnormal grain growth, which decreases the system's density (Fig. 5.18).

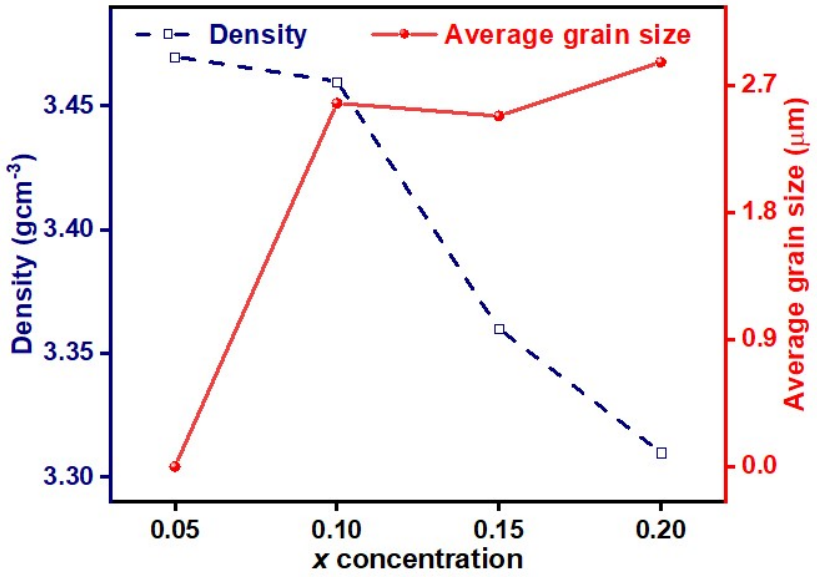


Fig. 5.18 Variation in the density and average grain size of Ni-doped $SrMnO_3$ with increasing dopant concentration

The elemental analysis in Table 5.8 reveals Sr, Mn and Ni in the $SrMnO_3$ even after heat-treatment, thereby maintaining the required stoichiometry.

Table 5.8 Weight % of the different elements of the composition $SrMn_{1-x}Ni_xO_{3-\delta}$ ($0.00 \leq x \leq 0.20$)

Sample Id	Average grain size (μm)	Sr	Mn	Ni	O
		wt%			
SM-0	1.22	51.39	30.38	-	18.23
SMN-5	Partial melt	51.49	29.71	0.59	18.21
SMN-10	2.57	55.09	22.37	4.69	17.85
SMN-15	2.48	55.64	22.58	3.96	17.82
SMN-20	2.86	54.91	22.81	4.41	17.87

5.2.5. TG-DTA analysis

As observed in the Cu-doped $SrMnO_3$, the weight loss seems relatively continuous with no sharp change in the TG plots. Slight changes are observed between 200-400°C and ~700°C in the doped samples. The loss of ~300°C could be due to the loss of moisture content from the samples. However, the weight loss at higher temperatures is attributed to the internal

structural changes such as oxygen vacancies creation and the presence of strain in the samples [39]. The weight loss amongst the Ni-doped samples is less as compared with Cu-doped samples.

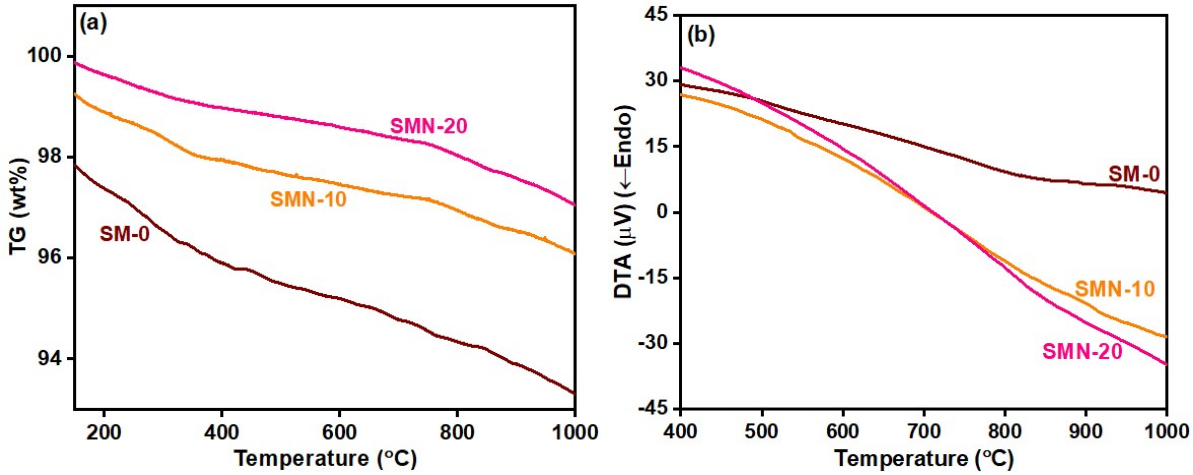


Fig. 5.19 Representative (a) TG plots and (b) DTA curves of $SrMn_{1-x}Ni_xO_{3-\delta}$ (x=0.00, 0.10, 0.20)

The DTA curves of the undoped and doped samples do not show any change. No significant endothermic and exothermic peaks are observed in the Ni-doped samples. Similar to Cu-doped samples, the DTA suggests thermal stability of Ni-doped $SrMnO_3$ up to 1000°C. Overall, both the Cu and Ni-doped samples are thermally stable up to 1000°C without any phase transitions.

5.2.6. Thermal expansion analysis

Fig. 5.20 shows the linear thermal expansion curves of $SrMn_{1-x}Ni_xO_{3-\delta}$ ($0.00 \leq x \leq 0.20$) in the temperature range of 200-1000°C. The CTE of SM-0, SMN-5, SMN-10, SMN-15 and SMN-20 are 9.52, 9.92, 10.20, 9.56 and 9.64×10^{-6} $°C^{-1}$, respectively. As in the case of Cu-doped samples, the Ni-doped samples have higher CTE than the undoped sample. The increase in the CTE is due to the lowering of the interatomic bond strength of $SrMnO_3$ on Ni doping. Shifting the FTIR bands towards lower diffraction angles supports the lowering of the bond strength and higher bond length. The oxygen vacancy formation is also responsible for the

increase in the CTE since the missing oxygen from the lattice lowers the interatomic bond strength and increases the CTE [24].

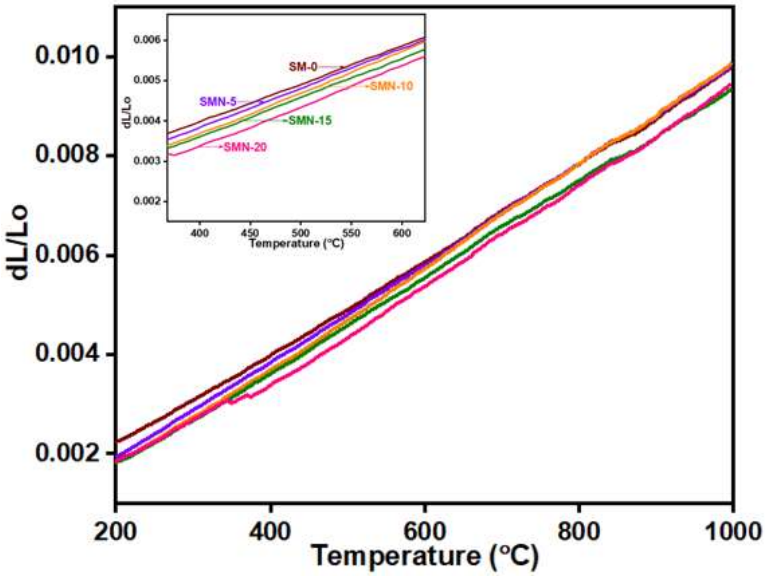


Fig. 5.20 Thermal expansion curves of $SrMn_{1-x}Ni_xO_{3-\delta}$ ($0.00 \leq x \leq 0.20$)

Also, the field strength of the dopant is higher than the host (Appendix), which leads to an increase in the CTE of the doped samples. The overall effect of the Ni dopant on $SrMnO_3$ is similar to Cu-doped samples with the CTE values in the required SOFC range, making them suitable for use as cathode materials for SOFCs.

5.2.7. Conductivity analysis

The representative Nyquist plots of SMN-15 and SMN-20 along with the equivalent circuit are shown in Fig. 5.21. Well defined semi-circular plots are observed at room temperature; however, with the rising heat temperature duration, the semi-circles distort as in Cu-doped $SrMnO_3$. The distortion can be attributed to the replacement of Mn^{4+} by Ni^{2+} and the reduction of manganese from Mn^{4+} to $Mn^{2+/3+}$.

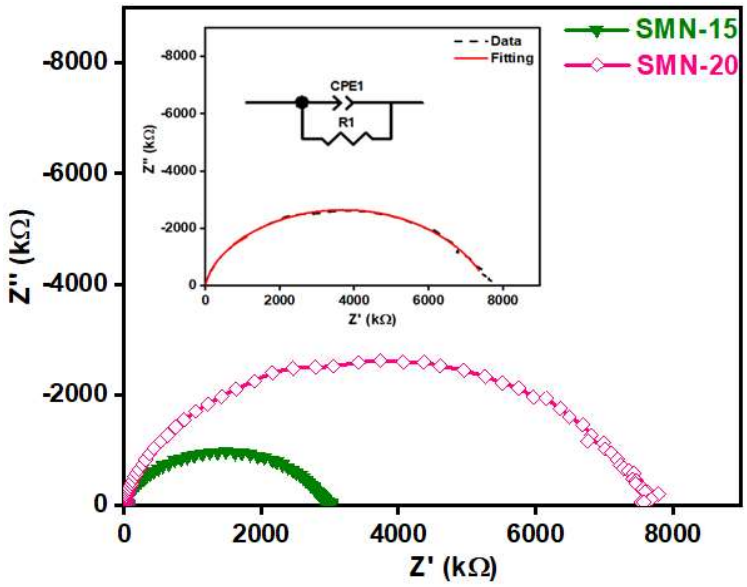


Fig. 5.21 Room-temperature Nyquist plots of SMN-15 and SMN-20 exhibiting similar characteristics as that of Cu-doped $SrMnO_3$ and the inset showing the corresponding equivalent circuit for SMN-20

The conductivity values listed in Table 5.9 show that the conductivity of the Ni-doped samples is lower than that of Cu-doped samples. The increasing dopant concentration decreases the conductivity of the system. Similar to the case of Ni-doped samples, the reduction of manganese generates vacancies in the system. However, their effect is nullified by introducing Ni^{2+} having the same or less charge as Mn^{2+} and Mn^{3+}, respectively. The decreasing density at the cost of higher porosity could also be a possible reason for the decrease in conductivity [40]. In other words, higher disorder leads to a decrease in the overall conductivity of the systems.

Table 5.9 Total conductivity (σ) of $SrMn_{1-x}Ni_xO_{3-\delta}$ ($0.00 \leq x \leq 0.20$)

Sample	σ (Scm^{-1})			
	RT	200°C	400°C	600°C
SM-0	2.83×10^{-6}	1.20×10^{-4}	4.27×10^{-3}	2.32×10^{-2}
SMN-5	1.01×10^{-6}	4.77×10^{-5}	1.77×10^{-3}	8.60×10^{-3}
SMN-10	1.71×10^{-7}	1.23×10^{-5}	1.20×10^{-3}	1.20×10^{-2}
SMN-15	4.45×10^{-8}	3.76×10^{-6}	4.00×10^{-4}	2.03×10^{-2}
SMN-20	1.20×10^{-8}	2.87×10^{-7}	4.75×10^{-5}	1.48×10^{-3}

However, the conductivity increases with the increase in the temperature exhibiting the semiconducting nature of the samples. It is deduced from the conductivity values that the conductivity of the doped as compared with the undoped sample varies by only an order. Similar to the Cu-doped $SrMnO_3$, the conductivity is dominated by the grain boundaries than the grains since the capacitance of the Ni-doped $SrMnO_3$ is of the order of 10^{-10} F.

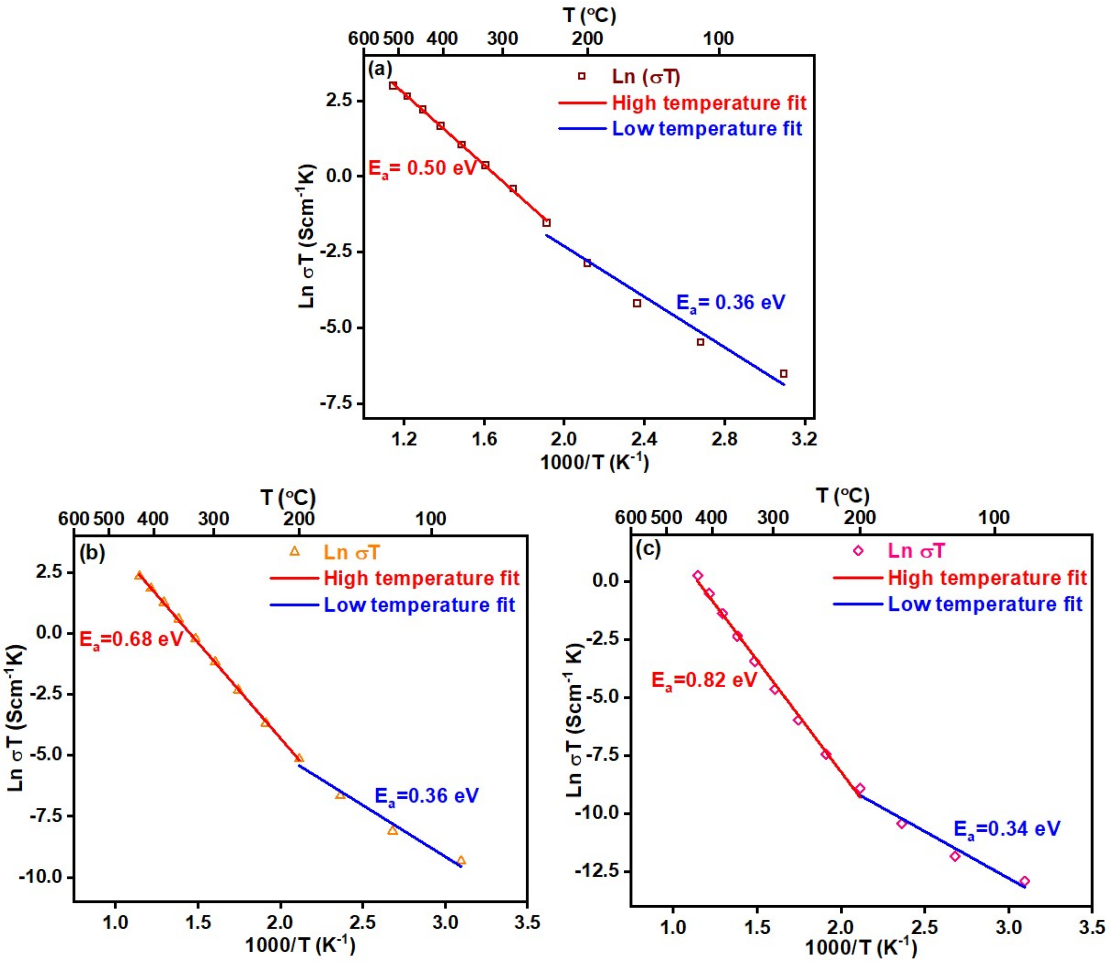


Fig. 5.22 Representative Arrhenius plots of SM-0, SMN-10 and SMN-20

The Arrhenius plots of Ni-doped $SrMnO_3$ are shown in Fig. 5.22, and the deduced E_a values are listed in Table 5.10. The doped samples have higher activation energies than the doped samples. Also, the high-temperature regime has higher activation energy than the low-temperature regime. Because there is a loss of oxygen at high temperatures, a decrease in manganese's valence state makes the high-temperature slope steep, as in the case of $CaMnO_3$

[40-43]. The higher concentration of Mn^{3+} increases the conductivity of the system. Therefore, it is observed from the literature that in manganite-based materials, the conduction phenomenon is through a thermally activated polaron hopping mechanism [44-46].

Table 5.10 Activation energy (E_a) of $SrMn_{1-x}Ni_xO_{3-\delta}$ ($0.00 \leq x \leq 0.20$)

Sample label	E_a (eV)	Temperature range (°C)
SM-0	0.36	50-250
	0.50	300-600
SMN-5	0.33	50-200
	0.50	250-600
SMN-10	0.36	50-200
	0.68	250-600
SMN-15	0.38	50-200
	0.71	250-600
SMN-20	0.34	50-200
	0.82	250-600

So the doping of Cu and Ni in $SrMnO_3$ does not create many oxygen vacancies. They reduce the Mn^{4+} to $Mn^{3+/2+}$ and create limited oxygen vacancies in the doped systems. Moreover, they also increase the tendency to form the secondary phase, mainly related to $Mn^{3+/2+}$ containing systems like Mn_3O_4. The presence of secondary phases, porosity, and ordering of oxygen might be the reason to reduce the conductivity in these systems with respect to dopant concentration.

Summary

Undoped and doped $SrMnO_3$ are multiphase systems with variable microstructural features. Ni doping increases the tendency to form secondary phases, i.e. Mn_3O_4. Doped and undoped $SrMnO_3$ samples exhibit higher porosity than $SrZrO_3$ samples. CTE of $SrMn_{1-x}A_xO_{3-\delta}$ (A: Cu, Ni; $0.00 \leq x \leq 0.20$) is ~$9\text{-}13 \times 10^{-6}$ $°C^{-1}$ between 200-1000°C. The conductivity increases by four orders in the doped samples as compared to the undoped $SrMnO_3$ at 600°C.

References

[1] R. Sondena, P. Ravindran, S. Stolen, Phys. Rev. B 74 (2006) 144102(1)-(12).

[2] T. Negas, R.S. Roth, J. Solid State Chem. 1 (1970) 409-418.

[3] R.K. Hona, F. Ramezanipour, Inorg. Chem. 59 (2020) 4685-4692.

[4] H.W. Nesbitt, D. Banerjee, Am. Min. 83 (1998) 305-315.

[5] J.F. Moulder, W.F. Stickle, P.E. Sobol, K.D. Bomben, Perkin Elmer, Eden Prairie (USA), 1992.

[6] F. Wang, Y.Q. Zhang, Y. Bai, W. Liu, H.R. Zhang, W.Y. Wang, S.K. Li, S. Ma, X.G. Zhao, J.R. Sun, Z.H. Wang, Z.J. Wang, Z.D. Zhang, Appl. Phys. Lett. 109 (2016) 052403 (1)-(6).

[7] V.K. Kaushik, Spectrochim Acta 44(B)(6) (1989) 581-587.

[8] J.P. Espinos, J. Morales, A. Barranco, A. Caballero, J.P. Holgado, A.R.G. Elipe, J. Phys. Chem. B 106 (2002) 6921-6929.

[9] R. Bujakiewicz-Koronska, D. Nalecz, A.M. Majcher, E. Juszynska-Galazka, M. Galazka, L. Vasylechko, E. Markiewicz, D. Majda, A. Kalvane, K. Koronski, J. Eur. Ceram. Soc. 37 (2017) 1477-1486.

[10] R.D. Shannon, Acta Cryst. A32 (1976) 751-767.

[11] G. George, S.L. Jackson, C.Q. Luo, D. Fang, D. Luo, D. Hu, J. Wen, Z. Luo, Ceram. Int. 44(17) (2018) 21982-21992.

[12] M. Khazaei, A. Malekzadeh, F. Amini, Y. Mortazavi, A. Khodadadi, Cryst. Res. Technol. 45(10) (2010) 1064-1068.

[13] M. Mylarappa, V. V. Lakshmi, K.R.V. Mahesh, H.P. Nagaswarupa, N. Raghavendra, IOP Conf. Series: Mater. Sci. Engg. 149 (2016) 012178(1)-(9).

[14] F. Soleimani, M. Salehi, A. Gholizadeh, Iran. J. Sci. Technol. Trans. Sci. 44 (2020) 1011-1023.

[15] I. Kashif, A. Ratep, Appl. Phys. A 120(4) (2015) 1427-1434.

[16] K.R. Kambale, A.R. Kulkarni, N. Venkataramani, Ceram. Int. 40(1) (2014) 667-673.

[17] D. Maurya, M. Murayama, S. Priya, J. Am. Ceram. Soc. 94(9) (2011) 2857-2871.

[18] M. Zhao, W. Pan, Acta Materialia, 61(14) (2013) 5496-5503.

[19] H. Lu, C. Wang, Y. Huang, H. Xie, Sci. Rep. 4 (2014) 1-7.

[20] J. Liu, Z. Jiang, P. Servati, E. Asselin, J. Am. Ceram. Soc. 99(4) (2016) 1125-1128.

[21] T.A.G. Restivo, S.R.H.M. Castanho, Int. J. Mater. Res. 101 (2010) 128-132.

[22] A.M.F.R. Pinto, V.S. Oliveira, D.S.C. Falcao, First ed., Academic Press, Cambridge (USA), 2018.

[23] H. Lu, C. Wang, Y. Huang, H. Xie, Sci. Rep. 4 (2014) 1-7.

[24] S. Thakur, O.P. Pandey, K. Singh, Part. Sci. Technol. 33 (2015) 178-183.

[25] Q. Zhu, T. Jin, Y. Wang, Solid State Ion. 177 (2006) 1199-1204.

[26] J. Liu, Z. Jiang, P. Servati, E. Asselin, J. Am. Ceram. Soc. 99(4) (2016) 1125-1128.

[27] A. Manthiram, J. Kim, Y.N. Kim, K.T. Lee, J. Electroceram. 27 (2011) 93-107.

[28] S. Hashimoto, H. Iwahara, J. Electroceram. 4(1) (2000) 225-231.

[29] S. Nasri, M. Megdiche, M. Gargouri, Ionics 21 (2015) 67-78.

[30] B. Tiwari, R.N.P. Choudhary, IEEE Trans. Dielectr. Electr. Insul. 17(1) (2010) 5-17.

[31] C. Chang, C. Hsu, T. Huang, J. Solid State Electrochem. 7 (2003) 125-128.

[32] X. Yuan, C. Song, H. Wang, J. Zhang, Springer-Verlag, London (UK), 2010

[33] A.M. Hussain, K. Pan, Y. Huang, I.A. Robinson, C. Gore, E.D. Wachsman, ACS Appl. Mater. Interfaces 10 (2018) 36075-36081.

[34] S. Omar, E.D. Wachsman, J.C. Nino, Solid State Ion. 177 (2006) 3199-3203.

[35] J. Pappis, W.D. Kingery, J. Amer. Ceram. Soc. 44(9) (1961) 459-464.

[36] A.N. Mansour, Surf. Sci. Spectra. 3 (1994) 231-238.

[37] S. Gholamrezaei, M.S. Niasari, Ultrason. Sonochem 40 (2018) 651-663.

[38] M. Khazaei, A. Malekzadeh, F. Amini, Y. Mortazavi, A. Khodadadi, Cryst. Res. Technol. 45(10) (2010) 1064-1068.

[39] J. Richter, P. Holtappels, T. Graule, L.J. Gauckler, Solid State Ion. 179 (2008) 2284-2289.

[40] J.W. Seo, C.M. Kim, K. Park, Powder Technol. 278 (2015) 11-16.

[41] H. Taguchi, M. Nagao, T. Sato, M. Shimada, J. Solid State Chem. 78 (1989) 312-315.

[42] I.P. Marozau, V.V. Kharton, A.P. Viskup, J.R. Frade, V.V. Samakhval, J. Eur. Ceram. Soc. 26 (2006) 1371-1378.

[43] A. Bhaskar, C. Liu, J.J. Yuan, C. Chang, J. Alloys Compd. 552 (2013) 236-239.

[44] J.W. Stevenson, M.N. Nasrallah, H.U. Anderson, D.M. Sparlin, J. Solid State Chem. 102 (1993) 175-184.

[45] K. Park, G.W. Lee, J. Jung, S.J. Kim, Y.S. Lim, S.M. Choi, W.S. Seo, J. Nanosci. Nanotechnol. 11 (2011) 7176-7176.

[46] D. Gutierrez, O. Pena, P. Duran, C. Moure, J. Eur. Ceram. Soc. 22 (2002) 567-572.

Overview

In this chapter, the chemical interaction between the proposed cathode material, $SrZr_{0.85}Cu_{0.15}O_{3-\delta,}$ and glass sealant, $45SiO_2+40BaO+10B_2O_3+5ZrO_2$, as well as Crofer 22 APU interconnect is reported. SZC-15 is chosen based on appropriate CTE as compared with glass sealant and interconnect material. This interaction study aims to understand the different crystalline phase formations which are detrimental to the SOFC operation. Characterization techniques such as XRD, SEM, and dilatometry analyze the samples for structural, microstructural, and thermal changes, respectively.

6.1. Interaction study with sealant and interconnect

In the planar SOFC design, the cathode comes in direct contact with the glass sealant (developed in our lab) and interconnects. Therefore, a boro-silicate glass sealant and interconnect have been chosen for compatibility test or interaction study with a perovskite-structured cathode material, i.e., $SrZr_{0.85}Cu_{0.15}O_{3-\delta}$. The basis for choosing the cathode materials was comparable CTE and good overall conductivity at 600°C with the glass sealant and the interconnect material. Glasses are amorphous; however, during SOFC operation, they convert into glass-ceramics which have crystalline phases embedded in the glass matrix. Therefore, the formation of crystalline phases and their volume fraction play an important role in deciding the lifespan of a SOFC. The chemical interactions between the samples have been investigated using XRD, SEM, and dilatometry to check for the presence of any detrimental phases and their effect on thermal expansion behaviour.

6.1.1. XRD analysis

The highly crystalline XRD peaks of the heat-treated samples (diffusion couple) at 1, 10, 100, and 500 hrs, respectively, are shown in Fig. 6.1(a, b). For reference, this figure also includes XRD patterns of SZC-15 and SBBZ (glass sealant) for comparison. The most prominent crystalline peaks positioned ~30.8°, ~44.2°, ~54.9°, ~64.2°, ~72.9°, and ~89.4°, respectively belong to the orthorhombic $SrZrO_3$ (ICDD: 01-070-0283).

From the XRD patterns of IS-1, there is no clear indication of any other phase apart from the perovskite phase, i.e., it belongs to the cathode material. However, the broadening of the highest intense peak of IS-1 compared with SZC-15 indicates the beginning of diffusion from the glass sealant side. However, the formation of other crystalline phases is evident as heat treatment duration increase from 10, 100 and 500 hrs, respectively (Fig. 6.1(b)). Table 6.1 lists the volume fraction of these phases. There is an increase in the $BaSrSi_2O_6$ and SiO_2

phases with increasing heat duration. However, after 500 hrs of heat treatment, $SrZrO_3$ increases at the cost of $BaSrSi_2O_6$ and SiO_2 phases.

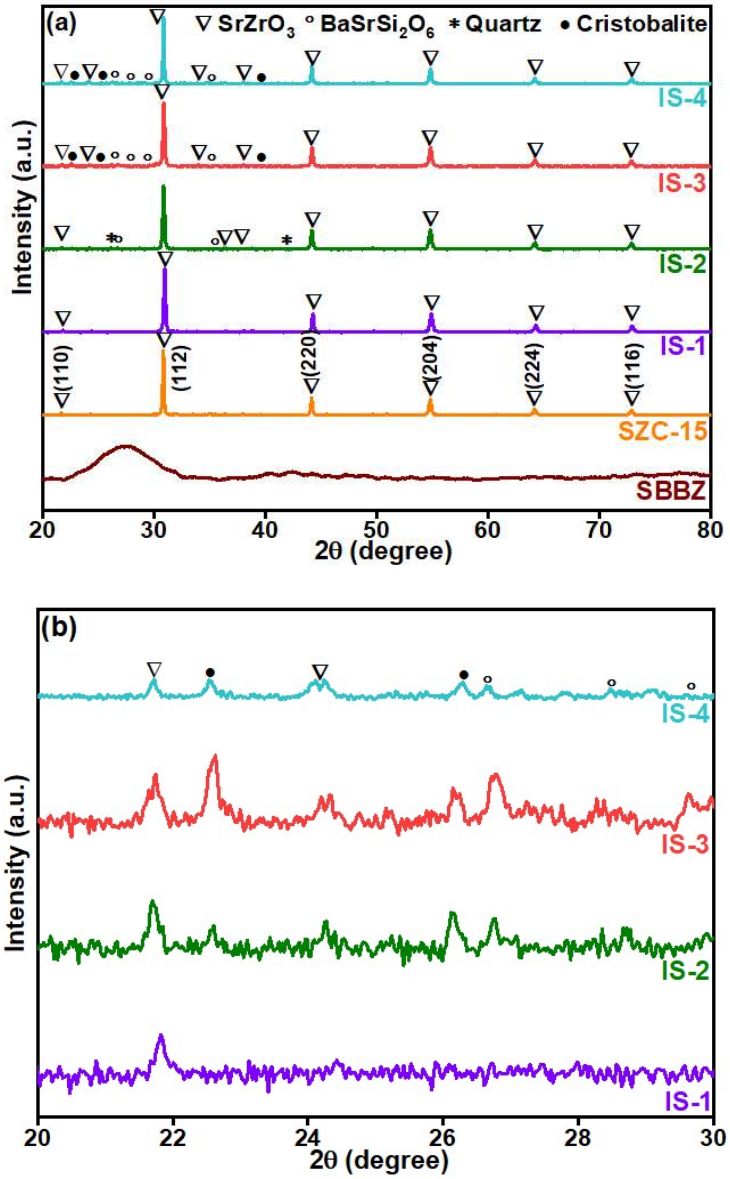


Fig. 6.1 XRD patterns of (a) SBBZ, SZC-15, IS-1, IS-2, IS-3, and IS-4 representing the presence of $BaSrSi_2O_6$, quartz, and cristobalite phases and (b) magnified view of the secondary phases

In the XRD patterns of IS-2, there is a slight presence of small peaks of β-quartz (hexagonal SiO_2: ICDD: 01-075-1555) and barium strontium silicate phase, i.e., $BaSrSi_2O_6$ (ICDD: 00-020-0143). It implied diffusion between Si^{4+} and Ba^{2+} from the glass sealant and the Sr^{2+}

from the cathode side and formed the new crystalline phase with respect to time and temperature. The presence of such a secondary $BaSrSi_2O_6$ phase has been reported during the synthesis of other alkaline-based sealants and perovskite structured oxides [1, 2].

Table. 6.1 Volume fraction (%) of the different crystalline phases

Sample label	$SrZrO_3$	$BaSrSi_2O_6$	SiO_2
IS-1	100	-	-
IS-2	97.90	1.31	0.77
IS-3	91.75	3.93	4.31
IS-4	95.53	1.41	3.05

The diffusion between Ba (0.135 nm) and Sr (0.118 nm) could be due to their comparable ionic radii. Another interesting feature is the conversion of quartz into tetragonal SiO_2, i.e., cristobalite (tetragonal SiO_2: ICDD: 01-082-1556) at 100 hrs of heat treatment duration. Cristobalite stabilizes between 1470-1710°C; however, its presence at 800°C implies that longer heat treatment durations result in the cristobalite phase [3]. The formation of a cristobalite phase is not desired since it undergoes a structural change ~200°C involving a significant volume change. Change in the volume leads to cracks and strain during cooling, which is detrimental during the SOFC operation [4].

However, the presence of these minor phases is not much significant compared to the major $SrZrO_3$ phase, as seen from the volume fraction difference between the minor and major phases. Also, the volume fraction of $BaSrSi_2O_6$ and SiO_2 decreases at 500 hrs of heat treatment duration. Their presence does not affect the density of the samples, as seen in Table 6.2. The density of IS-1, IS-2, and IS-3 is less than pure SZC-15; however, the heat treatment duration does not cause much change in the densities of IS-1, IS-2, and IS-3 samples. Moreover, at 500 hrs of heat treatment, the density is comparable to SZC-15. It could be related to the different method adapted to make these samples.

Table 6.2 FWHM, crystallite size and density of SZC-15, IS-1, IS-2, IS-3 and IS-4

Parameters	SZC-15	IS-1	IS-2	IS-3	IS-4
FWHM (°)	0.164	0.206	0.210	0.209	0.169
Crystallite size (nm)	54.59	42.89	42.16	42.51	53.83
Density (gcm^{-3})	3.36	3.14	3.38	3.26	4.36

Compared with SZC-15, there is a significant change in the peak positions of the highest intense peaks of XRD, as shown in Fig. 6.2. In IS-1, the peaks shift towards higher angles in comparison with SZC-15. However, with a further increase in the heat treatment duration, there is a significant shift towards lower diffraction angles. The variation in the peak positions can be attributed to the difference in the ionic radii of Si (0.04 nm), Sr, and Ba. Also, the increase in the heat treatment durations increases the FWHM, as shown in Table 6.2.

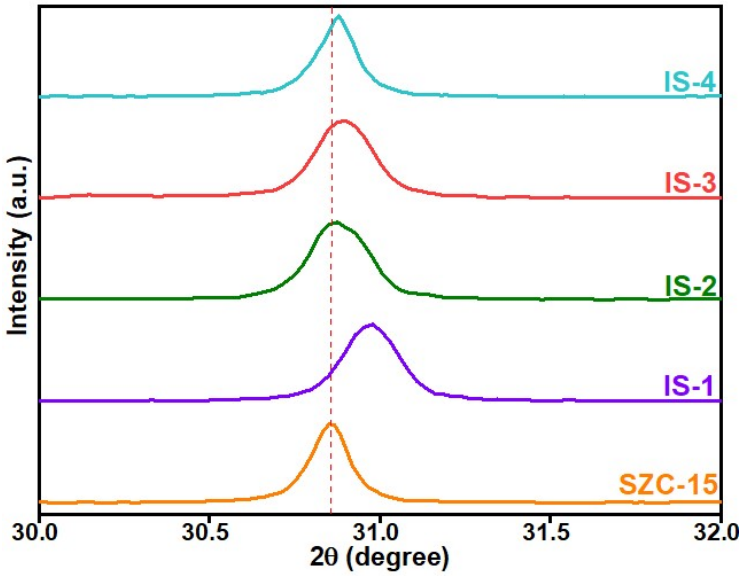


Fig. 6.2 XRD peak shifting highest intense peak corresponding to (112) plane of IS-1, IS-2, IS-3, and IS-4 with respect to SZC-15

Compared with SZC-15, the crystallization of different phases affects the crystallite size leading to broadening the XRD peaks of the heat-treated samples (Table 6.2). The broadening could also be due to the amorphous nature of the glass sealant. The presence of crystalline

phases decreases the crystallite size of the heat-treated samples. However, increasing heat durations up to 100 hrs decreases the broadening.

6.1.2. Microstructural analysis

Fig. 6.3 (a) shows the crystalline nature of SZC-15, while Fig. 6.3 (b-d) show the variation in the morphology of the samples on varying the heat durations. The crystalline SZC-15 has non-uniform grains; however, on mixing with glass sealant and after heat-treatment, the amorphous nature of the glass sealant becomes evident from the boxes shown in Fig. 6.3 (b).

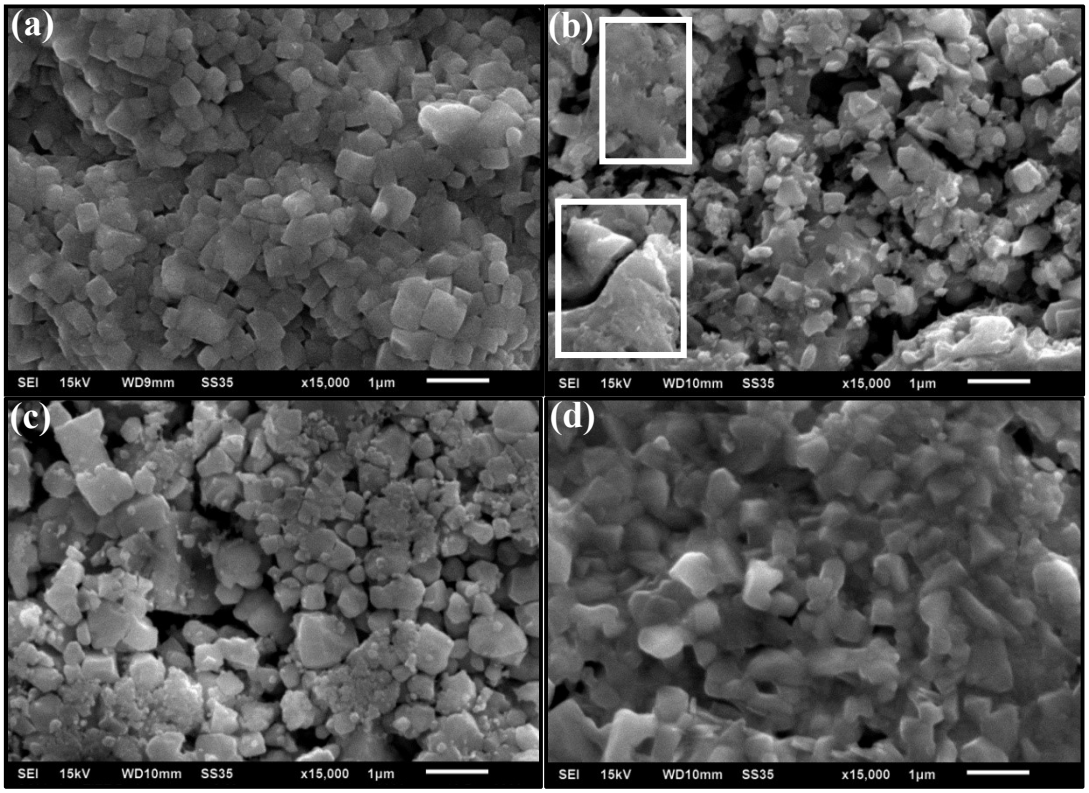


Fig. 6.3 SEM micrographs of (a) SZC-15, (b) IS-1, (c) IS-2 and (d) IS-3 showing variation in the microstructure

Liquid phase sintering (LPS) is also observed in 100 hrs heat-treated samples. LPS occurs when an additive melts before the base composition or the matrix [5]. CuO is known to have shown LPS during the synthesis of SZC [6]. The LPS is desirable since it provides a means for ionic transport in ceramic materials. The density of ceramic samples is often related to the

grain size and their distribution. The density of the present samples increases initially; however, with increasing heat duration, it decreases (Table 6.2). The increase might be due to the formation of grains, while the decrement could be due to the LPS.

FE-SEM of the diffusion couple was conducted to check the compactness and presence of any undesired phases. The FE-SEM micrographs of IS-4 shown in Fig. 6.4 show that even after prolonged heat-treatment for 500 hrs at 800°C, there is strong adhesion between the cathode and the sealant with no distinct fracture or delamination at the interface. It indicates that the cathode exhibits good bonding characteristics with the glass sealant. Even the FE-SEM sample preparation processing, i.e., grinding and polishing, did not cause any damage to the interface of the diffusion couple. As seen in the XRD micrographs, the secondary phases formed are not visible in the FE-SEM micrographs, justifying their presence in fewer amounts.

Table 6.3 lists the weight % of all the constituents of the composition. From the EDS point analysis, it is observed that the grains represent the perovskite cathode while agglomerated particles represent the glass sealant. It correlates with the fact that crystalline materials have a large number of grains while amorphous materials have one single large particle. There is slight diffusion between the cathode and the sealant with the increasing heat treatment duration, as observed from the line and dot mapping results in Fig. 6.5. It is observed that there is a diffusion of Si and Cu from the sealant and the cathode side, respectively. In $SrZrO_3$ (Chapter 4, Section 4.1.1), Cu does not form any phase itself but causes local level structural changes. However, silica, in this case, diffuses with Ba and Sr and forms $BaSrSi_2O_6$ due to the open structure of glass.

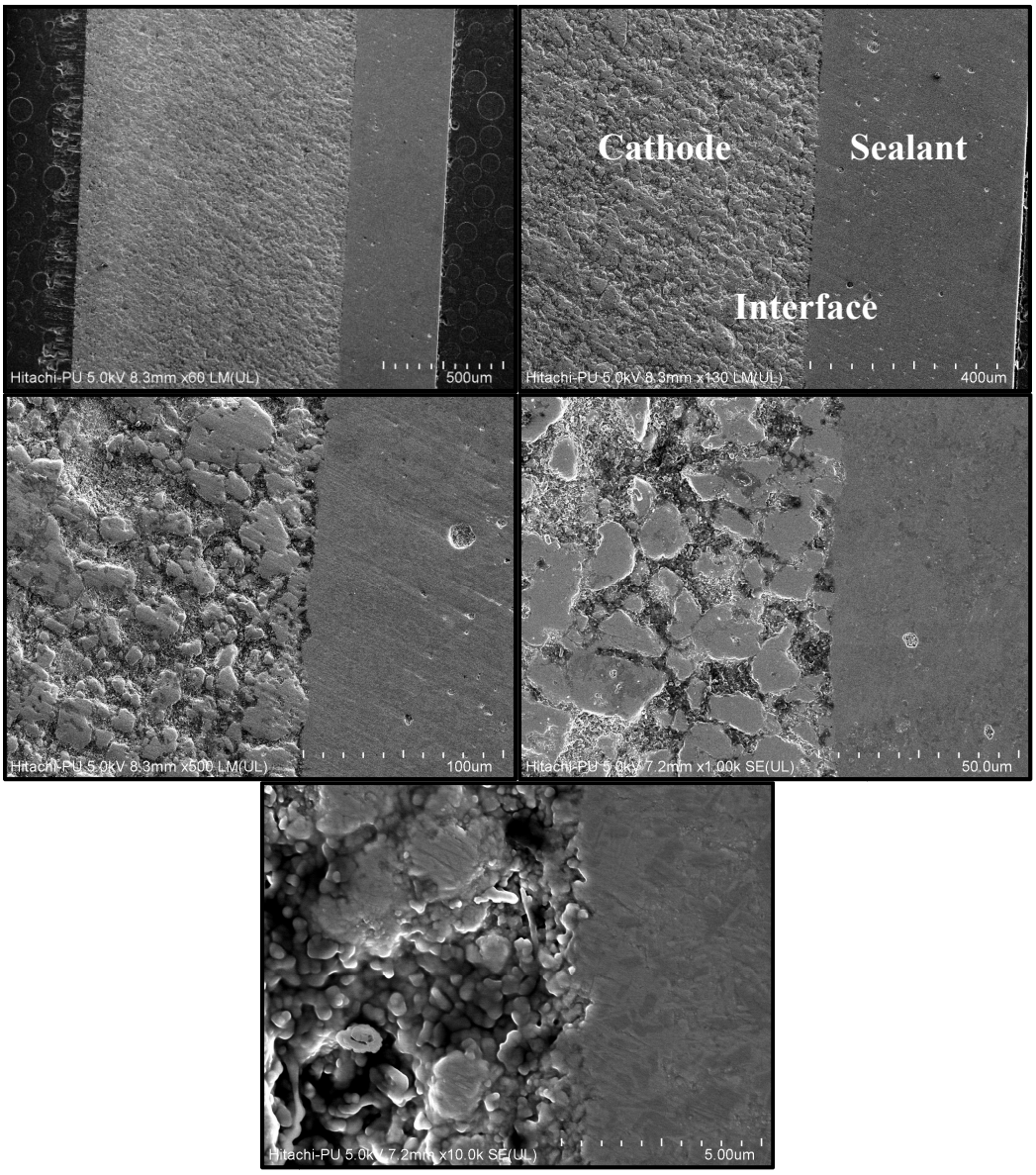


Fig. 6.4 FE-SEM micrographs showing a clear distinction between the cathode (left) and the glass sealant (right) with increasing magnification without the formation of any intermediate undesired phases at the interface

Table 6.3 Weight % of different constituents of the samples obtained from EDS analysis

Samples	Sr	Zr	Cu	Si	Ba	O
IS-1	30.94	29.5	0.73	3.21	14.14	21.49
IS-2	33.21	32.93	0.32	2.16	10.05	21.33
IS-3	37.64	32.20	0.13	1.27	8.15	20.60

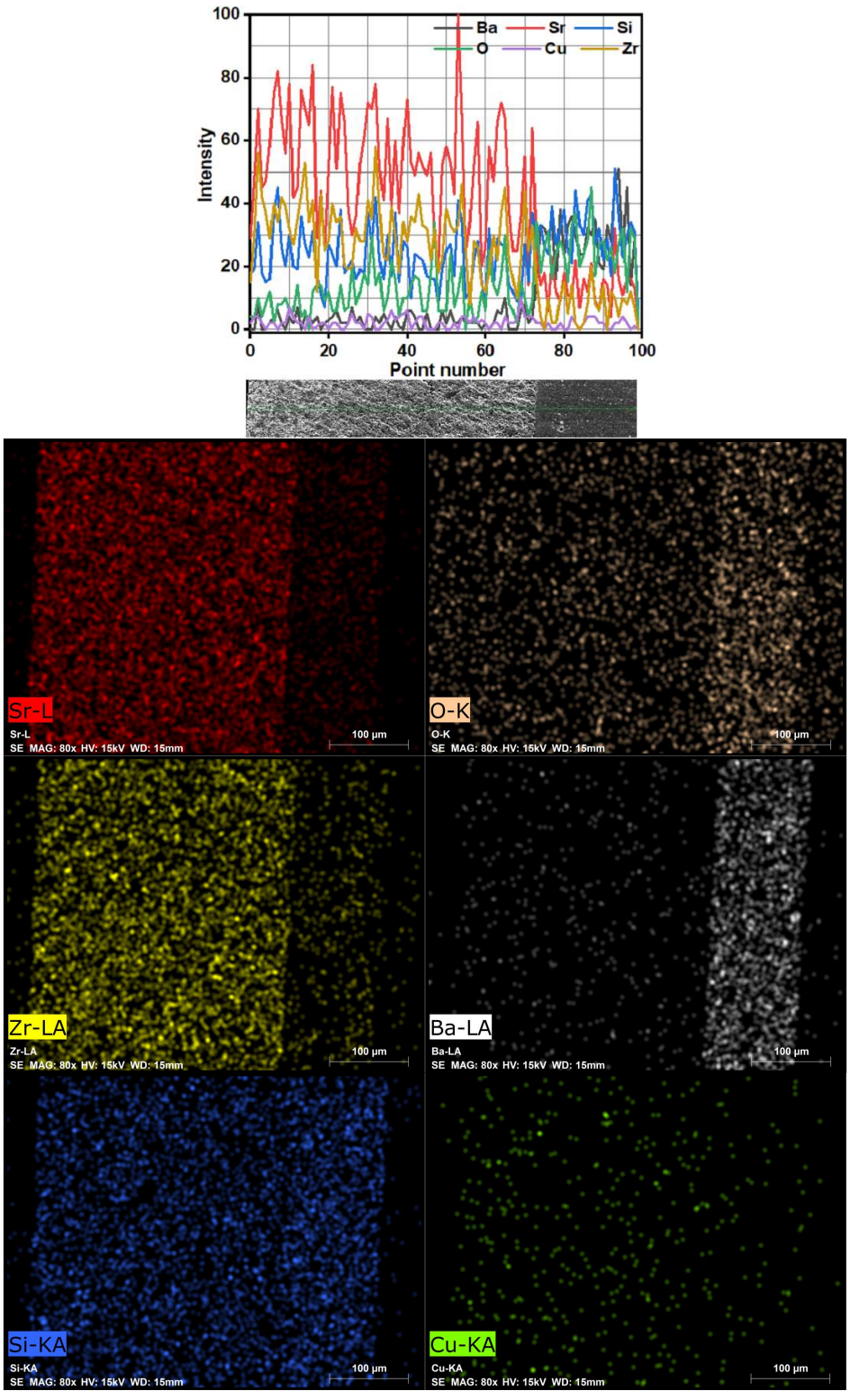


Fig. 6.5 Line and dot mapping of IS-4 showing the diffusion of different elements from cathode and glass side over the interface

6.1.3. Thermal expansion analysis

The linear CTE curves of the samples are shown in Fig. 6.6 (a). The linear curves of the CTE generally indicate the change in the crystal structure or the creation of oxygen vacancies due to the lattice oxygen loss at elevated temperatures [7]. The samples IS-1 and IS-2 have linear CTE curves; however, a slight change in the slope is observed in IS-3 and IS-4 due to the presence of secondary phases or lattice oxygen loss.

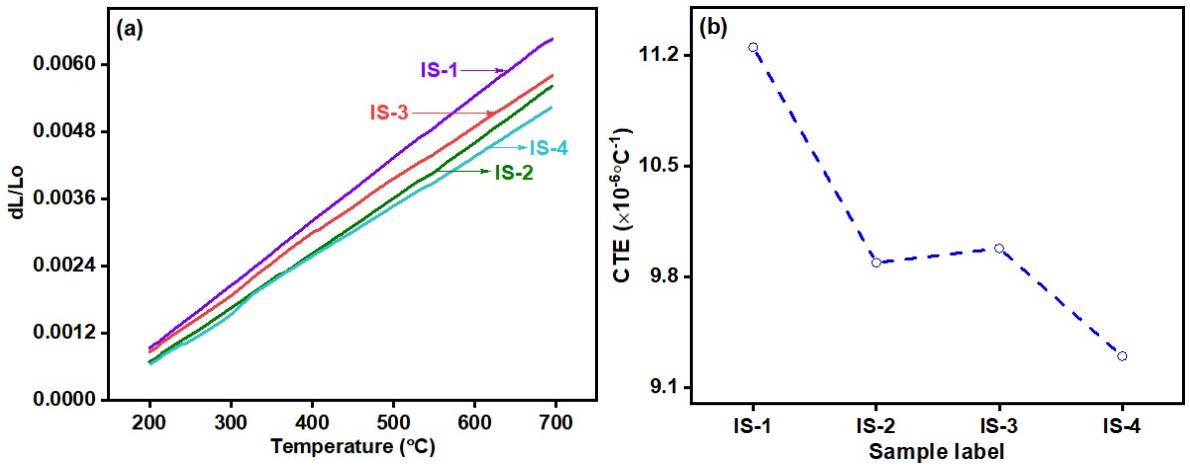


Fig. 6.6 (a) The thermal expansion curves of IS-1, IS-2, IS-3, and IS-4, respectively, and (b) variation in the CTE of the samples with increasing heat durations

Fig. 6.6 (b) shows the variation in the CTE with increasing heat treatment durations. The CTE of the samples is comparable with the CTEs of other SOFC components, thereby making them useful for SOFC applications [8-10]. As seen from the SEM micrographs, the diffusion between the cathode and the glass sealant starts majorly at 100 and 500 hrs of heat treatment duration. It has been verified from the slight change in the slope of IS-3 and IS-4. It is known that strongly bonded materials have lower CTE than weakly bonded materials [11]. The decreasing CTE of IS-2 shows enhanced bond formation with heat duration. The CTE of SZC-15 and SBBZ independently is 11.85 and 10.28×10^{-6} $°C^{-1}$, respectively. However, once the diffusion starts, there is a decrease in CTE. The decrease implies that the bond strength between the different constituents of the composition increases with increasing heat treatment

duration. Since the different crystalline phases are formed, and glass sealant has converted to glass-ceramics. The higher field strength of Si (2.24) compared with Ba (0.73), Cu (0.94), Zr (1.90), and Sr (0.78) might be responsible for the decrease in the CTE.

6.2. An interaction study with interconnect

Crofer 22 APU is a ferrite stainless steel interconnect material used to hold various single cells together. It comes in direct contact with the anode of one cell and the cathode of the consecutive cell. Therefore, apart from the interaction study of cathode material with the glass sealant, it is also essential to know the chemical interaction of the cathode with interconnect. Crofer 22 APU is a high-temperature ferrite stainless steel that contains 22 wt. % chromium and exhibits a CTE of 11.5×10^{-6} $°C^{-1}$ [12, 13]. The XRD patterns of the samples heat-treated at 1000°C for 1 and 10 hrs, respectively, are shown in Fig. 6.7.

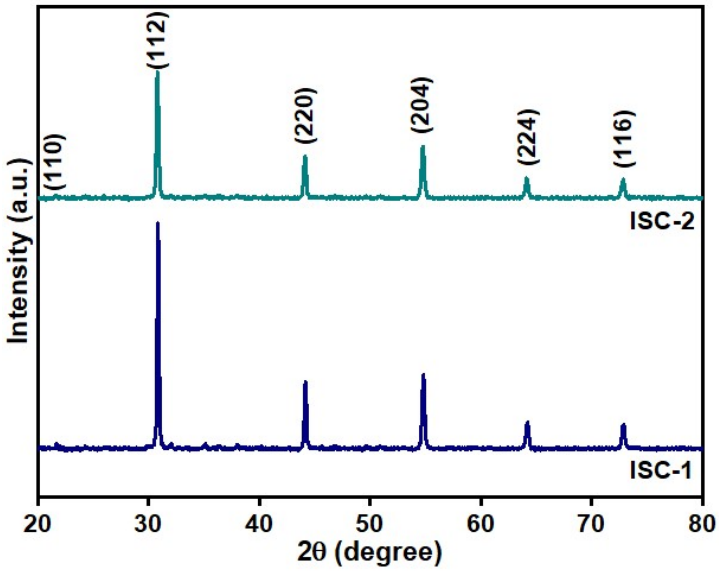


Fig. 6.7 XRD patterns of ISC-1 and ISC-2 showing no presence of Crofer elements

On analyzing the XRD patterns, it was observed that there is no diffusion between the Crofer and the cathode materials. Since no peaks belong to the Crofer constituents in the XRD, all the peaks belong to orthorhombic $SrZrO_3$. Also, on physically observing the samples, it was observed that there was no adhesion between the SZC-15 powder sample and Crofer rectangular bars even after heat treatment at 1200°C (Fig. 6.8).



Fig. 6.8 Representative picture of the heat-treated diffusion couple of the cathode-glass sealant. The rectangular bars are the Crofer 22 APU and the brown powdered layer sandwiched between the layers is SZC-15

Although the samples had comparable CTE, however, there was not much adhesion between them. It might be associated with the CTE mismatch at high temperatures, i.e., ≥1000°C, since the diffusion couple was heat-treated at 1000°C and 1200°C, respectively. Conclusively, Crofer 22 APU is not compatible with the developed cathode material, $SrZr_{0.85}Cu_{0.15}O_{3-\delta}$.

Summary

Diffusion couple of $SrZr_{0.85}Cu_{0.15}O_{3-\delta}$ with the glass sealant $45SiO_2+40BaO+10B_2O_3+5ZrO_2$ is smooth and intact even after heating for long durations ~500 hrs at 800°C. Most importantly, the CTE of the diffusion couple does not change after exposure for 500 hrs at 800°C. The developed samples do not form any bonding with interconnect materials.

References

[1] V.P. Ishchuk, M.V. Glumov, A.K. Demin, Inorg. Mater. 45(4) (2009) 440-443.

[2] M.C. Gust, L.A. Momoda, M.L. Mecartney, Mat. Res. Soc. Symp. Proc. 346 (1994) 649-653.

[3] K. Doyle, PhD thesis, Wright State University, Ohio (USA), 2020.

[4] N. Lahl, D. Bahadur, K. Singh, L. Singheiser, K. Hilpertz, J. Electrochem. Soc. 149(5) (2002) A607-A614.

[5] R.M. German, P. Suri, S.J. Park, J. Mater. Sci. 44 (2009) 1-39.

[6] T.A.G. Restivo, S.R.H Mello-Castanho, Int. J. Mater. Res. 101 (2010) 128-132.

[7] S. Thakur, O.P. Pandey, K. Singh, ECS Trans. 57(1) (2013) 2125-2132.

[8] O. Yamamoto, Electrochim. Acta 45 (2000) 2423-2435.

[9] M. Mogensen, T. Lindegaard, U.R. Hansen, J. Electrochem. Soc. 141(8) (1994) 2122-2128.

[10] S.P. Jiang, Solid State Ion. 146 (2002) 1-22.

[11] K. Sood, K. Singh, O.P. Pandey, J. Mater. Sci. 47 (2012) 4520-4529.

[12] F. Smeacetto, M. Salvo, M. Ferraris, J. Cho, A.R. Boccaccini, J. Eur. Ceram. Soc. 28 (2008) 61-68.

[13] V.M. Perez, A.M. Amesti, M.I. Arriortua, J. Power Sources 280 (2015) 505-515.

Overview

The conclusions drawn from the results are given in this chapter. Based on the conclusions, the present work's future prospects are also given at the end of the chapter.

7.1. Conclusion

The thesis aimed to study the effect of doping transition metal oxides (Cu^{2+} and Ni^{2+}) on the structural, thermal and conducting properties of strontium based perovskite-structured materials, i.e. $SrZrO_3$ and $SrMnO_3$. Doping of lower valence transition metal oxides at the B-site of $SrZrO_3$ and $SrMnO_3$, i.e. Zr and Mn, is expected to lower the sintering temperature and generate oxygen vacancies, increasing the overall conductivity of the materials. The polycrystalline samples, $SrM_{1-x}A_xO_{3-\delta}$ (M=Zr, Mn; A=Cu, Ni; $0.00 \leq x \leq 0.20$), were synthesized using the solid-state reaction method and characterized using several experimental techniques to check their suitability as cathode materials for IT-SOFCs.

Doped $SrZrO_3$ exhibit a single-phase orthorhombic structure, while $SrMnO_3$ exhibits multi phases. The formation of impurity phases in the doped $SrMnO_3$ system is related to the reduction of Mn^{4+} into Mn^{3+}/Mn^{2+} during heat treatment. The nickel doping has a higher effect on the reduction of Mn in $SrMnO_3$. Doping of Ni in $SrZrO_3$ increases the crack formation tendency due to the phase transition observed in DSC results. The shifting of the XRD peaks and bands in the FTIR spectra indicate effective doping of Cu and Ni in $SrMnO_3$ and $SrZrO_3$. The XPS of the selected samples confirms the multiple oxidation states of the transition metals. Doping increases the sinterability of $SrZrO_3$ than $SrMnO_3$. The CTE of all the developed cathode materials is in the required SOFC range, i.e. $9\text{-}13\times10^{-6}$ °C^{-1}. The TG-DTA of all the samples confirms the thermal stability of developed materials at the operating temperature of SOFC. Doping increased the conductivity of $SrZrO_3$ by two orders due to the presence of mixed states of Cu, leading to higher oxygen vacancy formation in this system. Also, the band gap and PL spectra of the Ni-doped show the presence of defects in $SrZrO_3$. Doping in the transition metal-containing system, i.e. $SrMnO_3$, reduces B-site (Mn) cations, restricting the formation of oxygen vacancies, thereby decreasing the system's conductivity and limiting the use of doped $SrMnO_3$ as SOFC cathode materials. The change in the slope of

the Arrhenius plots in all the samples indicates two types of conduction mechanisms that could be related to the mixed ionic and electronic conduction phenomenon.

$SrZr_{1-x}Cu_xO_{3-\delta}$ ($0.00 \leq x \leq 0.20$) is the best series amongst all the developed materials based on the monophasic nature, appropriate CTE and conductivity at SOFC operating temperatures. Therefore, the chemical interaction of $SrZr_{0.85}Cu_{0.15}O_{3-\delta}$ with a boro-silicate glass sealant and a commercially available interconnect material (Crofer 22 APU) was studied. The chemical interaction of the developed cathode materials with the glass sealant exhibited minimal detrimental phase formations, good adhesion and comparable CTE even after a heat treatment duration of 500 hrs in air. However, the selected samples could not show any adhesion with Crofer 22 APU even at 1200°C. Thus, highlighting the need to develop other interconnect materials that show affinity with our developed cathode materials.

7.2. Future scope

Based on the conclusions mentioned above, the following suggestions are recommended for further investigation of the systems:

i. Cu-doped $SrZrO_3$ samples could be tested in oxygen partial pressure to check the electronic and ionic contribution in overall electrical conductivity of the samples

ii. $SrMnO_3$ can be synthesized in the presence of oxygen atmospheres to form monophasic $SrMnO_3$ and prevent the reduction of Mn^{4+}

iii. Doping in the case of $SrMnO_3$ can be done at the A-site so that manganese stabilizes its oxidation state (Mn^{4+}) to maintain charge neutrality and enhance the conductivity

iv. $SrZr_{0.85}Cu_{0.15}O_{3-\delta}$ samples must be checked for stability and fatigue at prolonged high temperatures and high oxygen ambient conditions

Appendix

Cations	Coordination No.	Ionic radii* (Å)	Electro-negativity	Field strength ($Å^{-1}$)
Sr^{2+}	8	1.26	0.95	0.75
Zr^{4+}	6	0.72	1.33	1.90
Mn^{2+}	6	0.67	1.55	0.97
Mn^{3+}	6	0.58	1.55	1.53
Mn^{4+}	6	0.53	1.55	2.09
Cu^{1+}	6	0.77	1.90	0.46
Cu^{2+}	6	0.73	1.90	0.93
Cu^{3+}	6	0.54	1.90	1.56
Ni^{2+}	6	0.69	1.91	0.96
Ni^{3+}	6	0.56	1.91	1.54
Ni^{4+}	6	0.48	1.91	2.15

Compound	Theoretical density ($g\ cm^{-3}$)	Molar mass ($g\ mol^{-1}$)	Melting point (°C)
SrO	4.70	103.62	2531
ZrO_2	5.68	123.21	2715
MnO_2	5.03	86.93	535
CuO	6.31	79.54	1326
NiO	6.67	74.69	1955

*R.D. Shannon, Acta Cryst. A32 (1976) 751-767.